Quantum dislocations in solid Helium-4

by

Darya Aleinikava

A dissertation submitted to the Graduate Faculty in Physics in partial fulfillment of the requirements for the degree of Doctor of Philosophy

The City University of New York

2012

This manuscript has been read and accepted for the Graduate Faculty in Physics in satisfaction of the dissertation requirement for the degree of Doctor of Philosophy.

	Anatoly Kuklov
Date	Chair of Examining Committee
	Igor Kuskovsky
Date	Executive Officer
	Aditi Mitra
	Alfred Levine
	Alexander Zaitsev
	David Schmeltzer
	William Schreiber
	Anshel Gorokhovsky
	Supervisory Committee

THE CITY UNIVERSITY OF NEW YORK

Abstract

Quantum dislocations in solid Helium-4

by Darya Aleinikava

Thesis supervisor: Prof. Anatoly Kuklov

In this thesis the following problems on properties of solid ^{4}He are considered: i) the role of long-range interactions in suppression of dislocation roughening at $T = 0$; ii) the combined effect of ^{3}He impurities and Peierls potential on shear modulus softening; iii) the dislocation superclimb and its connection to the phenomenon of "giant isochoric compressibility" ; iv) non-linear dislocation response to the applied stress and stress-induces dislocation roughening as a I-order phase transition in 1D at finite temperature.

First we investigate the effect of long-range interactions on the state of edge dislocation at $T = 0$. Such interactions are induced by elastic forces of the solid. We found that quantum roughening transition of a dislocation at $T = 0$ is completely suppressed by arbitrarily small long-range interactions between kinks. A heuristic argument is presented and the result has been verified by numerical Monte-Carlo simulations using Worm Algorithm in J-current model.

It was shown that the Peierls potential plays a crucial role in explaining the elastic properties of dislocations, namely shear modulus softening phenomenon. The crossover from $T = 0$ to finite temperatures leads to intrinsic softening of the shear

modulus and is *solely* controlled by kink typical energy. It was demonstrated that the mechanism, involving only the binding of ^{3}He impurities to the dislocations, requires an unrealistically high concentrations of defects (or impurities) in order to explain the shear modulus phenomenon and therefore an inclusion of Peierls potential in consideration is required.

Superclimbing dislocations, that is the edge dislocations with the superfluidity along the core, were investigated. The theoretical prediction that superclimb is responsible for the phenomenon of "giant isochoric compressibility" was confirmed by Monte-Carlo simulations. It was demonstrated that the isochoric compressibility is suppressed at low temperatures. The dependence of compressibility on the dislocation length was shown to be strongly dependent on long-range interaction.

Non-linear behavior at high stresses was considered. The dislocation was observed to exhibit two types of behavior depending on the dislocation size: reversible and hysteretic. In the reversible regime responses of superclimbing dislocations exhibit sharp resonant peaks. We attribute this feature to the resonant creation of jog-antijog pairs. The peak in the compressibility results in the dip in the speed of sound which we believe was observed in "UMASS-sandwich" mass-transport experiments. The hysteresis revealed an unusually strong sensitivity to the dislocation size signifying that the stress-induced roughening is a I-order phase transition in 1D at finite T.

Contents

List of Figures

Chapter 1

List of Abbreviations

1D One-dimensional

2D Two-dimensional

3D Three-dimensional

BEC Bose-Einstein Condensate

BKT or KT Berezinskii-Kosterlitz-Thouless (phase transition)

CP Closed-path (configuration)

NCRI Non-classical rotational inertia

NCRIF Non-classical rotational inertia fraction

ODLRO Off-diagonal long-range order

MC Monte-Carlo

SF Superfluid

SG Sine-Gordon

TO Torsional oscillator

UMASS "sandwich" experimental set-up designed in University of Massachusetts by R. Hallock and collegues.

WA Worm algorithm

Chapter 2

Introduction

2.1 Supersolidity: experiments

A supersolid is a peculiar state of matter that simultaneously displays both superfluidity and crystalline order for the same sort of atoms. ^{4}He is thought to be a most likely candidate for the supersolid state due to the significant zero-point motion of atoms in the crystal lattice. Potential evidence for such a supersolid phase in Helium-4 has been first detected as non-classical rotational moment of rotational inertia (NCRI) in torsional oscillator (TO) experiments [1, 2, 3, 4] more than thirty years after the first proposals by Andreev and Lifshitz [5] and Chester [6]. For quite some time, there was no direct evidence indicating that solid ^{4}He really possesses this unique property since it did not respond to pressure differences [7, 8, 9, 10], no persistence currents were observed, and the material did not offer any other superflow features.

Since then a number of theories was suggested in attempt to explain the observed phenomenon. The earliest theory suggested by Andreev et al. [5] to explain supersolidity relied on so-called zero-point vacancies. The vacancies in a solid can move through the crystal by quantum tunneling mechanism. If the creation energy for

vacancy is zero, these vacancies can exist even at zero temperature. Since these vacancies are bosons, they can Bose condense below some critical temperature and form a superfluid. Therefore, the flow of vacancies leads to the flow of atoms in the solid forming a supersolid. The idea of vacancies being the reason for a supersolid state was much talked of and sometimes directly criticized (by Penrose and Onsager [11]), but not resolved completely till the very recent time.

Both measurements and calculations [12] indicate that vacancies in helium have an activation energy of at least 13 K, with no evidence of vacancies at zero temperature. Recently, it has been shown by Monte-Carlo simulations that supersolidity should not be expected in perfect, commensurate crystals [12]. Several features of TO experiments [1, 2, 3, 4] indicate strongly inhomogeneous nature of superfluidity because of , mostly, the overwhelming effect of a small concentration of ^{3}He impurities. This placed extended defects such as dislocations and grain boundaries in the center of attention as possible candidates for supersolid response [13, 14, 15, 16, 17, 18, 19, 20].

It was suggested in Ref. [21], that quenched dislocations (with superfluid dislocation cores) forming a 3d network can facilitate the supersolid/normal solid transition. In this picture, as temperature T decreases below the condensation temperature $T_{cond} \sim 1$K (which is comparable to the λ-temperature in liquid ^{4}He) , each dislocation line in a tangled network of them nucleates a cylindrical supersolid tube tangent to it. The places where dislocations cross, making supersolid tubes overlap, are the sites of a random lattice. A typical length of these bonds L determines the mean dislocation spacing. It grows with annealing; $L \to \infty$ for a clean crystal. This random lattice does not develop macroscopic supersolidity (or undergo any phase transition) at T_{cond} , because of the 1D nature of fluctuations in each tube suppressing the phase coherence exponentially with L at finite T. However, as temperature is lowered further, such coherence inevitably develops at certain mesoscopic temperature $T_c \sim T_{cond}/L$ (where

L is measured in units of the inter-atomic spacing), leading to the supersolid/normal transition.

The superfluidity of the cores of screw dislocations was found by Boninsegni *et. al.* in [13], who performed Monte-Carlo simulations of the screw dislocation along the hexagonal axis of an *hcp* crystal. The core exhibited superfluid response. At the same time, the same type of screw dislocation in solid H_2 turned out to be insulating. These simulations yielded thus the first realistic example of a supersolid in free space. Authors also noted that instead of being focused on one isolated screw dislocation one can notice that small twist-angle grain boundary can be represented as an array of screw dislocations and, therefore, must possess superfluidity feature with an additional ability of tunneling coupling between the cores. Therefore such boundaries might be the most realistic objects for studies of superfluidity of screw dislocations.

Balatsky et. Al. in [16] considered thermodynamic properties of near 200 mK (temperature range near supposed solid/supersolid transition), and found that the experimental entropy is substantially less than the calculated entropy derived from $S_\lambda = 4.6JK^{-1}mol^{-1}$ at $T_\lambda = 1.8K$ for ^{4}He at high pressure [22] with 1% superfluid fraction observed in Kim and Chan experiments [1, 2]. Similar calculations done with more recently obtained data [23] still yield values too high comparing to the measured entropy of 20 $\mu JK^{-1}mol^{-1}$ [24].Authors suggested that the low temperature linear term in the specific heat is the result of the dislocation induced glassy state in solid ^{4}He. It was suggested that small scale dislocation loops form those tunneling systems. They claimed that NCRI anomaly is consistent with their scenario and predicted that the linear term should increase with ^{3}He concentration. The calorimetry measurements [23] did not confirm the presence of the linear term in the specific heat but it is possible that one needs strongly disordered samples to see it.

2.1.1 Torsional oscillator experiments

The first experiments which provoked so many discussion, debates and arguments were done by Kim and Chan in 2004 [1, 2] and can be considered as a non-direct evidence of the supersolidity phenomenon. Authors used torsional oscillator (TO) technique. In their set-up the torsion bob containing either Vycor glass disk or an annular channel is attached to the torsion rod and can be filled by ^{4}He through the filling line inside the rod. Lock-in amplifier supplies a driving voltage and regulates the oscillation amplitude which keeps the oscillator in resonance. The resonant oscillations period in such a system is given simply by $\tau = 2\pi\sqrt{I/G}$, where I is the torsion bob moment of inertia, and G is a spring constant of a torsion rod. The pore space of around 30% in Vycor porous disk (or an annular channel in a second setup) was filled with liquid ^{4}He and solidified by pressures ranging from 26 bar to 66 bar.

If one would measure a liquid superfluid ^{4}He during oscillations, a part of the mass would decouple thus reducing the moment of inertia I which will result in lower period τ. Such phenomenon is referred to as non-classical rotational inertia (NCRI) [25]. The relative change in the inertial momentum is called the NCRI fraction (NCRIF) and it can be identified as

$$NCRIF = \frac{\rho_s(T)}{\rho} = \frac{I(T_0) - I(T)}{I(T_0) - I_{empty}}, \tag{2.1}$$

where I_{empty} is the moment of inertial of an empty cell, $I(T)$ is the moment of inertia of a cell, filled with ^{4}He, and T_0 is defined as a critical temperature below which superfluidity appears (for liquid He). If the change in resonant period is small the last equation can be rewritten as

$$NCRIF = \frac{\tau(T_0) - \tau(T)}{\tau(T_0) - \tau_{empty}}. \tag{2.2}$$

It was found [1, 2] that solid ^{4}He below $T_0 \approx 230mK$ exhibits the decrease in τ implying that a fraction of the mass about 1% decouples from the sample. The latter was interpreted as the first evidence of supersolidity. The NCRI fraction has also been found to depend strongly on the oscillation speed. The period shift was to be up to 20 ns for the rim velocities $V_{rim} = 31\mu$m/s (Vycor glass) and up to 42 ns for $V_{rim} = 4\mu$m/s (annular channel). Exceeding these values of V_{rim} lead to a significant suppression of NCRIF. Thus it was concluded that the critical speed of superfluid fraction in supersolid ^{4}He should be of the order of 10 μm/s.

The oscillation amplitude vs T demonstrates a broad minimum, and since the ac voltage was constant for all measurements, such feature indicates a presence of the dissipation maximum at some temperature. The control experiment on solid ^{3}He which is a fermion revealed no detectable NCRIF. Finally the effect of ^{3}He impurities was investigated in bulk solid ^{4}He samples and it was found that T_0 below which superfluidity appears is growing monotonically as ^{3}He concentration is increasing with a broad NCRIF maximum around 0.2 ppm [18]. The frequency shift was also found surprisingly sensitive to amount of ^{3}He atoms changing considerably even for tiny impurity concentration.

Heat capacity measurements [26] have also revealed a peculiar feature: a peak below 200 mK in a solid ^{4}He sample. The peak was found to be independent of ^{3}He concentration, but responsive to a sample quality, similar to NCRI. In a scenario [27] proposed to explain this phenomenon the peak was attributed to the presence of superclimbing phonons which will add to the specific heat a term $\sim \sqrt{T}$ – a considerable contribution to the standard T^3 dependence at low T.

To summarize, TO measurements with solid ^{4}He revealed several puzzling anomalies which are yet to be explained. First, it showed an unexpected sensitivity to ^{3}He impurity concentration. Second, the critical velocity above which NCRI disappears is extremely small: of the order of 10μm/s, while a speed of sound in the material is in the vicinity of 100 m/s. Third, specific heat exhibited a deviation from standard T^3 behavior below $T < 200mK$ resulting in a peak formation.

2.1.2 Shear modulus anomaly: its relation to dislocations and supersolidity

Very interesting results were obtained in studies of mechanical properties of solid ^{4}He [20, 28]. Beamish and colleagues measured a shear modulus of ^{4}He at low frequencies and strains, and the effect of annealing and large stresses. Their experimental technique involved embedding piezoelectric transducers in the helium which allowed the direct measurements of shear modulus G for a strains down to 2.2×10^{-9} (stress 0.03 Pa). Samples were grown under constant average density condition, this method being referred to as a blocked capillary technique. It is known to produce polycrystalline samples with a lot of disorder. The impurities concentration amount ranged between regular commercial purity of 0.3 p.p.m and almost isotopically pure count of 1 p.p.b. The main observed feature was the large (around 10%) increase of shear modulus below 200 mK with the striking resemblance to the NCRIF temperature behavior. Both $G(T)$ and NCRIF shared the dependence on concentration of ^{3}He impurities and demonstrated similar annealing effect [20]. Thus, it is reasonable to assume that both phenomenon have the same physical origin.

The shear modulus dependence on temperature $G(T)$ is presented on Fig. 2.1[20]. The data were obtained for different frequencies ranging from 20 Hz to 2000 Hz and

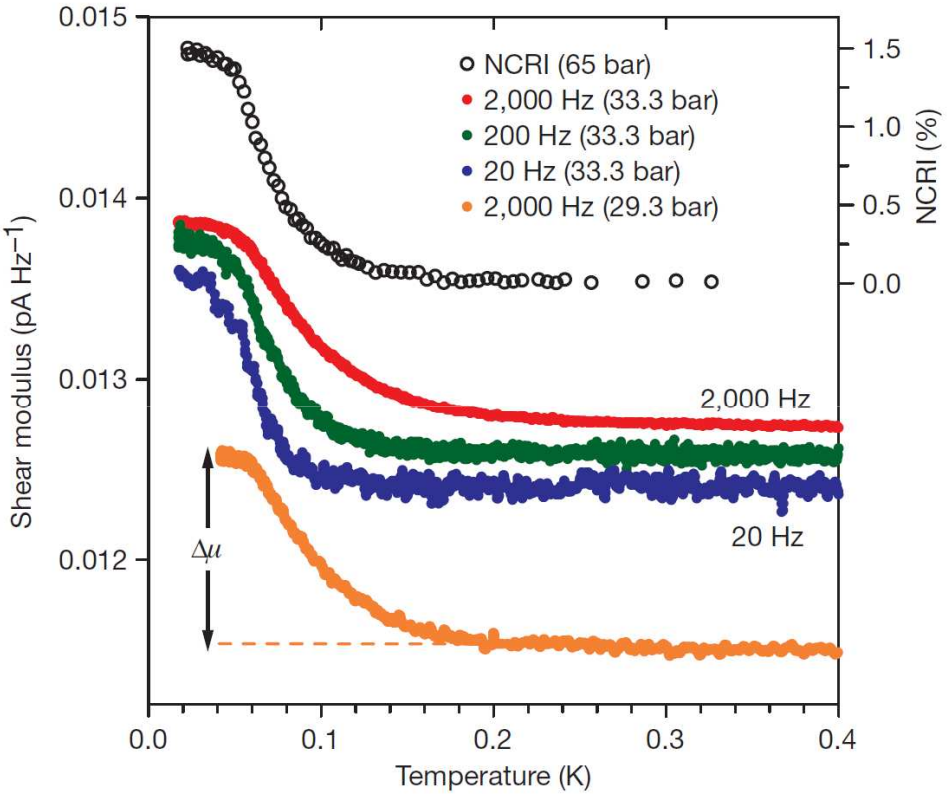

Figure 2.1: Shear modulus and NCRI fraction of solid ^{4}He as a function of temperature [20].

were plotted together with NCRI for easy comparison. At smaller frequencies the onset of the shear modulus softening shifts to smaller temperatures, with the similarity to NCRIF remaining the same (unfortunately, repeating the TO measurements at various frequencies is not possible for now).

Another interesting feature is the shear modulus sensitivity to the ^{3}He concentration: it was found [20] that G softening onset moves to lower T for small amount of ^{3}He in a way, similar to decoupling fraction. The annealing was found to lessen the shear modulus change at higher temperatures while the lower temperature region remained essentially the same.

It was suggested [20, 28] that the observed G anomalies could be explained in

terms of dislocations moving between the pinning points as a result of the shear stress. 3D dislocation network pin their ends effectively but they are free to shift between these pinning points. This displacement reduced the shear modulus of the sample observed in the experiments. In this case the modulus change $\Delta G/G \approx \Lambda L^2$ [28, 29] ,where Λ is the dislocation density and L is the typical dislocation length between the pinning points. It is clear that the longest dislocations produce the most significant displacement thus contributing the most to the G softening. However, the longer size required smaller density and therefore modulus change is practically *independent* of the dislocation density. The authors [20, 28] argued that this mechanism can explain G softening of the order of 30%. It was further proposed that ^{3}He impurities play a major role in the temperature dependence of $G(T)$ by providing an additional pinning of dislocations though not so effectively as the network cross-linking. The impurity concentration of on the dislocations is $\approx \exp(E_a/T)$ (in atomic units), where E_a is a binding energy (or the order of $E_a \sim 0.3 - 0.7$ K [28]) of ^{3}He atom to a dislocation. If there is on average one atom of ^{3}He on each dislocation the pinning becomes significant. Eventually, as ^{3}He concentration on dislocations increases further, dislocation loose their mobility and the shear modulus recovers its value for a defect-free crystal. The temperature around which such pinning becomes significant can be estimated from the following simple considerations. Let's imagine a cube made of dislocation segments of length $L >> 1$ (in the units of the inter-atomic distance) which contains $L^3 x_3 >> 1$ atoms of ^{3}He at high T, where $x_3 << 1$ denotes a ^{3}He bulk fraction. Thus, the temperature $T_{^3\mathrm{He}}$ below which ^{3}He atoms start effectively pinning dislocations [28] (determined from the equilibrium condition that there is at least one impurity per edge) is

$$T_{^3\mathrm{He}} \approx -\frac{E_a}{\ln(x_3 L)}, \tag{2.3}$$

where it is assumed that $x_3 L << 1$. We will show later, however, that the impurity-binding scenario, while agreeing qualitatively with the observed behavior, results in a much sharper changes in $G(T)$. To smoothen the transition one needs to include the Peierls potential into consideration (see Section 6).

The results of Day and Beamish may imply that the famous Kim and Chan TO experiment [1] showed the decrease in period $\tau = 2\pi\sqrt{\frac{I}{G}}$ not due to the decrease in I, but rather due to the increase of G which contributes to the effective torsional spring constant. However, such scenario provides an explanation for only about 1% of the NCRI fraction.

The possible explanation of these results was suggested by Biroli and Bauchaud [30] who connected this phenomenon to the proliferation of dislocation strings. The authors suggested that below a certain temperature T_c , the free energy of kink-antikink pairs of dislocations becomes negative, leading to an increasing wandering of dislocations that would form an entangled network similar to a polymer melt. In their opinion, this proliferation of kink-antikink pairs should lead both to an increased stiffness of the solid, and to kink-induced superfluid motion. Though the question whether the dislocations network undergoes a true phase transition is at this stage an unresolved problem, they expected a (small) specific heat anomaly and a change the elastic properties of the system around T_c . This could explain the shear modulus anomaly, witnessed by Day and Beamish, and other elastic anomalies, perhaps even a partial decoupling of the solid in a oscillating pendulum experiment. This effect should, they think, disappear as soon as supersolidity really establishes. Going a little bit ahead it should be mentioned that the results presented in the work [30] suggest that at low temperatures dislocations in ^{4}He exist in roughened state. As it will be discussed below, there are strong arguments against such conclusion.

Another set of measurements of elastic properties of solid ^{4}He crystals was per-

formed by Balibar and colleagues [31, 32] and the stiffening at low T was observed even in "impurity-free" crystals (i.e. crystals kept in equilibrium with liquid helium). This fact confirms our suggestion that impurities alone can not explain shear-modulus anomaly (Section 6). Another amazing feature was that for a freshly grown crystals the increase of the temperature from $T \approx 20mK$ and up actually *stiffens* the crystal, the anomaly *opposite* to what was measured before. Such behavior can be explained by the elastic properties of slanted dislocations [33]. During the crystal growth the dislocation ends can become strongly pinned and end up in different Peierls potential valleys. The latter signifies that even at very low T the dislocation string has a finite number of kinks which "form a superfluid" thus increasing the dislocation mobility. This effect can be diminished by kinks binding to random deformation potentials due to structural defects.

2.1.3 UMASS "sandwich" experiments

It is natural to expect that a supersolid should allow the superfluid mass flux through it. Thus, an evidence of such a flux would be a direct proof of the supersolidity. However the attempts to obtain the matter flow by directly pressing on the solid ^{4}He in a confined geometries have not produced any results [7, 8, 9, 10]. R. Hallock and colleagues developed a new approach and constructed a so-called "sandwich" design [34, 35, 36, 37, 38, 39]. The idea was to apply a chemical potential gradient across the sample rather than to apply pressure directly. The conceptual structure of their "sandwich" is presented on Fig. 2.2.

The experimental setup consisted of a main copper cell and two Vycor rods with liquid ^{4}He reservoirs attached to it. The main chamber then contains the solid *hcp* ^{4}He and the rods can serve to feed liquid helium intro the sample. The cell has two capac-

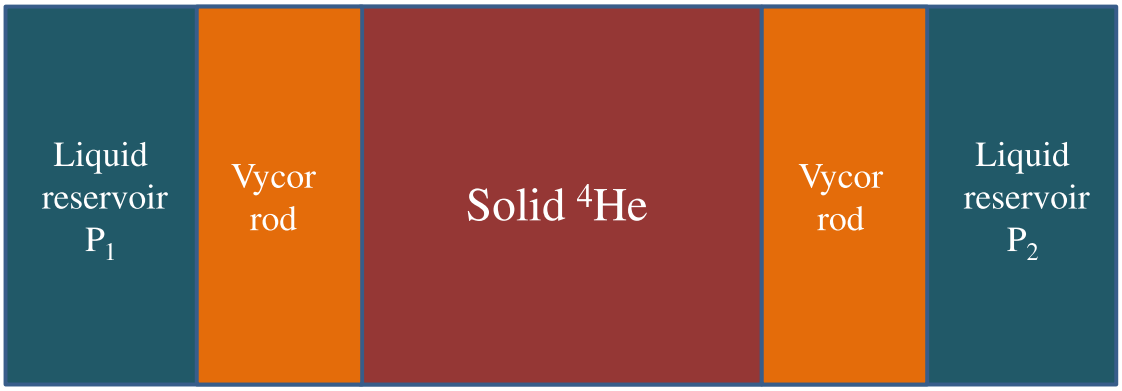

Figure 2.2: A conceptual representation of a "sandwich" experimental geometry where three compartments are separated by porous Vycor rods filled with liquid ^{4}He. The temperature gradient is applied across them to revent ^{4}He from freezing.

itive pressure gauges attached on either side for *in situ* pressure measurements. Each reservoir can be heated to prevent ^{4}He from freezing and their temperatures/pressures T_1, T_2, P_1 and P_2 can be measured. The purpose of the experiment was to transfer atoms from one liquid reservoir to another through the solid by applying either pressure or temperature difference between the reservoirs. And indeed it was possible to observe correlated changes in reservoir pressures signifying the flow through the solid sample which was happening at a certain constant speed. The latter does not depends on the applied chemical potential gradient which agrees with a critical flow happening at a certain critical velocity as it would be for a cell with superfluid liquid ^{4}He. The flow was observed at temperatures below 600 mK. In a liquid helium it is possible to create a pressure difference $P_1 - P_2$ as a reaction to the temperature difference $T_1 - T_2$, a phenomenon known as a fountain (or thermomechanical) effect. It was seen [37, 38, 39] that $T_1 - T_2$ induces the flow of atoms resulting in the pressure difference $P_1 - P_2$ and their relation agrees with the expected fountain effect. It was suggested the the observed flux through the solid is due to the conducting paths which were theoretically predicted to exist in the sample, namely, dislocations

with a superfluidity along their cores. With this assumption it looks reasonable to suppose that mechanical pressure on the sample does not allow access to the cores while injection of atoms from superfluid does.

In the very recent study [39] another quite interesting effect was observed: the flux through the cell suddenly drops at approximately $T \approx 80mK$ and then recovers as temperature decreases further. This effect is rather robust and can be repeated in warming/cooling scans. We explain this phenomenon by a non-linear properties of superclimbing dislocations which will be discussed in length in Section 7.

To sum up, the topological defects in crystals which were considered before as just irregularities in an ideal crystal lattice turn out to be far more interesting and exciting then expected. As we have seen, it is believed now that dislocations are responsible for a lot of peculiar properties of quantum crystals such as ^{4}He, so the study of their properties is an essential goal for condensed matter physics.

2.2 Berezinskii-Kosterlitz-Thouless phase transition

In this section we will consider the main idea of Berezinskii-Kosterlitz-Thouless (BKT) phase transition the actual realization of which in quantum dislocations will be described later (see Appendix A and Section 5.2).

At high temperatures most physical systems are homogeneous isotropic liquids which do not possess any positional or orientational order. When temperature T is decreased they loose their homogeneity and acquire some sort of order. The transformation from disordered to ordered state is called a phase transition. The distinguished feature of first order phase transition is singularity or discontinuity in the first derivative of a thermodynamic potential (solid/liquid/gas transitions). The second order phase transitions are continuous transitions (e.g., ferromagnetic transition). ^{4}He remains liquid even $T = 0$. Despite that, it also undergoes a II order phase transition, which is characterized by so called off-diagonal long-range order (ODLRO) leading to superfluidity [11].

The description of an ordered condensed system requires introduction of a collective variable – an order parameter $\langle\phi\rangle$ [40] . Generally, it is an average value of the operator ϕ which is a function of dynamical variables of the system. Obviously, since it is a characteristic of the order, its value equals zero in the disordered phase. If order is characterized by a vector defined on some plane, one can introduce continuous variable θ which gives the direction of such vector. Then, if the planar rotational symmetry is broken, spatial distribution of such "angle" θ, instead of being uniform, may exhibit topological defects. In XY-model they are called vortices, in crystals — dislocations.

Let us consider the XY-model and see what role vortices play in two dimensions. The Hamiltonian of this model is given by

$$H = -J \sum_{\langle i,j \rangle} \mathbf{S}_i \cdot \mathbf{S}_j = -J \sum_{\langle i,j \rangle} \cos(\theta_i - \theta_j), \tag{2.4}$$

where summation runs over the nearest neighbor sites in the lattice and θ_i is the orientation of a spin in site i. One can expand cos-function in Taylor series obtaining $H = E_0 + J \sum\limits_{\langle i,j \rangle} \frac{(\theta_i - \theta_j)^2}{2}$ or, in continuous form,

$$H = E_0 + \frac{J}{2} \int d^2x \left(\nabla\theta\right)^2, \tag{2.5}$$

where E_0 is the energy of the ground state.

The angle gains $2\pi n$ traveling around any closed contour enclosing the core of the vortex, n being a winding number of a vortex, or

$$\oint \nabla\theta\left(\mathbf{r}\right) \cdot d\mathbf{l} = 2\pi n. \tag{2.6}$$

This equation and the condition of minimum of the energy allows us to choose the solution in the form $\theta = n\phi$, where $\phi = \tan(y/x)$.

Then

$$\nabla_x\theta = \frac{y}{r^2} n, \quad \nabla_y\theta = -\frac{x}{r^2} n, \quad \left(\nabla\theta\right)^2 = \frac{n^2}{r^2}. \tag{2.7}$$

Therefore, the energy of the vortex is

$$E_v = \frac{J}{2} \int d^2x \left(\nabla\theta\right)^2 = \frac{J}{2} n^2 2\pi \int_a^R \frac{dr}{r} = Jn^2\pi \ln\frac{R}{a}, \tag{2.8}$$

where to avoid singularities we introduced R (a linear dimension of a sample) and a (distance between neighbor sites in the lattice). Evidently, a vortex is a rather energetically costly excitation. However, such defects are very unlikely to disappear

if they were created during the phase transition. There are no continuous deformations of the order parameter that will lead to their destruction. The energy of a discontinuous deformation is of the order JR. The energy barrier for a system to destroy a vortex through returning to the disordered state and back is of order JR^2, which is even more. Similarly, it is hard for a system to create a single vortex. But the pair of vortices with opposite winding numbers is the configuration that can be brought to the uniform state by continuous transformation of spins. The creation and destruction of a pair does not change total vorticity of a system, therefore, such configuration is topologically equivalent to the uniform state.

At low temperatures the order parameter correlation functions has quasi-long-range order, that is, they decay as power laws in 2D. At high T, they decay exponentially. It means that at certain temperature there is a phase transition from one state to another. In 1972 Berezinskii [41] and independently in 1973 Kosterlitz and Thouless [42] showed that at such transition vortex pairs proliferate and make a 2D system fully disordered. Let us consider free energy of the system $F = E - TS$, and see what are the condition for its minimum. The entropy per vortex is $S = k_B \ln \Gamma$, where Γ is the number of microstates that allow the presence of one vortex. Obviously, Γ equals $\frac{R^2}{a^2}$ — the number of lattice sites where the vortex can be centered. Therefore,

$$F = Jn^2\pi \ln \frac{R}{a} - Tk_B \ln \frac{R^2}{a^2} = \left(Jn^2\pi - 2Tk_B\right) \ln \frac{R}{a}. \tag{2.9}$$

So we see, that the spontaneous formation of vortices becomes advantageous at $T > T_{BKT}$, where $T_{BKT} = \frac{J\pi}{2k_B}$. This simple heuristic argument points to the fact that the logarithmic dependence on system size of the energy of the vortex combines with the logarithmic dependence of the entropy to produce the subtleties of the vortex

unbinding transition. Assume a different dependence of the energy on systems size and one will either have thermal activation of vortices at all temperatures (in the case E_v is slower than $\ln R$) or vortices will be always bound into pairs at any temperature (in the case $E_v \propto (R/a)^b, b > 0$). It is the logarithmic size dependence of the 2D vortex energy that allows the outcome of the competition between the entropy and the energy to change qualitatively at a certain finite temperature T_{BKT}.

There exists a useful analogy between vortices in XY model and electric charges in two-dimensional plasma. The interaction potential between vortices with windings n_1 and n_2 in 2D system is given by

$$U_{12} = -2\pi J n_1 n_2 \ln\left(\frac{|\mathbf{r}_1 - \mathbf{r}_2|}{a}\right). \tag{2.10}$$

where n_1 and n_2 are centered at $\mathbf{r}_1$ and $\mathbf{r}_2$ respectively. The logarithmic dependence on the distance between the vortices makes it similar to the interaction between charges in 2D Coulomb gas which is also $\sim \ln(\mathbf{r}_1 - \mathbf{r}_2)$. In this comparison the winding number n plays the role of the electric charge.

A peculiar feature of the electrostatic interactions in two dimensions is that the mechanical work needed to separate a pair of charges of opposite sign is infinite. Consequently, the low temperature phase of a 2D plasma is an insulator: at $T < T_{BKT}$ charges are bound into pairs with infinite ionization energy. This analogy allows to understand the nature of the phase transition in the XY model at $T = T_{BKT}$. The low temperature state with no vortices can be viewed as the state in which vortices of opposite vorticity are bound into pairs. At $T > T_{BKT}$ these pairs unbind, creating a disordered state with random phase $\phi(\mathbf{r})$ that corresponds to random orientation of spin-vectors.

Chapter 3

Elastic properties of dislocations

3.1 General properties

Dislocation is an 1D topological defect in a 3D crystal which partially breaks translational symmetry of the lattice thus rendering it imperfect. Originally the basic properties and classification of dislocations were developed while plastic deformations of solids were tried to be described [43]. It was noticed that under certain stresses the crystal deforms by creating the *translational* slip during which one part of the crystal slides with respect to the other. It was observed that the material in the slip planes remains crystalline during slip which starts on irregularities of the lattice. The other interesting fact was that slip spreads consecutively, not simultaneously, over a slip plane. The line around the boundary between the slipped region and the rest of the crystal was called a *slip dislocation line*. It is presumed from the definition that the dislocation lines must either form loops or end on the crystalline surfaces [43, 44, 45].

The earliest experimental data revealed a surprisingly minute amount of stresses required to deform the crystal plastically. The proof why this fact can not be described by slips in perfect crystals is the following [46]. Let's consider two rows of a

homogeneously strained crystal. We will identify σ as a shear stress acting on them (see picture), with shear displacement x of the upper row over the lower one, and a and b being the spacing between the rows and atoms accordingly (see Fig.3.1).

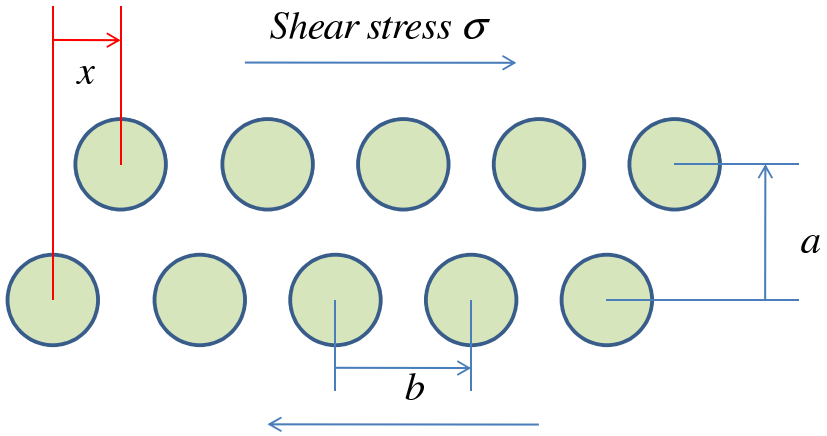

Figure 3.1: Shear stress on two rows of atoms.

The interaction with the atoms from the neighboring row pushes the atom to its nearest lattice site thus rendering the shearing force periodic in x with period b. Assuming that the force is sinusoidal $\sigma = k \sin(2\pi x/b)$ we have at small x $\sigma = k2\pi x/b$. Hooke's law gives $\sigma = Gx/a$, where G is a shear modulus. This leads to

$$\sigma = \frac{b}{a}\frac{G}{2\pi}\sin\left(\frac{2\pi x}{b}\right) \tag{3.1}$$

The critical shear stress required to produce a slip in a lattice is therefore

$$\sigma_{crit} = \frac{b}{a}\frac{G}{2\pi} \tag{3.2}$$

For a close to b the value of $\sigma_{crit} \approx \frac{G}{2\pi}$ is several orders of magnitude greater than the experimental data. Any refinements to the above crude calculation, such as considering realistic laws for the forces between atoms, including all possible configurations of mechanical stability while slipping, accounting for thermal vibrations, led

to the reduced value of $G/30$ or so. This value was still too big, therefore proving that the defects in the crystal are essential in explaining the plastic properties of crystals.

There are two basic types of dislocations: edge and screw. The actual dislocations in crystal can be of one type or represent a certain combination. To visualize a dislocation geometry one should imagine first starting to cut a crystal but stopping half-way through so that that upper part is cut in half and the lower part is untouched. Then the edge dislocation can be thought of as the end of an *extra plane of atoms* inserted in the cutting plane (Fig.3.2). A screw dislocation is obtained if one *displaces* two upper halves with respect to each other along the cutting line (Fig.3.3).

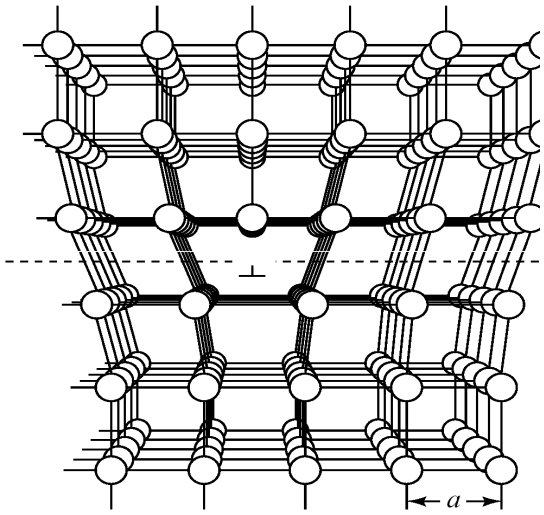

Figure 3.2: An example of an edge dislocation. Here its core is perpendicular to the picture. Extra plane of atoms is inserted from above.

The most useful dislocation description is given in terms of the Burgers circuit. A Burgers circuit is any atom-to-atom path chosen in crystal that forms a closed loop. An example of such a path enclosing an edge dislocation is illustrated on Fig.3.4a, it is denoted by ABCDE. If the same atom-to-atom sequence is considered in a defect-free crystal as in Fig.3.4b and the circuit remains open it means that the original circuit in Fig.3.4a contains at least one dislocation. The vector required to complete the

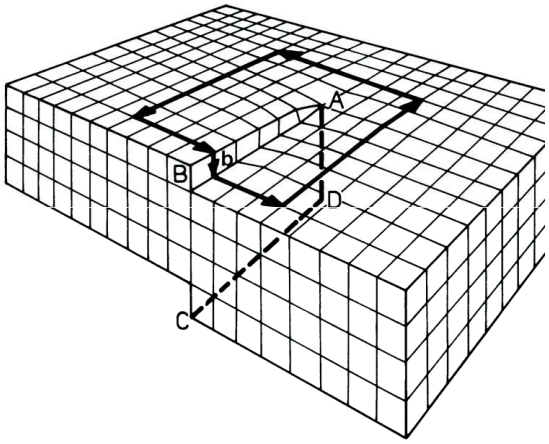

Figure 3.3: An example of a screw dislocation. AD is the cutting line being simultaneously a dislocation core in this case. Two halves are displaced along AD. The Burgers vector required to complete the Burgers circuit is *parallel* to AD.

circuit is called the *Burgers vector* b. The Burgers vectors in a simple cubic lattice are the shortest lattice translation vectors which join two points in the lattice. A dislocation whose Burgers vector is a lattice translation vector is known as a perfect or unit dislocation. The direction of b also provides a way to distinguish between edge and screw dislocation since for an edge dislocation b is *normal* (Fig.3.4a) to the dislocation line, and for screw it is *parallel* (Fig.3.3) to it. In general dislocation core lies at an arbitrary angle to its Burgers vector b if it has a mixed edge and screw character. It should be noted that Burgers circuits taken around other types of defects, such as vacancies or interstitials do not result in closure failures.

Dislocations lines never end inside the crystal, they always either form a closed loop, or branch into other dislocations, or terminate at the crystal surface. The dislocation density ρ is defined as a total length of dislocation lines per unit volume of crystal and is measured in cm^{-2} or m^{-2}. Sometimes it is also calculated as a number of dislocations intersecting a unit area. All crystals contain dislocations and in well-annealed ones they are arranged in a 3D forest where the average distance between

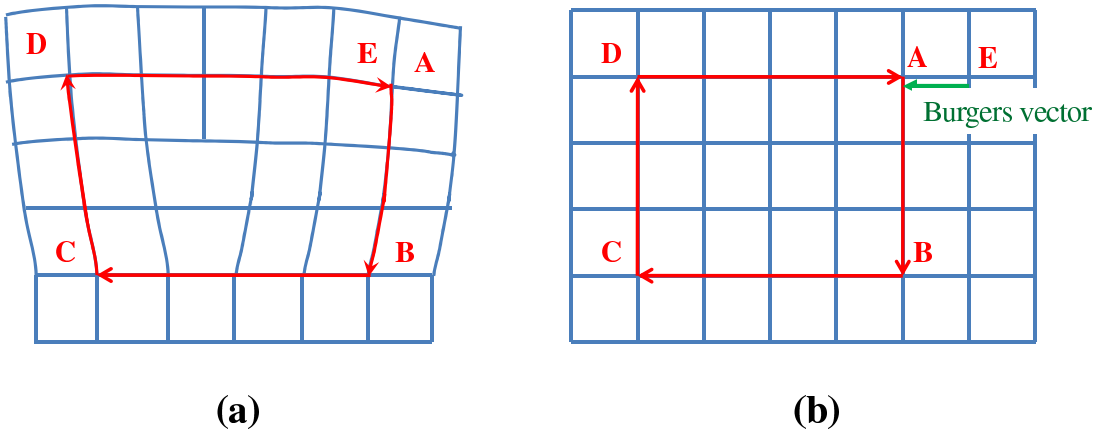

Figure 3.4: a) Burgers circuit ABCDE around a single edge dislocation. b) The same atom-to-atom path taken in a dislocation-free crystal leads to an open circuit. It requires a Burgers vector to complete it.

dislocations in a network of density ρ is of the order $1/\sqrt{\rho}$. Typical dislocation density in metals is between $10^{10}m^{-2}$ and $10^{12}m^{-2}$.

A dislocation, like, for example, in Fig.3.4a, can perform two types of motion: glide and climb. Glide is a conservative type, it corresponds to the dislocation core moving in a horizontal direction on Fig.3.4a, or one can say that it is a motion in a *slip plane* discussed above. Climb, on the other hand, is a non-conservative motion type, it consists of dislocation line moving along the vertical on Fig.3.4a., thus requiring the building (or removing) of the edge of the extra plane of atoms. The elementary displacements of short dislocation sections are called kinks and jogs for glide and climb respectively. Gliding dislocations will be discussed at length in Chapter 5. Usually at low temperatures where diffusion is difficult and in the absence of point defects the dislocation motion is restricted almost entirely to glide since it does not require a mass influx. However at high temperatures due to the flow of vacancies towards, away or along the cores (a process of so-called "pipe diffusion" [44, 47]) climb becomes possible. It was suggested that at very low temperatures in ^{4}He the dislocation cores become superfluid and the atoms can be delivered along the cores

by a superflow instead of the "pipe diffusion". This results in a process which is called "superclimb" [48]. It should be noted that pure screw dislocations have no extra half-plane and in principle cannot climb. However, a small edge component or a jog on a screw dislocation will provide a site for the start of climb. The properties of the superclimbing dislocations will be discussed in Section 7.

Inside a crystal the dislocations can exist separately, create a 3D network by intersecting with each other or they can form loops. If a dislocation form a loop in the plane and its Burgers vector b belong to that plane then the plane is a slip plane and the loop can shrink or expand by glide. When however b does not belong to that plane then the slip surface is cylindrical and the dislocation loop is called a *prismatic loop*. In this case loops can glide conservatively along this cylindrical surface, but their expanding or shrinking will require climbing. The mechanism of loop creation are numerous including Bardeen-Herring, Frank-Read mechanisms and so on [44, 45]. Under the influence of large stresses or injection of extra matter into the solid like in [34, 35, 36, 37, 38, 39] the amount of produced loops can strongly surpass the number of "straight" dislocations. Considering the fact that they also can move quite unimpeded inside the crystal the prismatic loops can significantly affect the material properties. It was, for example, suggested, that the superfluidity along the core of prismatic loops can be an explanation for a specific heat anomaly and extremely small critical speed in TO experiments [27].

3.2 Classical description: elastic string

3.2.1 Granato-Lüke approach

In a traditional description gliding dislocations are considered as elastic strings able to move freely inside the crystal unless their ends are pinned by, say, the intersection points with neighboring dislocations or, perhaps, impurities (such as ^{3}He). Such representation is the core of Granato-Lüke theory of internal friction in metals [29]. Let's consider the edge dislocation of length L_x gliding in a (x, y) plane with a Burger's vector b parallel to y-axis. The glide of such dislocation is characterized by its displacement $y(x,t)$. The action of such a system should include the kinetic energy of string motion $H_k = \int dx \frac{n_1}{2} (\partial y/\partial t)^2$, with n_1 being a linear mass density. The displacement $y(x,t)$ induces sting deformation which results in string tension thus contributing an elastic energy term $H_{el} = \int dx \frac{n_1 V_d^2}{2} (\partial y/\partial x)^2$. Here V_d stands for the speed of sound along the string. These two terms proved to be very useful in explaining many properties of metals at high temperatures [29]. At low temperatures, however, one should consider the effect of the lattice on the dislocation, namely, the Peierls potential should be included $H_P = u_P \cos(2\pi y/b)$. The lattice contribution is taken in the simple cos-form, as it was done, for example, in [49], with u_P denoting the strength of the Peierls potential. Therefore the full action in imaginary time is

$$S_{SG} = \int_0^\beta dt \int_0^{L_x} dx \left[\frac{n_1}{2} (\partial y/\partial t)^2 + \frac{n_1 V_d^2}{2} (\partial y/\partial x)^2 - u_P \cos(2\pi y/b) - fy \right]. \quad (3.3)$$

Here f stands for the linear density of exteranl force. At low temperatures the long-range interaction between kinks [45, 49] is also relevant and will be introduced in our simulations.

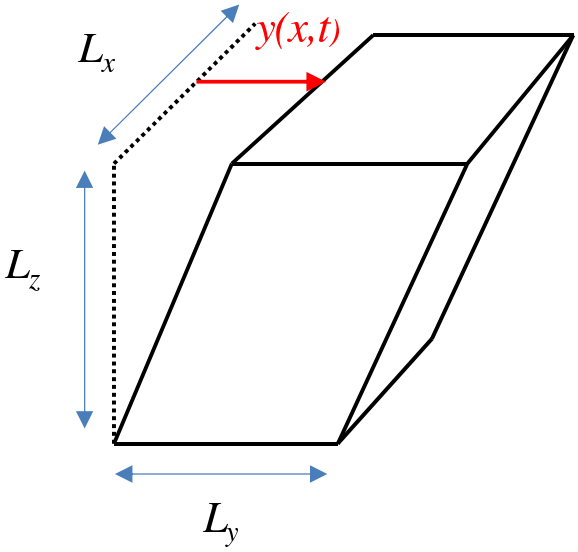

Figure 3.5: A single cube of 3D network formed by the dislocation lines (Frank's dislocation forest). Typical segment lengths are denoted by L_x, L_y and L_z. Applied strain results in the displacement $y(x,t)$.

The dislocation lines inside the crystal cross-link each other and form an almost periodic 3D network (Frank's dislocation forest [50]) and can be considered as having a typical segment lengths L_x, L_y, L_z along the corresponding orthogonal axes as in 3.5.

In this case the uniform stress σ applied to the lattice can be related to uniform 3D strain tensor. The displacement $y(x,t)$ under a small force $f = \sigma_{zy} b$ leads to a strain of the block $u_{zy} \approx by/(L_y L_z)$. Here σ_{zy} signifies a stress tensor [51]. Therefore $y \propto \sigma_{zy}$ and

$$u_{zy} = \frac{bN_d}{L_x} \int dx < y(x,t) >, \tag{3.4}$$

where $N_d \equiv \frac{1}{L_y L_z}$ is interpreted as a dislocation density in the chosen system of coordinates. In the following description it will be useful to employ the dimensionless dislocation density $n_d \equiv b^2 N_d$ in units of Burger's vector b. Since in solid ^{4}He $b \approx 3.5\mathring{A}$

to switch from dislocation density N_d measured in cm^{-2} one has to multiply it by $\approx 10^{-15}$, so that $n_d = 10^{-8}$ will correspond to $N_d = 10^7 cm^{-2}$.

Though segments lengths L_x, L_y, L_z can, in general, be different, we will assume for simplicity their equality so that $n_d \approx b^2/L_x^2$ is considered a scalar.

The average value of the dislocation displacement is given by

$$\langle y(x,t)\rangle = \frac{\int \mathbf{D}y e^{-S_{SG}/\hbar} y}{\int \mathbf{D}y e^{-S_{SG}/\hbar}}. \tag{3.5}$$

In the limit of linear response (small f), we can expand the exp-function in Taylor series and leave only linear in f terms

$$\langle y(x,t)\rangle = \frac{1}{\hbar}\frac{\int e^{-S_0}\mathbf{D}y \int_0^\beta dt' \int_0^{L_x} dx' y(x',t')y(x,t)f}{\int e^{-S_0}\mathbf{D}y}, \tag{3.6}$$

where S_0 includes all the terms in (3.3) but $-fy$ term. Using $f = \sigma_{zy}b$ we conclude that in the limit of linear response (small f) the average displacement is determined by the correlation function with no external field present

$$\langle y(x,t)\rangle = \frac{b}{\hbar}\int_0^\beta dt' \int_0^{L_x} dx' \,\langle y(x',t')y(x,t)\rangle_0 \,\sigma_{zy}. \tag{3.7}$$

Here $\langle ...\rangle_0$ implies the statistical averaging over the action (3.3) with $f = 0$. Thus we obtain that

$$u_{zy} = \frac{n_d}{\hbar L_x}\int_0^\beta dt' \int_0^{L_x} dx \int_0^{L_x} dx' \,\langle y(x',t')y(x,t)\rangle_0 \,\sigma_{zy}. \tag{3.8}$$

To this strain it is also necessary to add the contribution from the elastic response of the ideal crystal given by the bare shear modulus G_{el}: $u_{zy}^{(el)} = G_{el}^{-1}\sigma_{zy}$. Thus the total expression reads $u_{zy}^{(tot)} = G^{-1}\sigma_{zy}$, where the total shear modulus G can be

obtained from

$$\frac{G_{el}}{G(T,q)} = 1 + \gamma \int_0^{\tilde{\beta}} dt \int_0^{N_x} dx \, \langle \theta(x,t)\theta(0,0) \rangle_0 \, . \tag{3.9}$$

Here $\gamma \equiv 4b^2 x_0 n_d G_{el}/(\pi T_0)$, $y = (2b/\sqrt{\pi})\theta$, $x \to x_0 x, t \to t_0 t$ and $x_0/t_0 = V_d$, $\tilde{\beta} = T_0/T$, $N_x = L_x/x_0$, $T_0 = \hbar V_d/x_0$.

The correlator in (3.9) can be obtained numerically and therefore Eq.(3.9) is extremely useful since it provides a bridge between simulation results and an actual experimental data. The discussion of the Eq.(3.9) implementation will be given in Section 5.2.3.

3.2.2 Two states of dislocation: rough and smooth

The model (3.3) is a so-called Sine-Gordon (SG) model, it has been extensively studied in literature [52] and it was shown to exhibit BKT transition at $T = 0$ (see Section.2.2). The transition is possible due to the fact that though our system is a 1D quantum dislocation, its mapping to the classical model with an imaginary time as a second dimension allows to treat it formally as a 2D Coulomb gas as will be shown later (Section 5.1). The transition for Sine-Gordon model happens between *smooth* and *rough* states. Smooth state corresponds to the dislocation with a small amount or no kinks at all, while in rough state kink-antikink pairs are plenty.

The meaning of this transition becomes clear if one compares the energy required to create kink-antikink pair at $T = 0$ with the phonon energy. The first can be obtained from a solution of SG model as $\Delta \approx V_d b\sqrt{n_1 u}$ and the latter is $E_{ph} \approx 2\pi\hbar\sqrt{u}/(b\sqrt{n_1})$. If one considers their ratio $R = E_{ph}/\Delta = \frac{h}{n_1 V_d b^2}$ it is obvious that if $R \ll 1$ the energy of zero-point fluctuations is just too small to create kinks. In the opposite case $R \gg 1$, however, it is more than enough and dislocation will be in a

rough state. For most materials $R \ll 1$ so the defects are in smooth state, but for quantum crystals the situation is different. For ^{4}He, as an example, taking $b \approx 3.5\mathring{A}$, typical speed of sound as $V_d \approx 300m/s$, $bn_1 \approx m_0$ - the mass of a single ^{4}He atom, the ratio turns out to be $R \approx 1$, which suggests that in solid ^{4}He at $T = 0$ the dislocations can be in a quantum rough state.

Extending the analogy between Coulomb gas and dislocation transitions one should notice that the dislocation *smooth* state corresponds to the *plasma* state in the gas, where charges unbind and become screened from each other with a finite screening length. *Rough* state is equivalent to the *insulating* phase in gas, where charges bind together into neutral pairs.

It is necessary to understand that the model (3.3) is reduced to the Granato-Lücke free string in the case of a *rough* dislocation since such a state renders the Peierls potential irrelevant. For a string of length L_x with strongly pinned ends the average displacement would be

$$\langle y \rangle \approx \frac{x(L_x - x)}{2n_1 V_d^2} f. \tag{3.10}$$

For a *smooth* dislocation, however, the Peierls potential plays an essential role: it tries to localize the string to one of its valleys. Dislocation motion is limited by small deviations $|y| \leq b$ and its displacement as a response to small external static force f will be small and independent of dislocation length

$$\langle y \rangle \approx \frac{b^2}{4\pi^2 u} f. \tag{3.11}$$

It will be proved later (Section 5.2.2) that in solid ^{4}He dislocation is in smooth state at $T = 0$ due to the effect of long-range interaction. Therefore, the next question arises: how does the smooth/rough transition happens as you increase the tempera-

ture? At any finite T thermal fluctuations make it possible to create kink-antikink pairs with probability $\sim \exp(-\Delta/T)$, where Δ is the effective energy of the kink-antikink pair. Hence one may say that the dislocation becomes rough at any finite T at all. However for $T \ll \Delta$ the amount of such pairs is negligible, so one may safely assume that the dislocation remains in a smooth state in a region $0 \leq T \leq \Delta$. The nature of the crossover which should happen at $T \sim \Delta$ will be considered in Section 5.2.3.

Chapter 4

Monte-Carlo method

4.1 Simulation details: Monte-Carlo method and Metropolis algorithm

Computer simulations based on Monte-Carlo technique are widely used and are the most efficient method in treating systems containing a large number of elements [53]. Basically, we will be interested in the quantities averaged over the large number of system states. To find it, we actually have to perform two long summations

$$\langle A \rangle = Z^{-1} \sum_{\{\upsilon\}} A(\upsilon) W(\upsilon), \qquad Z = \sum_{\{\upsilon\}} W(\upsilon), \tag{4.1}$$

where the sum runs over all possible states. This is the expression for an average value of A over all possible system configurations considering that each configuration is included the probability $p(\upsilon) = W(\upsilon)/Z$, which is called a configuration weight. If the energy of every configuration is given by E_υ then the configuration weight is $W(\upsilon) = e^{-E_\upsilon}$ The formal strategy in Monte-Carlo simulations is run over all possible system configurations, computing two long sums. The problem here is that

the number of terms in these sums is literally huge even for small systems. The good thing is though that in thermal equilibrium most of the states have extremely small W and do not add significant contribution to the summation, therefore, we have to find a way to choose only the most important states while performing calculations, that is to select configurations with probabilities proportional to their weight. The way to do so is provided by the Metropolis algorithm [54]. Metropolis et al. suggested replacing original summation over all possible configurations with the stochastic one

$$\frac{\sum\limits_{\upsilon} A\left(\upsilon\right) W\left(\upsilon\right)}{\sum\limits_{\upsilon} W\left(\upsilon\right)} \rightarrow \frac{\sum_{\upsilon}^{\prime} A(\upsilon)}{\sum_{\upsilon}^{\prime}}, \tag{4.2}$$

where configurations υ are included into the sum with certain probabilities (proportional, actually, to $W\left(\upsilon\right)$). The expression for $A\left(\upsilon\right)$ is called an *estimator*. The main equation that should be satisfied is a so-called balance equation which tells us the exact relation between the probability of accepting the new configuration into the sum and the ratio of configuration weights.

$$W\left(\upsilon\right) \sum_{\upsilon^{\prime},u} p_u P_u^{acc}(\upsilon \rightarrow \upsilon^{\prime}) = \sum_{\upsilon^{\prime},u} W\left(\upsilon^{\prime}\right) p_{\bar{u}} P_u^{acc}(\upsilon^{\prime} \rightarrow \upsilon). \tag{4.3}$$

Here p_u is the probability of applying update u in the simulation and $P_u^{acc}(\upsilon \rightarrow \upsilon^{\prime})$ is the probability that the modification suggested by u is actually accepted. The latter is also called the *acceptance probability*. To satisfy this equation is a tricky part of the problem since one can think of infinitely many ways to choose the update. The easiest way to do that is to *balance flow* between arbitrary pairs of configurations. Then one says that the pair is balanced if

$$\frac{P_u^{acc}(\upsilon \rightarrow \upsilon^{\prime})}{P_u^{acc}(\upsilon^{\prime} \rightarrow \upsilon)} = \frac{W\left(\upsilon^{\prime}\right)}{W\left(\upsilon\right)} \frac{p_{\bar{u}}}{p_u} = R, \tag{4.4}$$

where R is called an acceptance ratio. This equation can be satisfied if we choose

$$\begin{aligned} P_{acc}\left(\upsilon \to \upsilon'\right) &= \begin{cases} R & if\ R < 1 \\ 1 & if\ R \geqslant 1 \end{cases} \\ P_{acc}\left(\upsilon' \to \upsilon\right) &= \begin{cases} 1 & if\ R \leqslant 1 \\ 1/R & if\ R > 1 \end{cases} \end{aligned} \tag{4.5}$$

So if a generated random number is smaller than P_{acc} then the new configuration is implemented in the summation. It is clear that if $P_{acc} = 1$ new configuration is accepted automatically.

4.2 Worm algorithm for Ising model

The J-current model [55] is a classical statistical model of conserved currents on a lattice. It was first suggested by Wallin *et al.* [56] to study quantum-phase transitions in bosonic systems by using path-integral mapping of a d-dimensional bosonic quantum system to a $d+1$-dimensional classical statistical model. In most simulations done in this work we will be using so-called Worm Algorithm (WA)[57]. This method was proposed to eliminate critical slowdown of the convergence times around critical points. The main idea of this method is to introduce the configuration space of closed paths (CP) to collect the statistics of the model. It was shown that the efficiency of sampling is dramatically increased for such classical statistical models as 2D and 3D Ising models, 2D and 3D XY models, and Gaussian model since the autocorrelation times $\tau(L)$ scale for them as $\tau(L) = \tau_0 + c\ln(L)$ with the size of the system L. For Metropolis updates connecting configurations by a Markovian chain τ scales like $\tau \sim L^z$ with $z = 2$ for most systems. Therefore the worm algorithm provides a crucial acceleration for these models since it gives z close to 0 for them [57]. Implementation of WA for $q = 3$ Potts model in 2D resulted in τ scaling like a power law with $z \approx 0.55$.

To introduce the idea, let's consider its application to Ising model:

$$-\frac{H}{T} = \sum_{b=<ij>} H_b, \quad H_b = K s_i s_j. \tag{4.6}$$

Here $K = J/T$ - the dimensionless parameter characterizing the coupling strength between spins $s_i = \pm 1$, and the summation runs over all bonds b between neighboring sites i and j. Expanding an exp-function in a Taylor series we arrive at

$$e^{-\frac{H}{T}} = \prod_b \left(\sum_{N_b=0}^{\infty} \frac{K^{N_b}(s_i s_j)^{N_b}}{N_b!} \right). \tag{4.7}$$

The summation runs over bonds N_b and the composition $\{N_b\}$ is referred to as a "bond configuration". We can rewrite the sum over spins as $\prod_i \left(\sum_{s_i=\pm 1} s_i^{k_i}\right) = \prod_i Q(k_i)$, where $k_i = \sum_\nu N_{i,\nu}$ is the sum of bond states starting from site i. This representation allows then to reformulate the problem completely in terms of bond states [57] and the partition function assumes the form

$$Z \equiv \sum_{\{s_i\}} \sum_{\{N_b\}} \prod_b \frac{K^{N_b}}{N_b!} (s_i s_j)^{N_b} = \sum_{\{N_b\} \in CP} W_Z(\{N_b\}), \tag{4.8}$$

where bond configuration weight is given by

$$W_Z(\{N_b\}) = \left(\prod_b \frac{K^{N_b}}{N_b!} \right) \left(\prod_i Q(k_i) \right). \tag{4.9}$$

If one imagines a two-dimensional lattice with all neighboring sites connected to each other by bonds then N_b is the number of lines on the bond b. The summation in (4.8) runs over only the closed paths bond configurations that is the number of bond lines associated with any given site should be even.

If we try to calculated the correlation function

$$G(i_1 - i_2) = < s_{i_1} s_{i_2} > = \frac{\sum_{\{s_i\}} s_{i_1} s_{i_2} e^{-H/T}}{Z} \tag{4.10}$$

a little bit different situation arises: the configuration space P_g consists not only of closed paths, but it also allows two special sites i_1 and i_2 to have an odd number of bond lines connected to it. These two sites are the only ones where the "open" path is allowed to start and start. To obtain new configurations a space motion of

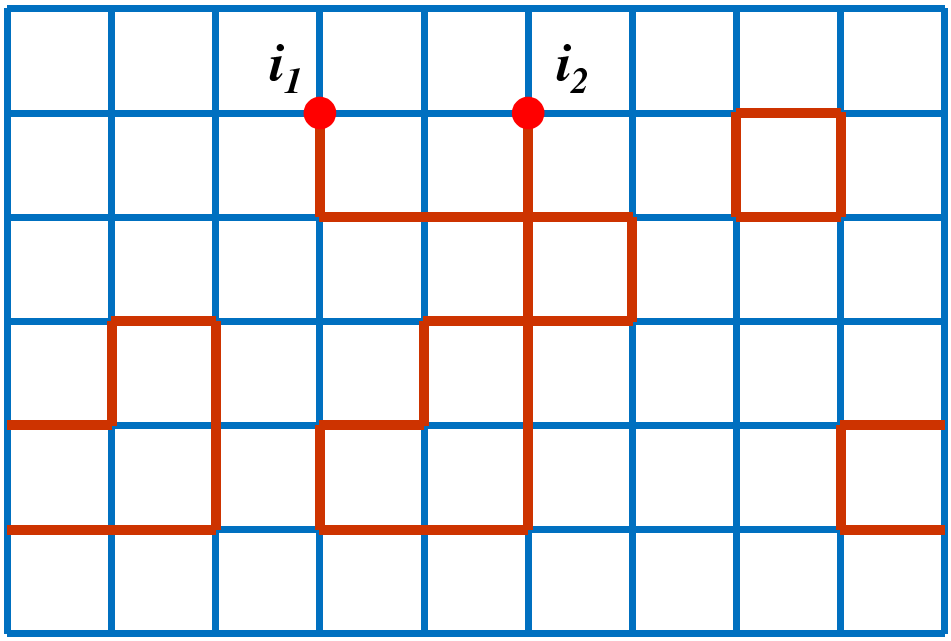

Figure 4.1: Sample of the configuration space for a WA procedure: it contains two closed paths and one open path, which begins and ends on sites i_1 and i_2 correspondingly.

these two sites is suggested and two elementary updates are attempted: if $i_1 \neq i_2$ we propose to shift i_1, and if $i_1 = i_2$ (CP configuration) we propose to "shift" i_1 with probability p_0 or "move" both end points with probability $p = 1 - p_0$ to a new site i_0 chosen randomly. The example of the WA configuration space is depicted on Fig. 4.1.

The usual scheme of the algorithm implementation consists of choosing the initial bond configuration $\{N_b\}$ and then performing the cycle of the usual Metropolis updates. The initial $\{N_b\}$ is usually chosen to be 0 or a certain configuration obtained previously for this system for a specific set of parameters. The latter is used in the study of, for example, hysteresis behavior (like the results obtained in Section 7). The procedure is the following:

1) Select an update: either "move" or "shift" depending on whether $i_1 = i_2$ or not (described above);

2) Calculate the acceptance ratio, and, if accepted, change the configuration;

3) Collect the statistics for necessary MC quantities;

4) Return to step (1).

This update scheme proved to be very successful in acquiring the information about the dislocation properties, at it will be shown later.

Chapter 5

Glide of dislocation with long-range interaction

5.1 Mapping of a dislocation to the Coulomb gas.

In this section we will consider a dislocation using Coulomb gas approach and first we will show how the dislocation line can be viewed as gas of interacting charges.

Let's consider a gliding edge dislocation which can move in the periodic potential provided by the lattice. We will use a Granato-Lüke description (3.3) with an addition of Peierls potential. Let's also introduce a long-range interaction between distant kinks [45, 49].

Our problem is a 1D quantum problem. However using Feynman path integral formalism it is possible to map a quantum system to a classical statistical model [58]. The price to pay for it is an extra dimension of imaginary time τ. This extra variables has a maximum value of inverse temperature $\beta = 1/T$ and can be treated in calculations no different from space variable. Therefore we make the mapping of our one-dimensional quantum problem to the classical one in 1+1 dimensions with

the classical action for a membrane:

$$S = \int dxdt \Bigg(\frac{1}{2K} ((\nabla_x y)^2 + (\nabla_t y)^2) - 2\alpha \cos\left(\sqrt{16\pi} y\right) + \\ + \int dx' dt' \vec{\nabla} y(x,t) V(x-x', t-t') \vec{\nabla} y(x',t') \Bigg), \tag{5.1}$$

where $y(x,t)$ is the dislocation displacement (the core is oriented along x-axis). The constants K and α are related to the physical properties of the system. The long-ranged potential is induced by the deformations of the host lattice and it has the asymptotics

$$V(x,t) \propto \frac{1}{x^2+t^2} \propto \frac{1}{r^2}, \tag{5.2}$$

where $r^2 = x^2 + t^2$. The interaction between the static kinks $V(x) = \int dt V(x,t) \propto \frac{1}{|x|}$ has been discussed in the literature [45, 49]. The action written on the discrete space-time lattice is

$$E = \frac{1}{2K} \sum_{\langle i,j \rangle} (y_i - y_j)^2 + C \sum_{\langle i,j \rangle} \sum_{\langle k,m \rangle} (y_i - y_j)(y_k - y_m) V(|\mathbf{r}_i - \mathbf{r}_k|) - \\ - 2\alpha \sum_i \cos\left(\sqrt{16\pi} y_i\right) = H_0 - 2\alpha \sum_i \cos(\sqrt{16\pi} y_i), \tag{5.3}$$

where

$$H_0 = \frac{1}{2K} \sum_{\langle i,j \rangle} (y_i - y_j)^2 + C \sum_{\langle i,j \rangle} \sum_{\langle k,m \rangle} (y_i - y_j)(y_k - y_m) V(|\mathbf{r}_i - \mathbf{r}_k|). \tag{5.4}$$

Here y_i is displacement of dislocation at site i, C gives the strength of long-range interaction and $< ij >$ means a summation over nearest neighboring sites . The

summation in first term runs over the nearest neighbor sites, and therefore it is a short-ranged term. It describes only the interaction between two nearest sites in the dislocation. The third term is a Sine-Gordon action describing the interaction of the dislocation with the crystal lattice periodic field. The behavior of dislocation in the presence of long-ranged interaction (the second term) has not been studied before and will be examined in Section 5.2.

Let us apply Fourier transform to the first two terms:

$$\sum_{\langle i,j\rangle}\left(y_i-y_j\right)^2=4\sum_q\left|y\left(q\right)\right|^2\left(\sin^2\left(\frac{q_x}{2}\right)+\sin^2\left(\frac{q_y}{2}\right)\right), \tag{5.5}$$

$$\sum_{\langle i,j\rangle}\sum_{\langle k,m\rangle}\left(y_i-y_j\right)\left(y_k-y_m\right)V(|\mathbf{r}_i-\mathbf{r}_k|)=\sum_q|y(q)|^2\hat{V}(q)\left(\sin^2\left(\frac{q_x}{2}\right)+\sin^2\left(\frac{q_y}{2}\right)\right), \tag{5.6}$$

where $\hat{V}(q)$ is the Fourier transform of the potential $V(x,t)$.

Thus we obtain

$$H_0=\frac{2}{K}\sum_q\left|y\left(q\right)\right|^2\left(1+\hat{V}(q)\right)\left(\sin^2\left(\frac{q_x}{2}\right)+\sin^2\left(\frac{q_y}{2}\right)\right). \tag{5.7}$$

.

Our partition function is

$$Z=\int\mathbf{D}ye^{-H_0}e^{2\alpha\sum_i\cos(\sqrt{16\pi}y_i)} \tag{5.8}$$

. We expand the second exponent in Taylor series and apply binomial formula:

$$\exp(2\alpha\sum_i \cos(\sqrt{16\pi}y_i)) =$$
$$= \prod_i \sum_{N_i} \frac{(2\alpha)^{N_i}}{N_i!}\left(\cos(\sqrt{16\pi}y_i)\right)^{N_i} = \prod_i \sum_{N_i} \frac{(2\alpha)^{N_i}}{2^{N_i}N_i!}\left(e^{i\sqrt{16\pi}y_i}+e^{-i\sqrt{16\pi}y_i}\right)^{N_i} =$$
$$= \prod_i \sum_{\{N_i^+,N_i^-\}} \frac{(\alpha)^{N_i}}{N_i^+!N_i^-!}\left(e^{i\sqrt{16\pi}y_i}\right)^{N_i^+}\left(e^{-i\sqrt{16\pi}y_i}\right)^{N_i^-} = \prod_i \sum_{\{N_i^+,N_i^-\}} \frac{\alpha^{N_i^++N_i^-}}{N_i^+!N_i^-!}e^{i\sqrt{16\pi}y_i\left(N_i^+-N_i^-\right)} =$$
$$= \sum_{\{N_i^+,N_i^-\}}\left(\prod_i \frac{\alpha^{N_i^++N_i^-}}{N_i^+!N_i^-!}\right)e^{i\sum\limits_i \sqrt{16\pi}y_i m_i} = \sum_{\{N_i^+,N_i^-\}}\left(\prod_i \frac{\alpha^{N_i^++N_i^-}}{N_i^+!N_i^-!}\right)e^{i\sqrt{16\pi}\sum\limits_q m_q^* y_q}, \tag{5.9}$$

where we introduced the notation $N_i^+ - N_i^- = m_i$.

Now we have

$$Z = \int \mathbf{D}y e^{-\frac{2}{K}\sum\limits_q |y(q)|^2\left(\left(1+\hat{V}(q)\right)\left(\sin^2\left(\frac{q_x}{2}\right)+\sin^2\left(\frac{q_y}{2}\right)\right)\right)} \sum_{\{N_i^+,N_i^-\}}\left(\prod_i \frac{\alpha^{N_i^++N_i^-}}{N_i^+!N_i^-!}\right)e^{i\sqrt{16\pi}\sum\limits_q m_q^* y_q} =$$
$$= \sum_{\{N_i^+,N_i^-\}}\left(\prod_i \frac{\alpha^{N_i^++N_i^-}}{N_i^+!N_i^-!}\right)\int \mathbf{D}y e^{-\sum\limits_q (2k_q|y(q)|^2+i\sqrt{16\pi}m_q^* y_q)}, \tag{5.10}$$

where we introduced the notation $k_q = \frac{1}{K}\left(1+\hat{V}(q)\right)\left(\sin^2\left(\frac{q_x}{2}\right)+\sin^2\left(\frac{q_y}{2}\right)\right)$ with $\hat{V}(\mathbf{q}) = \int d\mathbf{r}e^{i\mathbf{qr}}V(\mathbf{r}) = C\ln\left(1+\frac{Q_0^2}{q_x^2+q_y^2}\right)$.

Performing Gaussian integration, we finally obtain

$$Z = \sum_{\{N_i^+,N_i^-\}}\left(\prod_i \frac{\alpha^{N_i^++N_i^-}}{N_i^+!N_i^-!}\right)e^{-16\pi\sum\limits_q \frac{|m_q|^2}{8k_q}}. \tag{5.11}$$

Using $|m_q|^2 = \frac{1}{N}\sum\limits_{i,j} m_i m_j e^{-iq(x_i-x_j)}$, we transform the partition function as follows

$$Z = \sum_{\left\{N_i^+, N_i^-\right\}} \left(\prod_i \frac{\alpha^{N_i^+ + N_i^-}}{N_i^+! N_i^-!} \right) e^{-\sum\limits_q \frac{16\pi}{8k_q N} \sum\limits_{i,j} m_i m_j e^{-iq\left(\mathbf{x}_i - \mathbf{x}_j\right)}} =$$
$$= \sum_{\left\{N_i^+, N_i^-\right\}} \left(\prod_i \frac{\alpha^{N_i^+ + N_i^-}}{N_i^+! N_i^-!} \right) e^{-\frac{1}{2} \sum\limits_{i \neq j} m_i m_j U(\mathbf{x}_i - \mathbf{x}_j)}, \tag{5.12}$$

where

$$U\left(\mathbf{x}\right) = \frac{4\pi K}{N} \sum_{-\frac{\pi}{a} \leqslant q_{x,y} \leqslant \frac{\pi}{a}} \frac{e^{iq_x x + iq_y y}}{\left(1 + V(\mathbf{q})\right) \left(\sin^2\left(\frac{q_x}{2}\right) + \sin^2\left(\frac{q_y}{2}\right)\right)}. \tag{5.13}$$

The exponential of Z is, therefore,

$$E = \frac{1}{2} \sum_{i \neq j} m_i m_j U(\mathbf{x}_i - \mathbf{x}_j) \tag{5.14}$$

which looks exactly like the energy of the system of charges m_i interacting via the potential $U(\mathbf{x}_i - \mathbf{x}_j)$. Consequently, in the future we will call m_i charges.

We can see, that in the absence of long-ranged interaction term (that is $C = 0$), the potential is (dropping unessential constants)

$$U(\mathbf{x}) = \frac{16\pi K}{N} \sum_{\mathbf{q}} \frac{e^{i\mathbf{q}\cdot\mathbf{x}}}{q^2} = \frac{16\pi K}{(2\pi)^d} \int \frac{e^{i\mathbf{q}\cdot\mathbf{x}}}{q^2} d^d q. \tag{5.15}$$

In three dimensions the potential dies with the distance as $U(\mathbf{x}) \xrightarrow[d=3]{} \sim \frac{1}{|\mathbf{x}|}$ In two dimensions $U(\mathbf{x}) \sim \int\limits_0^\infty \frac{e^{i\mathbf{q}\cdot\mathbf{x}}}{q^2} d^2 q$ it diverges at zero, but the behavior of the integral can be improved by noticing, that $\sum\limits_{i \neq j} m_i m_j U(\mathbf{x}_i - \mathbf{x}_j) = \sum\limits_{i \neq j} m_i m_j \left(U(\mathbf{x}_i - \mathbf{x}_j) - U(0)\right) + U(0) \sum\limits_i m_i$ The last term should disappear due to the charge neutrality condition, so $U(\mathbf{x}) \sim \int\limits_0^\infty \frac{\left(e^{i\mathbf{q}\cdot\mathbf{x}} - 1\right)}{q^2} d^2 q$ To avoid divergence on the upper limit we impose the limit of

the integration $1/a$ (first Brillion zone). Now

$$U(\mathbf{x}) \sim \int_0^{1/a} \frac{(e^{i\mathbf{q}\cdot\mathbf{x}}-1)}{q^2} d^2q = \int_0^{1/a} dq \int d\phi \frac{\left(e^{iqx\cos\phi}-1\right)}{q^2 2\pi} q = \int_0^{1/a} \frac{dq}{q} \int d\phi \frac{\left(e^{iqx\cos\phi}-1\right)}{2\pi} =$$
$$= \int_0^{x/a} \frac{d(qx)}{qx} (J_0(qx)-1) = \int_0^1 \frac{d(y)}{y} (J_0(y)-1) + \int_1^{x/a} \frac{d(y)}{y} (J_0(y)-1) = const - \ln\frac{x}{a} \propto$$
$$\propto -\ln\frac{x}{a}, x >> a. \tag{5.16}$$

Thus, in case $V(x,t)=0$ the partition function is

$$Z = \sum_{\left\{N_i^+, N_i^-\right\}} \left(\prod_i \frac{\alpha^{N_i^+ + N_i^-}}{N_i^+! N_i^-!} \right) e^{\frac{8K}{2} \sum\limits_{i\neq j} m_i m_j \ln \frac{\left|\mathbf{x}_i - \mathbf{x}_j\right|}{\mathbf{x}_0}}. \tag{5.17}$$

The energy is logarithmic which means that the system exhibits Berezinskii Kosterlitz-Thouless (BKT) transition (at $K = 1/2$).

The key question arises: what happens in the presence of long-ranged interaction? How the potential $V(x,t)$ modifies the transition? To make an assumption we should consider the asymptotic behavior of the potential

$$U(\mathbf{r}) \xrightarrow[r>>1]{} \iint dq_x dq_y \frac{e^{iq_x x + iq_y y}}{\left(q_x^2+q_y^2\right)\left(1 + C\ln\left(1+\frac{Q_0^2}{q_x^2+q_y^2}\right)\right)} =$$
$$= \int dQ \frac{J_0(Qr)}{Q\left(1 + C\ln\left(1+\frac{Q_0^2}{Q^2}\right)\right)} \propto \ln(\ln(r)), \tag{5.18}$$

where $Q^2 = q_x^2 + q_y^2$ and $J_0(Qr)$ is the Bessel function.

As it was shown before (see Section 2.2) BKT transition is possible in 2D system

if the interaction potential has an asymptotic behavior of the form $U(\vec{r}) \to \ln r$ as $r \to \infty$, where $r = \sqrt{x^2 + t^2}$. Such dependence is needed to balance an entropic term in free energy (2.9). However, as Eq. (5.18) shows the potential in case of a long-range interaction is decaying much slower than $\ln r$, which means, according to the Kosterlitz-Thouless heuristic argument, that the charges in the Coulomb gas must be deconfined as long as $C \neq 0$. Therefore even for small values of C the Coulomb gas will be in plasma state, corresponding to the smooth state of the dislocation (the analogy between states in Coulomb gas and dislocations was discussed in Section 3.2.2). Thus we would anticipate to see the suppression of zero-point kinks for any *arbitrary* small long-range interaction in the thermodynamical limit $T \to 0$ and $L_x \to \infty$.

To test this assumption by simulations we should calculate the correlation function with a partition function given by (5.12)– (5.14). After performing simulations it was found that Coulomb gas approach is not efficient for this problem. The details of the obtained results are discussed at length in Appendix A.

The results obtained from the simulations of dual J-current model turned out to be much more promising. The convergence is much better, and, thus, we conclude that the J-current model is superior to the Coulomb gas model. We will use it to perform simulations.

5.2 Glide of dislocation: duality approach

5.2.1 Model

As it was mentioned before the duality approach for a gliding dislocation proved to be far superior method for simulating the dislocation line. We used it henceforth.

Let's go back a little and rewrite the full action using a little bit different notations ($\hbar = 1$,$K_B = 1$):

$$S_{SG} = \sum_{Q=(\omega,q_x)} \{\frac{1}{2K} Q^2[1 + C \ln\left(1 + \frac{Q_0^2}{Q^2}\right)]|y_Q|^2\} - \\ - \int_0^{Nx} dx \int_0^{\beta} dt\, u_P \cos(\sqrt{16\pi}\, y), \tag{5.19}$$

where $Q_0 \approx 1$, C gives the strength of long-range interaction, u_P described the Peierls potential – periodic potential, provided by the lattice, $\beta = T_0/T$, $T_0 = \hbar V_d/b$, $\omega = (2\pi/\beta)n, n = 0, 1, 2...$, q_x is a spatial wave vector along the core of length L_x, $K = 1/(n_1 V_d b^2)$, n_1 - 1d mass density, V_d - speed of sound along the sting. $Q^2 = \omega^2 + q_x^2$. The first part is written in Fourier and the last in x, t coordinates. The model is written so that the KT transition occurs at $K = 1/2$ for $C = 0$. The long-range potential is introduced according to [45, 49].

In simulations periodic boundary conditions are assumed $y(x+L_x, t) = y(x, t)$,$y(x, t+\beta) = y(x, t)$.

The cos-term in (5.19) on a lattice, where the integration over x and t is replaced by the summation over all lattice sites i, can be simplified by using Villain approximation [59]. It comes from the fact that periodic cos-function can be replaced by the periodic guassian which has the minima at the same places $\sqrt{16\pi}y = 2\pi m$ with the same curvatures [60]. Then the partition function of the system containing cos-term is

transformed as follows

$$Z = \int \mathbf{D}y e^{-S_{SG}} = \int \mathbf{D}y \exp\left(-S_0 + \sum_i u_P \cos(\sqrt{16\pi}\, y_i)\right) \rightarrow$$
$$\sum_{\{m_i\}} \int \mathbf{D}y e^{-S_0} \exp\left(-\frac{u_P}{2} \sum_i \left(\sqrt{16\pi} y_i - 2\pi m_i\right)^2\right). \tag{5.20}$$

Now applying Poisson summation formula we obtain

$$Z = \sum_{n_i} \int \mathbf{D}m \mathbf{D}y e^{-\sum_{q_x,\omega} \frac{1}{2K_q}|y_q|^2 - \frac{u_P}{2}\sum_i \left(\sqrt{16\pi} y_i - 2\pi m_i\right)^2 + 2\pi i m_i n_i}, \tag{5.21}$$

where

$$K_q = \frac{K}{1 + C \ln\left(1 + \frac{Q_0^2}{Q^2}\right)}, \quad Q^2 \equiv q_x^2 + \omega^2. \tag{5.22}$$

Calculating integrals over m and y as gaussian we arrive at

$$Z = \sum_{\{n\}} \exp\left[-\frac{1}{2} \sum_{q_x,\omega} |n_q|^2 \left(\frac{1}{u_P} + \tilde{U}_{SG}(q_x, \omega)\right)\right], \tag{5.23}$$

where

$$\tilde{U}_{CG}(q_x, \omega) = \frac{16\pi K}{Q^2 \left(1 + C \ln\left(1 + \frac{Q_0^2}{Q^2}\right)\right)}. \tag{5.24}$$

Thus we reformulated our problem as a Coulomb gas with charges n_i "living" on the lattice sites i and interacting through some potential $\tilde{U}_{SG}$ which is derived from our original quantum mechanical problem.

The expression (5.23) allows an exact mapping to J-current model. The action in the dual representation can be written as

$$S_J = \frac{1}{2} \sum_{i,j} \vec{J}_i U_d(\vec{x}_i - \vec{x}_j) \vec{J}_j, \tag{5.25}$$

where $\vec{J}_i = j_i^\nu$ are integer bond currents obeying Kirchhoff's conservation law. Here $\nu = \pm\hat{x}, \pm\hat{t}$ are defined on each bond leaving site i and $\hat{x}, \hat{t}$ are unit vectors.

Duality is based on introducing a dual lattice with sites located at centers of squares of the original lattice and expressing currents as $\vec{J} = \vec{\nabla} \times \phi$, where ϕ are integer numbers. The graphical representation is displayed on Fig.5.1.

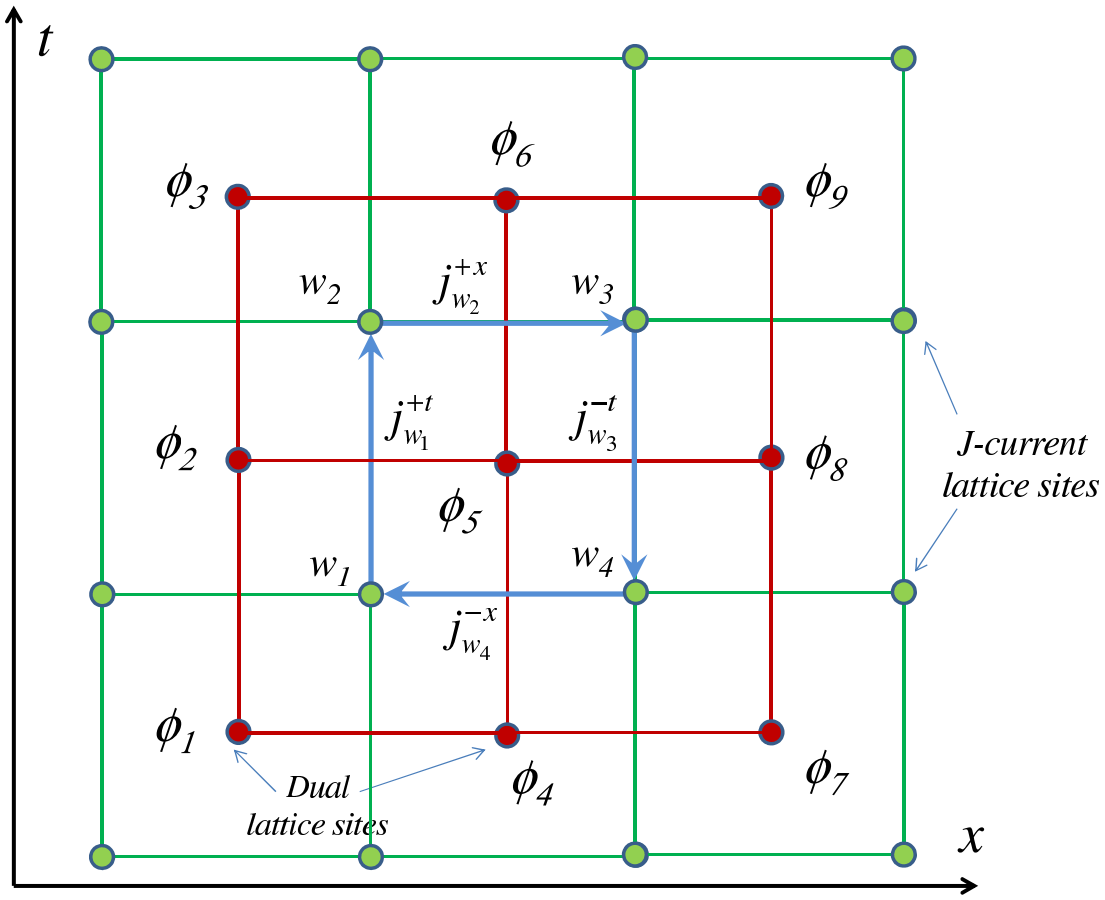

Figure 5.1: Duality transformation for J-current representation. The dual lattice ϕ is positioned in the centers of squares of the original lattice so that $\vec{J} = \vec{\nabla} \times \phi$. Blue arrows represent the smallest J-current loop.

In particular, for the small J-current loop connecting sites w_1, w_2, w_3 and w_4 on

the shown picture, this means the following relations

$$\begin{aligned} j_{w_1}^{+\hat{t}} &= \phi_2 - \phi_5 \\ j_{w_2}^{+\hat{x}} &= \phi_6 - \phi_5 \\ j_{w_3}^{-\hat{t}} &= \phi_5 - \phi_8 \\ j_{w_4}^{-\hat{x}} &= \phi_5 - \phi_4. \end{aligned} \tag{5.26}$$

Using Eqs.(5.26) and (5.25) one can write the partition function as

$$Z = \sum_{\{\phi\}} \exp\left(-\sum_{q_x,\omega} |\hat{\phi}_{\vec{q}}|^2 (q_x^2 + \omega^2) \tilde{U}_d(q_x,\omega) \right). \tag{5.27}$$

Using Poisson's summation formula and integrating out ϕ one obtains

$$\begin{aligned} Z &= \sum_{\{n\}} \int \mathbf{D}\phi \exp\left(\sum_{q_x,\omega} \left[-|\hat{\phi}_{\vec{q}}|^2 (q_x^2 + \omega^2) \tilde{U}_d(q_x,\omega) + 2\pi i n_{\vec{q}} \phi_{-\vec{q}} \right] \right) \\ &= \sum_{\{n\}} \exp\left(-\frac{1}{2} \sum_{\vec{q}} \frac{2\pi^2 |n_q|^2}{(q_x^2 + \omega^2)\tilde{U}_d(q_x,\omega)} \right). \end{aligned} \tag{5.28}$$

The partition function for J-current model in (5.28) looks *exactly the same* as the partition function for Coulomb gas representation in (5.23) provided we choose interaction potentials properly. Comparing (5.23) and (5.28) we find that $\tilde{U}_d(q_x,\omega)$ should be expressed as

$$\tilde{U}_d(q_x,\omega) = \frac{(2\pi)^2}{(\omega^2 + q_x^2)(u_P^{-1} + \tilde{U}_{CG}(q_x,\omega))}, \tag{5.29}$$

where $\tilde{U}_{CG}$ is the interaction potential from CG model (5.24).

It should be emphasized that Coulomb gas and J-current models are dual representations of *the same system*, and can be both implemented in MC. However, J-current

proved to be quite superior to Coulomb gas approach. The data below were obtained by applying Worm Algorithm [57] to the model (5.25) and have been published in [62].

5.2.2 Simulation results at $T = 0$

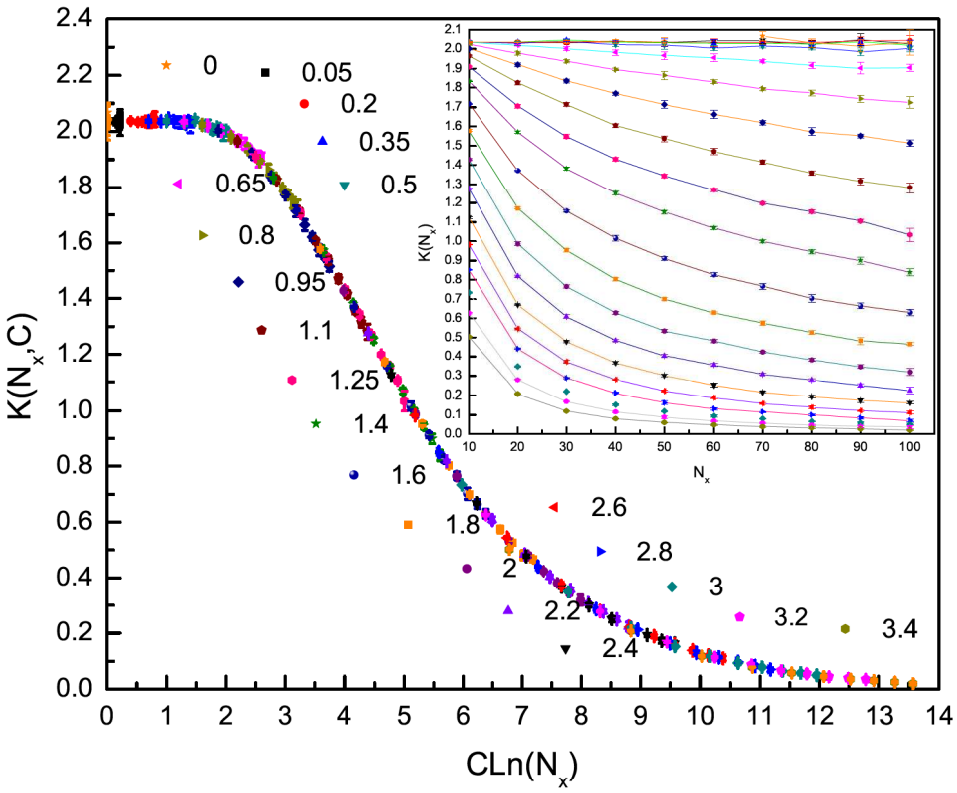

Figure 5.2: Stiffness $K(N_x, C)$ at $T = 0$ as a function of $C \ln N_x$. Displayed numbers are C-values. On the inset: family of curves $K(N_x, C)$ for various C [62].

MC simulations of a dual action (5.25) have utilized Worm Algorithm [57] and were conducted on square lattice $N_x = N_t$ with unit lattice spacings. Since BKT in our variable happens at $K = 1/2$, we used $K = 1.6$ – the value well above the transition which would put the dislocation in a rough state at $C = 0$. The compressibility of the system κ was measured in terms of the winding numbers $\kappa \equiv \frac{<W_t^2>}{TL_x}$, where

winding $W_t = \sum_i J_i^{\hat{t}}/N_t$ is the total current in t direction. The renormalized stiffness at $q_x = w\pi/N_x$ for $N_x \gg 1$ can be given as $K(N_x, C) = \kappa(1 + C \ln\left(1 + \frac{Q_0^2}{q_x^2}\right))$. The dependences of $K(N_x)$ on the dislocation size N_x for different values of C are shown on the inset in Fig. 5.2 [62]. The value of C increases for curves from up to down. As one can see, the compressibility is getting more and more suppressed with size as C grows. All the data on the inset (obtained for different C) can be collapsed on one master curve $K(N_x, C) = F(C \ln N_x)$ (the main graph in Fig. 5.2) where $F(\xi)$ is some function which asymptotically reaches zero. This means that the data obtained for any *arbitrary* small long-range interaction strength C will be a part of this curve if we go to high enough sizes N_x.

The suppression of compressibility signifies that the dislocation is in smooth state at $T = 0$ in the presence of long-range interaction. This statement agrees with our prediction obtained by heuristic argument (Section. 5.1).

It is important to mention that the above conclusion does not depend on the variations of Peierls potential or the change of atoms statistics so the result holds for the dislocation in any crystal (ex., solid ^{3}He).

5.2.3 Shear modulus softening

In this section we present our findings about the dislocation thermal roughening and its connection to the shear modulus experiments [20, 28].

At small temperatures the spectrum of normal excitations of the dislocation is gapped (see Section 3.2.2) which means that shear modulus $G(T)$ will have a plateau at $T \leq \Delta$ and start change significantly only for $T \geq \Delta$. At higher T compressibility κ will reach its asymptotic value κ_∞.

As it was mentioned before (Section 3.2.1), the typical response of a dislocation

network to the applied small stress $f \approx \sigma_{zy} b$ results in the shear modulus changes as

$$\frac{1}{G(T, L_x)} = \frac{1}{G_0} + \frac{b^2}{L_y L_z \hbar} \int_0^\beta dt \int_0^{L_x} \langle y(x,t) y(0,0) \rangle \,. \tag{5.30}$$

After mapping our system to J-current model, we can reformulate the expression for G as

$$G(T, L_x) = \frac{G_0}{1 + \gamma \kappa(T, L_x)} \quad \kappa(T, L_x) \equiv \frac{< W_\tau^2 >}{T L_x}, \tag{5.31}$$

where $\gamma \approx b^4 G_0$ is a constant and κ is a compressibility of J-current model. W_τ are so-called "winding numbers" defined by the total currents in t-direction

$$W_\tau = \sum_i \frac{J_i^{(\tau)}}{N_\tau}. \tag{5.32}$$

MC simulations of the model (5.25) were done for different $T = T_0/(\Delta_t N_t)$ for fixed N_x. For comparison we used data [20](Fig.2.1) obtained for 2000 Hz since they contained the least noise. The experimental curve was fit by

$$G = \frac{G_0}{1 + \frac{\kappa(T/T_\Delta)}{\kappa_\infty} \left(\frac{G_0}{G_\infty} - 1 \right)} \tag{5.33}$$

and the results are presented on Fig 5.3 where we have taken $G_0/G_\infty - 1 = 0.089$ from the experiment [20]. It turned out that all our data can be collapsed on a single master curve by just rescaling the temperature $T \to T/T_\Delta$, T_Δ being the temperature around which the dislocation softens. T_Δ can also be considered as a typical energy of the kink $\Delta \equiv \Delta(K, C, \alpha, N_x)$ for at least low T, where K is the Luttinger parameter, α is used for strength of Peierls potential. Therefore, the shear modulus softening is controlled by *one* parameter – kink energy.

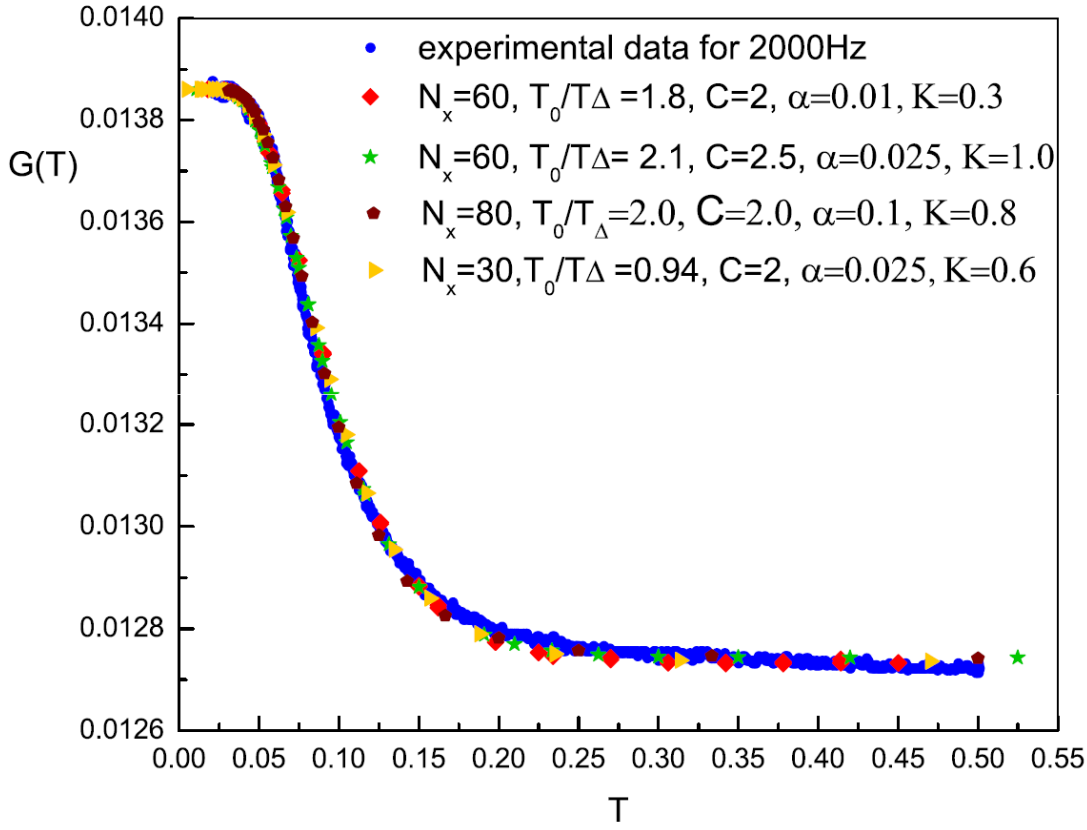

Figure 5.3: Experimental shear modulus $G(T)$ from [20] for 2000 Hz (blue dots) and the modulus (5.33) with $\kappa(T)$ obtained by MC for four sets of parameters [62]. All five curves have been collapsed on each other by the simple rescaling of the temperature T to $T * T_0/T_\Delta$. Error bars do not exceed the dot size.

To summarize it was shown that the crossover from $T = 0$ to finite temperatures leads to *intrinsic* softening of the shear modulus, that is, even if no ^{3}He impurities were present (cf. [20]). The crossover is solely controlled by kink typical energy and their density and for dislocation sizes greater than kink size it should be size-independent.

Chapter 6

Effect of ^{3}He impurities

6.1 Impurities and dislocations: depinning scenarios

One of the most intriguing phenomena observed in solid ^{4}He is the striking similarity in temperature dependencies of NCRI fraction and shear modulus (see Section 2.1.2,[20, 28]). The shear modulus softening occurs in the same temperature range (below 200 mK) where NRCI fraction starts growing, and both phenomena share the same dependence on temperature and ^{3}He concentration. All these similar features strongly suggest the common origin of these two phenomena. It was argued [20, 28] that ^{3}He impurities play the major part in shear modulus stiffening at low T by binding to dislocations and rendering them immobile.

We are going to show that ^{3}He alone cannot explained the qualitative behavior of G softening and that the inclusion of Peierls potential is essential in understanding this phenomena.

Let's consider what is happening to the dislocation and the impurities as we change

the temperature. At $T = 0$ the dislocation is in smooth state (Section 5.2.2,[62]) pinned by ^{3}He atoms and localized in one of the Peierls valleys as in Fig.6.1a (slanting of dislocation requires energy, being possible in highly disordered samples, and is not considered here). As temperature grows there are two mechanisms of dislocation depinning. The first one includes ^{3}He atoms unbinding (or evaporating) from dislocation allowing it to move [20, 28] as in Fig.6.1b. Let's call it ^{3}He "boiling off" mechanism. The second option takes into account that the growing temperature generates thermal kinks which allows the dislocation line to detach from impurities (even if they have not been evaporated) and move into different Peierls valleys (see Fig.6.1c). This model is called "creeping away" mechanism. These two options can of course work together.

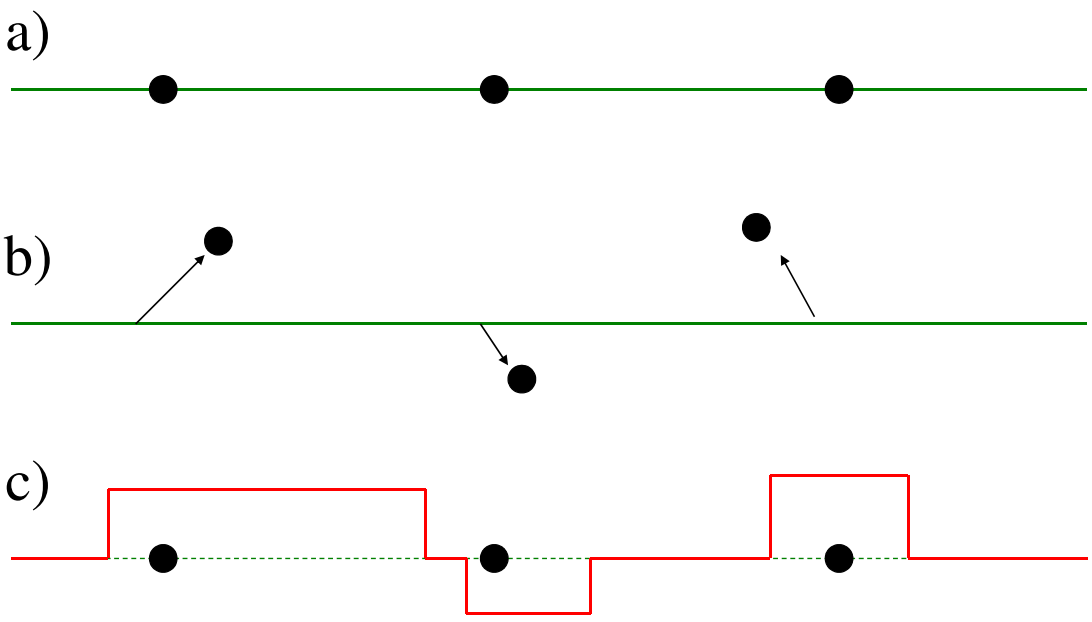

Figure 6.1: a) Smooth dislocation at $T = 0$; b) 1^{st} option: ^{3}He boiling off (evaporation model); c) 2^{nd} option: "Creeping away" from Peierls potential and ^{3}He atoms due to thermal kinks

6.2 Gradient expansion: impurities inclusion

Duality approach which was discussed above is a very useful tool in obtaining the information about SG-like systems. A new approach is needed, however, if we try to include the impurities into consideration, represent their pinning potential, e.g., by Gaussian, and try to add terms $V = V_0 N(x) \exp\left(-\left(y(x,t)/y_0\right)^2\right)$ into the Hamiltonian, where y – dislocation displacement from the impurity, y_0 – typical scale of the potential and $N(x) = 0,1$ gives the impurity density. The alternative technique in this case is called the "gradient expansion" and is based on Taylor expansion of the exponent, containing gradient term, in the partition function. The basic calculations, without inclusion of the impurities, are presented in Appendix B.

Lets add the impurities pinning potential and write down the Hamiltonian in the following form

$$H = \sum_i \left(2y_i^2 - 2\alpha\cos(By_i) - N_i V_0 \exp\left(-\frac{K}{2}y_i^2\right)\right) - \sum_{\langle ij\rangle'} y_i y_j, \tag{6.1}$$

so that

$$H = \sum_i H_i - \sum_{\langle ij\rangle'} y_i y_j. \tag{6.2}$$

Here $N_i = 0,1$ stands for onsite ^{3}He impurities, considered as Boltzmann particles so that $\frac{\partial}{\partial\tau}N(x,\tau) = 0$. The partition function is

$$\begin{aligned} Z = \int Dy \exp(-H) = \prod_i \int dy_i \exp\left(-H_i\right) \prod_{\langle ij\rangle'} \sum_{\{N_{ij}\}} \frac{\left(y_i y_j\right)^{N_{ij}}}{N_{ij}!} = \\ = \sum_{\{N_{ij}\}} \left(\prod_i C(i)\right) \prod_{\langle ij\rangle'} \frac{1}{N_{ij}!}. \end{aligned} \tag{6.3}$$

The main part of the calculations (see Appendix B) holds true except we get a modified $C(i)$ for the sites with impurities present:

$$\begin{aligned} C(i) &= \sum_{n=0}^{\infty} \frac{V_0^{n_c}}{n!} \int dy_i \exp\left(-y_i^2\left(2+\frac{K}{2}n\right)+2\alpha\cos(By_i)\right) y_i^{k(i)} = \\ &= \sum_{n=0}^{\infty} \frac{V_0^{n}}{n!} \sum_{m} \int dy_i y_i^{k(i)} e^{-y_i^2\left(2+\frac{K}{2}n\right)-\alpha(By_i-2\pi m)^2}. \end{aligned} \tag{6.4}$$

After integration, one obtains

$$C(i) = \sum_{p=0}^{p'} \sum_{n,m} \left[\begin{array}{l} \dfrac{V_0^{n_c}}{n!} e^{-4\pi^2 m^2 \alpha + \frac{(2\alpha B\pi m)^2}{2+\frac{K}{2}n+\alpha B^2}} \dfrac{(2p')!\,(2p-1)!!}{(2p)!(2p'-2p)!} \times \\ \times \left(\dfrac{2\alpha B\pi m}{2+\frac{K}{2}n+\alpha B^2}\right)^{2(p'-p)} \dfrac{\sqrt{\pi}}{2^p\left(2+\frac{K}{2}n+\alpha B^2\right)^{p+1/2}} \end{array} \right]. \tag{6.5}$$

The ratio of the expressions C necessary for MC updates can be simplified to in case of no Peierls potential $\alpha = 0$

$$\frac{C(k(s)+2)}{C(k(s))} = \frac{k(s)+1}{4} \frac{1+\sum_n^{\infty} \frac{V_0^n}{n!} \frac{1}{(1+Kn/4)^{(k(s)+3)/2}}}{1+\sum_n^{\infty} \frac{V_0^n}{n!} \frac{1}{(1+Kn/4)^{(k(s)+1)/2}}}, \tag{6.6}$$

where the summations should be performed only if a site with ^{3}He particle on it is being updated. For the open worm wondering around the system the correlator is

$$\langle y_n y_m \rangle = \frac{1}{Z} \left[\sum_{\{N_{ij}\}} \left(C(n+1)C(m+1) \prod_{i \neq n,m} C(i) \right) \prod_{<ij>'} \frac{1}{N_{ij}!} \right]. \tag{6.7}$$

When the worm closes it changes to

$$\langle y_s y_s \rangle = \frac{\sum_{\{N_{ij}\}} \Big(C(s+2) \prod_{i \neq s} C(i) \Big) \prod_{<ij>'} \frac{1}{N_{ij}!}}{\sum_{\{N_{ij}\}} \big(\prod_i C(i) \big) \prod_{<ij>'} \frac{1}{N_{ij}!}} = \\ = \frac{1 \times \sum_{\{N_{ij}\}} \Big(\prod_{i \neq s} C(i) \Big) \prod_{<ij>'} \frac{1}{N_{ij}!}}{\frac{C(s)}{C(s+2)} \sum_{\{N_{ij}\}} \Big(\prod_{i \neq s} C(i) \Big) \prod_{<ij>'} \frac{1}{N_{ij}!}}, \tag{6.8}$$

which gives the estimators: 1 for correlator and $C(s)/C(s+2)$ for the partition function.

In case $\alpha = 0$ the acceptance ratio for a "move" procedure from site s to s' is $R = \frac{k(s')+1}{k(s)-1}$. To "shift" from s to s' while creating the bond $R = (k(s')+1)/N_{ss',new}$ and while destroying $R = N_{ss',old}/(k(s)-1)$.

6.3 Gapped string effective description

MC simulations were performed of the full nonlinear action (6.1). It turned out that the obtained results could be perfectly fit by an effective Gaussian

$$S_f = \int_{-L/2}^{L/2} dx \left(\frac{\nu^2}{2} \left(\frac{\partial y}{\partial x} \right)^2 + \frac{\Delta^2}{2} y^2 - fy \right). \tag{6.9}$$

This is the action at zero Matsubara frequency of a gapped string with some effective parameters ν and Δ. These parameters can be obtained from the simulations of a full (microscopic) action (6.1). Gaussian models allow to obtain the solution right away.

The average for the action (6.9)

$$< y(x) >_f = \frac{\int \mathbf{D} y e^{-S_f} y}{\int \mathbf{D} y e^{-S_f}} \tag{6.10}$$

should be linearly proportional to the force f in the limit of small f, so we expand in Taylor series and leave only linear in f terms

$$< y(x) >_f = \frac{\int \mathbf{D} y e^{-S_0} \int dx' y(x') y(x) f}{\int \mathbf{D} y e^{-S_0}}. \tag{6.11}$$

Therefore the average is determined by the correlation function with no external force present

$$< y(x) >_f = f \int dx' < y(x') y(x) > . \tag{6.12}$$

Now we know from minimizing the action that

$$y(x) = \frac{f}{\Delta^2} \left(1 - \frac{\cosh(\kappa x)}{\cosh(\kappa L/2)} \right), \quad -L/2 < x < L/2, \quad \kappa \equiv \frac{\Delta}{\nu}. \tag{6.13}$$

So we have

$$\int dx' < y(x')y(x) >= \frac{1}{\Delta^2}\left(1 - \frac{\cosh(\kappa x)}{\cosh(\kappa L/2)}\right) \tag{6.14}$$

and we approximate the correlator from the full model by the above Gaussian ansatz:

$$G_{\text{corr}}(x) = \int dx' < y(x)y(x') > /L^2 = \frac{1}{\Delta^2 L^2}\left(1 - \frac{\cosh(\kappa x)}{\cosh(\kappa L/2)}\right). \tag{6.15}$$

The example of the correlators obtained from MC simulations of the full nonlinear model is presented on the Fig. 6.2.

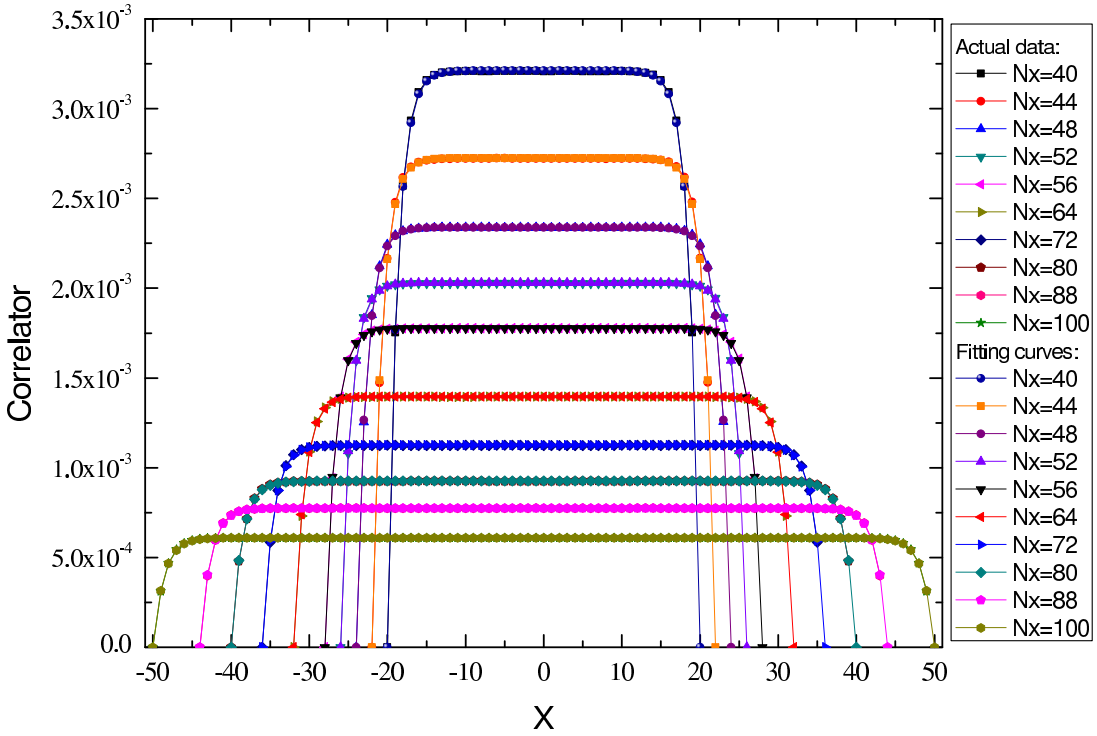

Figure 6.2: Correlators obtain from MC of full nonlinear model (6.1). Parameters: $N_y = 40$, $K = 0.1$, $V_0 = 1$, $N_{He3} = 10$, $\alpha = 0.3$. Different curves correspond to different dislocation sizes N_x. Each curve is fitted by (6.15) with b and x being fitting parameters.

The data was obtained for different dislocation length N_x with fixed amount of impurities $N_{He3} = 10$ (resulting in different densities) for $N_y = 40$, $K = 0.1$, $V_0 = 1$,

$\alpha = 0.3$. Each correlator is fitted by (6.15). The considerable strength of pinning potential used in this case strongly suppresses the free-string parabolic form and creates a plateau on top of each curve.

Using the fit, the gap Δ values were obtained and Fig.6.3 illustrates how Δ changes with ^{3}He density. The parameters of the system are $K = 0.1$, $V_0 = 1$, the different ones include change in α, amount of impurities N_{He3} and the method of density change N_{He3}/N_x: for the first three curves N_{He3} = const with changing N_x, for curves 4 and 5 N_x= const with scan performed over N_{He3}.

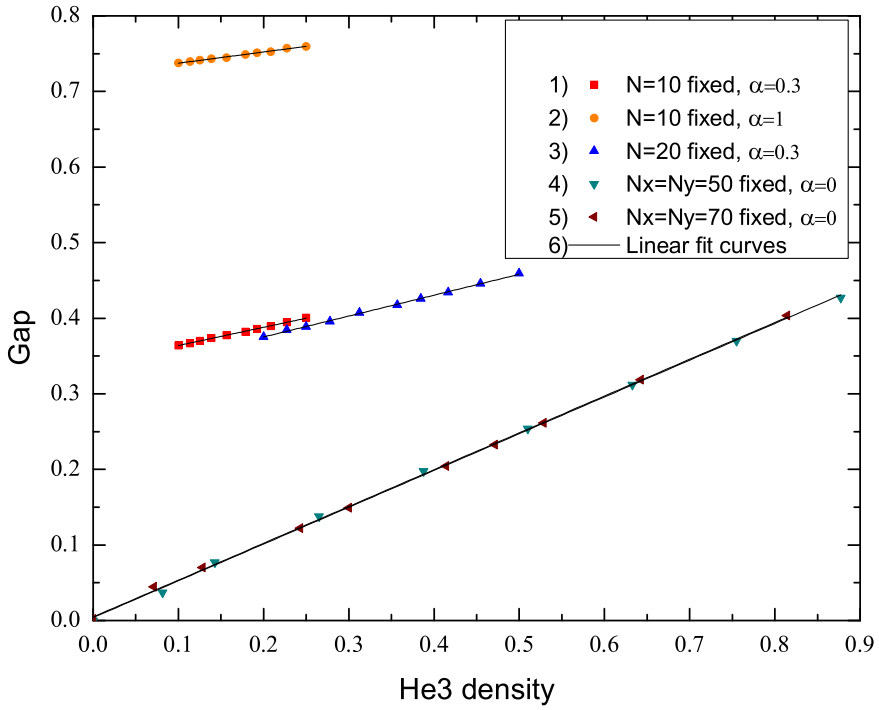

Figure 6.3: Gap Δ values obtained from fit (6.15). Common parameters: $K = 0.1$, $V_0 = 1$. Different parameters: 1,2) N_{He3}= 10 = const, scan over N_x for $\alpha = 0.3$ (see Fig. 6.2) and $\alpha = 1$; 3) similar to above with $N_{He3} = 20$ and $\alpha = 0.3$; 4,5) $N_x = N_y = 70$, $\alpha = 0$, scan over N_{He3}: 6) Black lines represent linear fit.

Comparison of curves 1 and 2 shows that the increase in Peierls potential strength

α effectively increases gap, which was to be expected. Curves 1 and 3 demonstrate that the particular way of changing density changes the results but slightly. Curves 4 and 5 extrapolate to 0 which is to be expected since for $\alpha = 0$ and $N_{He3} = 0$ the string is free and gapless.

The most important feature of all the curves is that gap Δ is *linear* in density of impurities, regardless of the parameters of the system. We will use this fact extensively later while fitting shear modulus experimental data.

As was shown in Section 3.2.1 we can relate the correlator (6.15) to the shear modulus as

$$\frac{1}{G(T)} = \frac{1}{G_0}\left[1 + \lambda \int_{-L/2}^{L/2} G_{\rm corr}(x)dx\right], \tag{6.16}$$

where $\lambda \approx 0.1 - 0.3$ is the absolute value of the shear modulus stiffening. Thus we have (reminding the definition of the dislocation density as $x_d = 1/L^2$)

$$\frac{1}{G(T)} = \frac{1}{G_0}\left[1 + \frac{\lambda\nu^2 x_d}{\Delta^2}\left(1 - \frac{\tanh\frac{\Delta}{2\nu\sqrt{x_d}}}{\frac{\Delta}{2\nu\sqrt{x_d}}}\right)\right]. \tag{6.17}$$

Since we know that $\Delta \sim N_{He3}$ the next step is to calculate how the density of bound to the dislocations impurities changes with temperature.

6.4 "Boiling off" model

Let's consider a simple thermodynamic model for ^{3}He atoms and write the Hamiltonian of the system in the form

$$H = \sum_i (E_i - \mu)\, n_i. \tag{6.18}$$

where $n_i = 0, 1$ reflects the presence of ^{3}He on any site – either on dislocation or in bulk, $i = 1, 2, ..., N_b + N_d$, E_i is the energy of ^{3}He atom on site i. $E_i = E_a$ if ^{3}He is in the bulk and 0 if on the dislocation. N_b and N_d are the number of available "places" for ^{3}He in the bulk and on the dislocations respectively and μ is the chemical potential. The restriction imposed in the system is

$$\sum_i < n_i >= N_3, \tag{6.19}$$

where N_3 is the total amount of ^{3}He atoms. The partition function is therefore

$$\begin{aligned} Z = \sum_{n_1=0}^{1} \sum_{n_2=0}^{1} ... \sum_{n_{N_b+N_d}=0}^{1} \exp\left(-\sum_i \beta n_i(E_i - \mu)\right) = \\ = \sum_{n_1=0}^{1} \exp\left(-\beta n_1(E_1 - \mu)\right) \sum_{n_2=0}^{1} \exp\left(-\beta n_2(E_2 - \mu)\right)... \\ \times \sum_{n_{N_b+N_d}=0}^{1} \exp\left(-\beta n_{N_b+N_d}(E_{N_b+N_d} - \mu)\right) = \\ = \prod_{i=i}^{N_b+N_d} \left[1 + \exp\left(-\beta(E_i - \mu)\right)\right] = \left(1 + \exp\left(\beta(\mu - E_a)\right)\right)^{N_b} \left(1 + \exp\left(\beta\mu\right)\right)^{N_d}. \end{aligned} \tag{6.20}$$

The mean occupation number on a site s is given by

$$< n_s >= -\frac{1}{\beta}\frac{\partial \ln Z}{\partial E_s} = -\frac{1}{\beta}\frac{\partial}{\partial E_s}\left[ln(1 + \exp\left(-\beta(E_s - \mu)\right))\right] = \frac{1}{1 + \exp\left(\beta(E_s - \mu)\right)}. \tag{6.21}$$

The condition (6.19) becomes

$$\sum_{i=bulk} \frac{1}{1 + \exp\left(\beta(E_a - \mu)\right)} + \sum_{i=dislocation} \frac{1}{1 + \exp\left(-\beta\mu\right)} = N_3 \tag{6.22}$$

or

$$\frac{N_b}{1+\exp\left(\beta(E_0-\mu)\right)}+\frac{N_d}{1+\exp\left(-\beta\mu\right)}=N_3, \tag{6.23}$$

$$\frac{1}{1+\exp\left(\beta(E_a-\mu)\right)}+\frac{N_d/N_b}{1+\exp\left(-\beta\mu\right)}=\frac{N_3}{N_b}. \tag{6.24}$$

Let's introduce dislocation density $x_d = N_d/N_b$ and impurity density $x_3 = N_3/N_b$. Physically, $x_d \ll 1$ and $x_3 \ll 1$. We will be using the range $x_3 \leq x_d$. In the opposite limit we assume excess of ^{3}He stays in the bulk and reduce slightly $N_b \to N_b - (N_3 - N_d)$ at $T = 0$. So, the solution with + sign becomes

$$\mu = T\ln\lambda,$$

$$\lambda = \frac{2x_3}{e^{-\frac{E_a}{T}} - (1+e^{-\frac{E_a}{T}})x_3 + x_d + \sqrt{\left(e^{-\frac{E_a}{T}} - (1+e^{-\frac{E_a}{T}})x_3 + x_d\right)^2 + 4x_3(1+x_d-x_3)e^{-\frac{E_a}{T}}}}. \tag{6.25}$$

We use this solution to find ^{3}He fraction on the dislocation $X(T)$

$$\begin{aligned} X(T) &= \frac{1}{1+e^{-\mu/T}} \\ &= \frac{2x_3}{(1-x_3)e^{-\frac{E_a}{T}} + x_3 + x_d + \sqrt{\left[x_d + x_3 + (1-x_3)e^{-\frac{E_a}{T}}\right]^2 - 4x_d x_3(1-e^{-\frac{E_a}{T}})}}. \end{aligned} \tag{6.26}$$

Let's divide by x_d both numerator and denominator and introduce a variable

$\xi = x_3/x_d = N_3/N_d$:

$$X(T) = \frac{2\xi}{(x_d^{-1} - \xi)e^{-\frac{E_a}{T}} + 1 + \xi + \sqrt{\left[1 + \xi + (x_d^{-1} - \xi)e^{-\frac{E_a}{T}}\right]^2 - 4\xi(1 - e^{-\frac{E_a}{T}})}}. \tag{6.27}$$

The same result could be obtained from writing down the energy of a simple model "dislocation-impurity" as

$$F = E_a n_b + T\left(n_b \ln\frac{n_b}{eN_b} + (N_b - n_b)\ln\frac{N_b - n_b}{eN_b} + n_d \ln\frac{n_d}{eN_d} + (N_d - n_d)\ln\frac{N_d - n_d}{eN_d}\right), \tag{6.28}$$

where $N_3 = n_b + n_d$ reflects the fact that ^{3}He atoms can be in bulk or can "sit" on dislocations. In this notation $X(T) = n_d/N_d$. Minimizing the energy with respect to n_b we arrive at the same expression for $X(T)$ in the limit $x_d = N_d/N_b \ll 1$ as we already have from (6.27)

Using the fact that $x_d \ll 1$ we can simplify (6.27) even further:

$$X(T) = \frac{2\xi}{\frac{e^{-\beta E_a}}{x_d} + 1 + \xi + \sqrt{\left[1 + \xi + \frac{e^{-\beta E_a}}{x_d}\right]^2 - 4\xi(1 - e^{-\beta E_a})}}. \tag{6.29}$$

Eq. (6.29) will be later used for to fit actual experimental data.

6.5 Fit by pure "boiling-off" model

Here we presume that no Peierls potential is present and we will try to fit experimental data by pure "boiling-off" mechanism. As it was shown on Fig.6.3 the energy gap of a string in our model is linearly proportional to the density of impurities "sitting" on

it, that is $\Delta = gX(T)$ and we can rewrite (6.17) as

$$\frac{1}{G(T)} = \frac{1}{G_0} + \frac{\gamma}{g^2X^2(T)}\left(1 - \frac{\tanh\frac{gX(T))}{2\sqrt{x_d}}}{\frac{gX(T)}{2\sqrt{x_d}}}\right), \tag{6.30}$$

where γ and g are some adjustable parameters and dislocation length $L = 1/\sqrt{x_d}$. In case of zero Peierls potential $\alpha = 0$ the concentration $X(T)$ can be calculated from (6.29). The fitting results are presented on Fig.6.4 where the actual experimental data are the same as used in Section 5.2.3([20]).

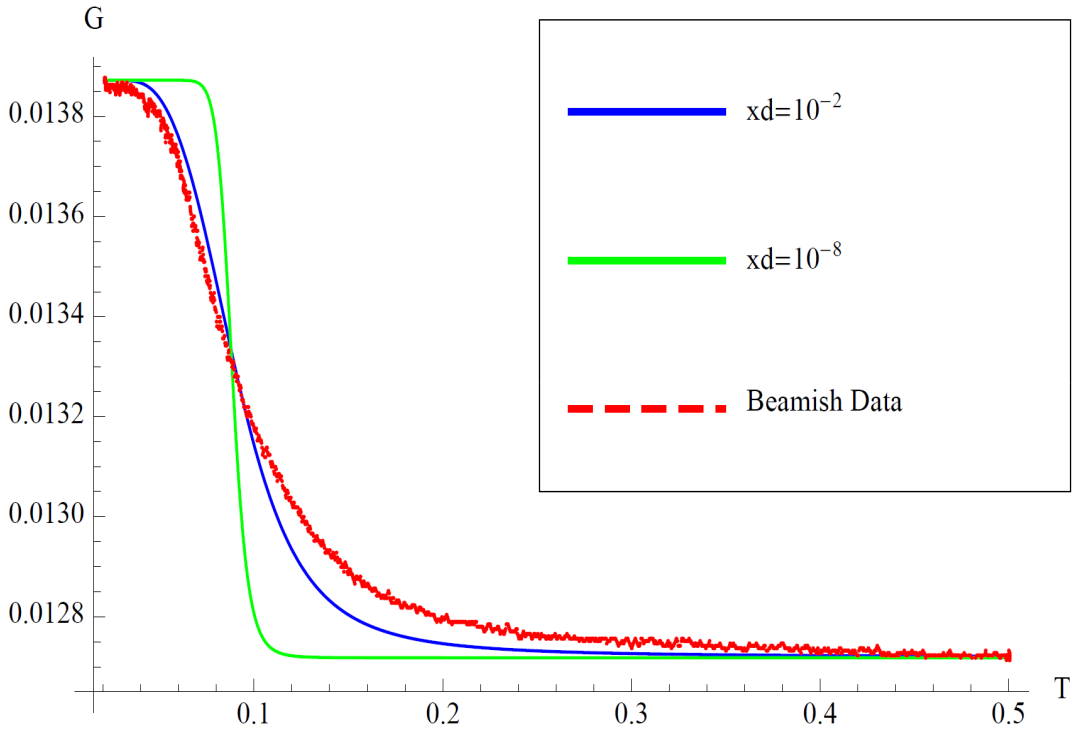

Figure 6.4: Fit of experimental data [20] by pure "boiling-off" model. The theoretical curve for a physical amount of dislocation density $x_d = 10^{-8}$ (green line) is quite sharp and does not follow the experimental curve. Much closer fit can be achieved (blue line), but it required enormously high amount of dislocations $x_d = 10^{-2}$. The stiffening region is $\delta T \approx T_{jump} \approx E_a/|\ln(x_d)|$.

Parameters γ and G_0 are chosen to fit the data points for $T \to 0K$ and $T = 0.5K$ and the used parameters are $\xi = 0.7$, $E_a = 0.5$, $x_d = 10^{-9}, ..., 10^{-1}$. Two curves

are shown for comparison: one obtained for a physical value of dislocation density $x_d = 10^{-8}$ and the one for extremely high concentration $x_d = 10^{-2}$. The first one exhibits quite sharp G stiffening and does not fit the experimental data, the other one is much closer to the actual curve but requires an enormously higher number of dislocations. Therefore we conclude that the pure "boiling-off" model alone can not explain the shear modulus softening in solid ^{4}He since requires an unphysical amount of dislocations to do so.

The temperature region of stiffening (jump) is proportional to the temperature of the jump $\delta T \approx T_{jump} \approx E_a/|\ln(x_d)|$. The temperature of full dislocation decoupling without Peierls potential is $T_d \approx E_a/|\ln\left(\frac{X_3}{\sqrt{x_d}}\right)|$, where X_3 is the bulk fraction of ^{3}He. Thus the jump-like feature will be observed for $X_3/\sqrt{x_d} \ll 1$ and a good fit will be achieved for $X_3/\sqrt{x_d} \geq 1$, which for physical dislocation densities $x_d > 10^{-8}$ means rather high impurity concentrations $X_3 > 100$ p.p.m. It is also interesting to notice that the temperature of a stiffening T_{jump} allows to obtain an estimation of the dislocation density as

$$x_d \approx e^{-\frac{E_a}{T_{jump}}}. \tag{6.31}$$

In Section 5.2.3 it has been shown that the experimental data for clean samples can well be described by the dislocation model with Peierls potential only (see Fig. 5.3). Here we recalculated the data by using gradient-expansion technique (See Section 6.2) and also collected the data for a set of finite linear densities of ^{3}He [61]. Such simulations mimic a dislocation behavior in pure "creeping-away" mechanism. The results are presented in Fig.6.5 and Fig.6.6 where n stands for the impurity density.

For larger n the softening of shear modulus $G(T)$ shifts to higher T which can be seen in Fig.6.5. The curves turned out to be almost self-similar so we could collapse them to a single master curve simply by rescaling temperature T as $T \to TT_\Delta$

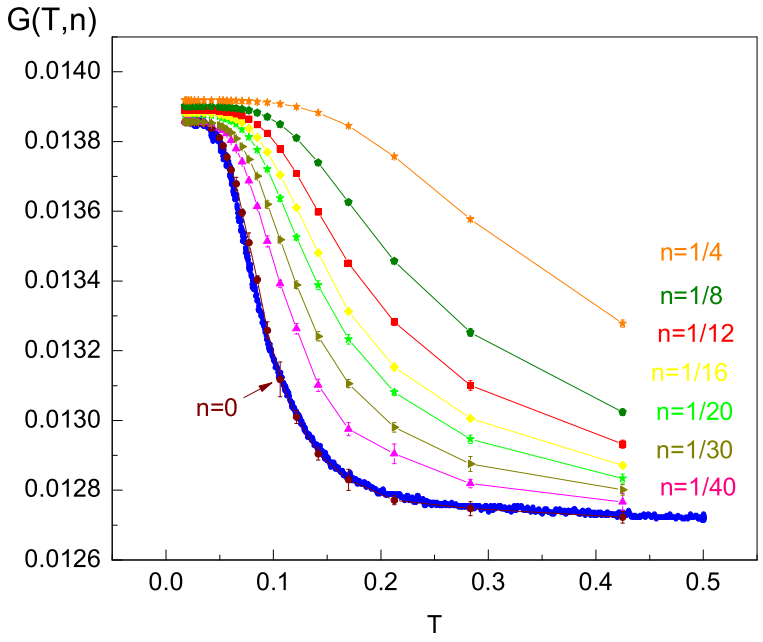

Figure 6.5: Shear modulus G from [20, 28] for 1 ppb of ^{3}He at f = 2000Hz (blue dots) and the ones obtained by MC simulations of the model (1,3) for the "creeping away" mechanism for various (linear) concentrations n of ^{3}He impurities. The curves represent shear modulus $G(T)$ for different n. The simulations parameters: $\alpha = 0.005$, $K = 0.1$, $V_0 = 0.3$.

(see Fig.6.6). In simulations the impurity density n remained fixed but thermal kinks allowed dislocation to "break free" from impurities and reach its high-T value. Parameter T_Δ can be used to obtain a typical energy required to create kink-antikink pair Δ: $\Delta = 1/T_\Delta$.

We should mention that MC simulations with fixed impurity density values fit the experimental results well. But if one tries to allow boiling-off of impurities the obtained $G(T)$ curves will fail to fit the experimental data [61]. It appears that ^{3}He remains bound to dislocations even at large temperatures due to very long equilibration times. It was suggested that such long equilibration time is a result of a very narrow band of ^{3}He impuritons [61].

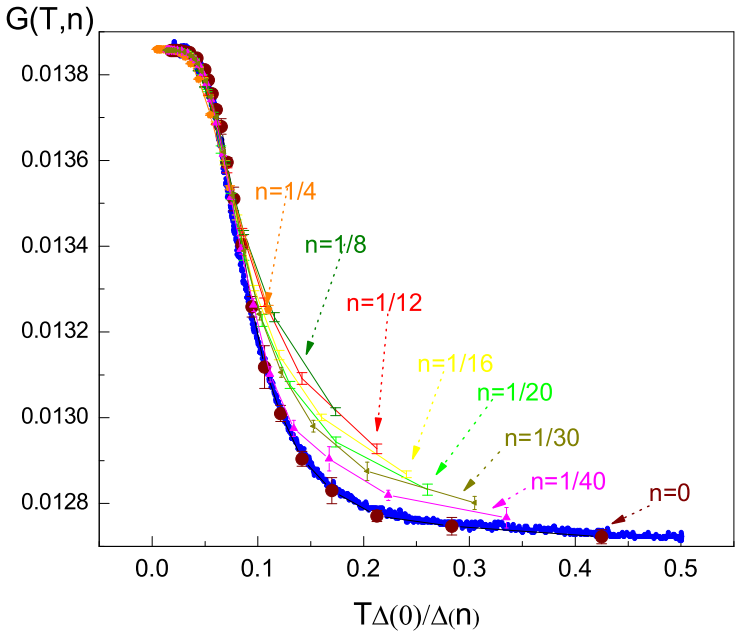

Figure 6.6: The family of the curves from Fig.6.5 has been collapsed to a single master curve by rescaling the temperature T and slightly adjusting lower-T value. The simulations parameters: $\alpha = 0.005$, $K = 0.1$, $V_0 = 0.3$.

To summarize, we showed the traditionally accepted "boiling off" model cannot explain the experimental data on shear modulus $G(T)$ softening. It is demonstrated that "creeping away" mechanism is essential in understanding the phenomenon. In other words, quantum and thermal fluctuations of dislocation shape lead to the decoupling of the gliding dislocations from the Peierls and ^{3}He pinning potentials. Such decoupling happens at temperatures determined by the energy of the kink-antikink pair Δ. In its turn such energy depends on the strength of the both potentials and ^{3}He concentration along the dislocation line.

Chapter 7

Superclimbing dislocations

7.1 The idea of superclimb

In metals at low temperatures diffusion is suppressed and the motion of dislocation is mostly provided by glide. At higher temperatures, however, edge dislocation can perform another type of motion: climb. In analogy with glide, where motion of dislocation results from the dynamics of kink-antikink pairs, climb is performed by the creation of jog-antijog pairs [44, 45]. These pairs allow to build the extra plane of atoms in the crystal, resulting, therefore, in a nonconservative type of motion. The jogs are characterized by Burger's vector (one lattice spacing) and a typical energy of $E_{jog} \approx$1 eV. At high temperatures process is facilitated by so-called "pipe diffusion" when thermally actived vacancies moving along the dislocation, as well as to and from it, help to create jogs. This process is well-known in metals and ionic crystals at $T \approx 600K - 1000K$ [47]. It was suggested that a similar phenomenon can occur in solid He at very small temperatures due to the core superfluidity of the dislocation [48]. In this case the matter delivered by superflow along the dislocation core is used to create jog-antijog pairs, and therefore, displace the edge of the dislocation. The

authors defined this macroscopic quantum phenomenon as *superclimb*. The scenario was corroborated by *ab initio* MC simulations showing that the edge dislocation with Burger's vector along C-axis in *hcp* crystal has superfluid core (see Fig.7.1) and it can climb as a response to the provided chemical potential gradient (see Fig.7.2).

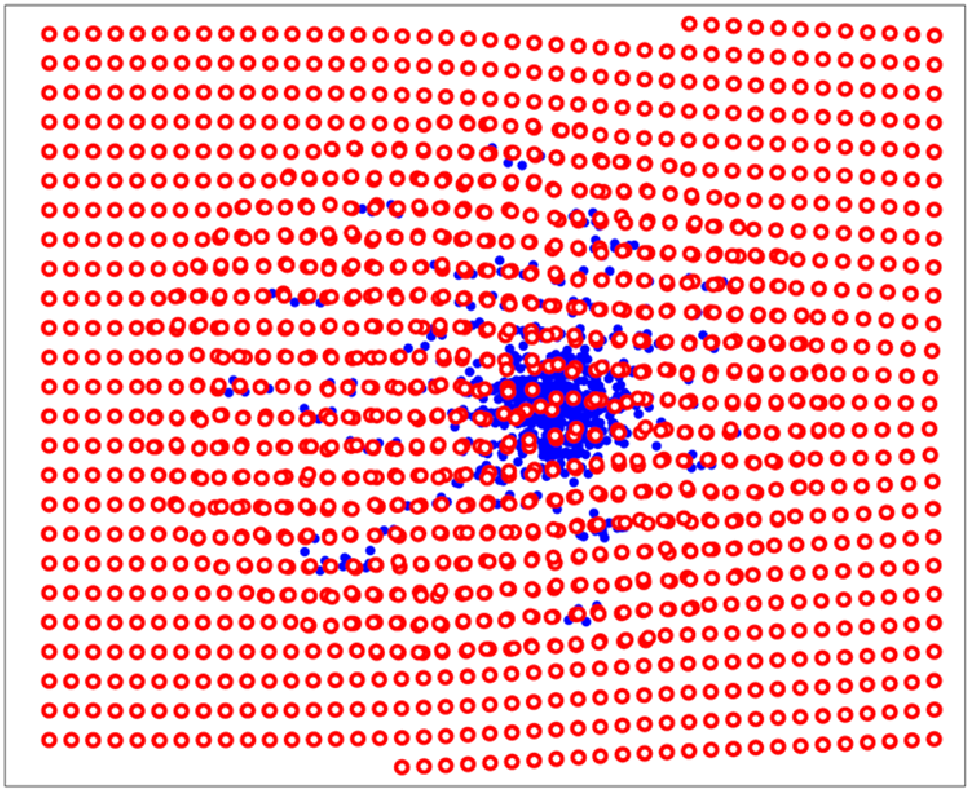

Figure 7.1: The results *ab initio* simulations from [48]. The red dots represent the actual atoms of the lattice. The blue dots display the superfluid "condensate density" map. The core of the edge dislocation is perpendicular to the picture.

The idea of superclimbing dislocations [48] was also introduced as a possible explanation for a phenomenon of so-called "giant isochoric compressibility". The non-supersolid crystal is supposed to be isochorically noncompressible $\chi \equiv (dn/d\mu)_V = 0$, which means that small changes in chemical potential μ should have no effect on the crystal density n. It follows from the fact the gapped spectrum prevents the formation of vacancies/interstitials at small temperatures, which leaves the creation/destruction

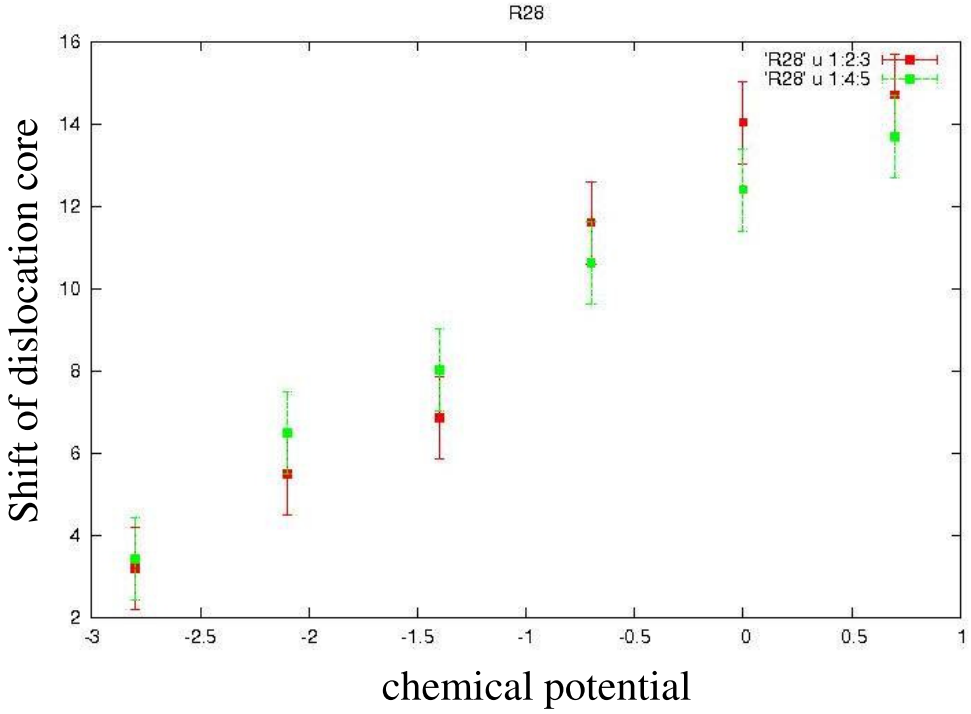

Figure 7.2: The results *ab initio* simulations from [48]. The graphs represent the dislocation core displacement as a function of the applied chemical potential. Such dependence together with the dislocation core superfluidity is an evidence of a *superclimb*. Graphs were provided as a courtesy of authors [48].

of the whole lattice layers as the only possible way to change the density. Such process requires quite long times and therefore leads to noncompressible crystals. This argument, however, does not work for supersolids since they have zero vacancy/interstitial gap. Accordingly, the isochoric compressibility should be finite – comparable to the superfluid fraction. As found in [34, 35], this fraction is no larger than 10^{-5}. Despite that, the measured compressibility was about 3 orders of magnitude higher, so that this phenomenon was called the "giant isochoric compressibility" [48]. It was suggested that the superflow along the dislocation cores allows significant and spatially uniform mass accumulation in the bulk of supersolid ^{4}He samples thus greatly in-

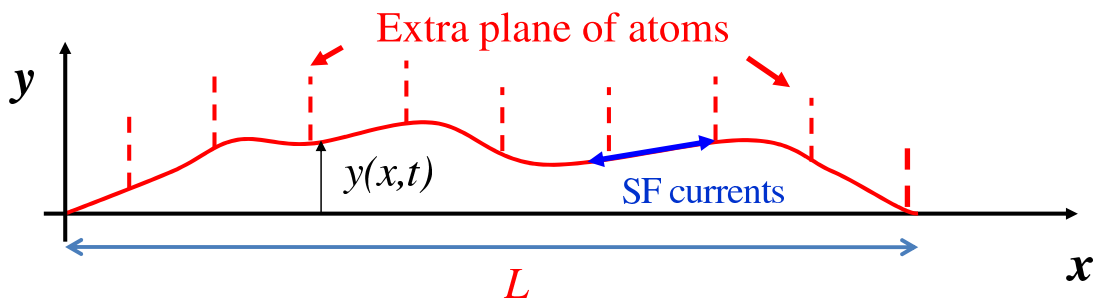

Figure 7.3: A schematic representation of a non-slanted and stronly pinned dislocation with superfluid currents along the core. A displacement $y(x,t)$ corresponds to climb - a building/reduction of the extra plane of atoms.

creasing χ. We will show later that out MC simulations of superclimbing dislocations corroborate this scenario.

7.2 The model

We model the dislocation as a quantum string of length L_x with zero boundary conditions immersed in a Peierls potential u_P and a potential provided by the external stress F. In this paper we consider just one type of motions – superclimb. The detailed description of this model and the results of *ab initio* simulations are presented in Ref. [33, 48]. A schematic representation of a dislocation in question is presented in Fig. 7.3.

The thermodynamics of a dislocation behavior is achieved by utilizing the following action

$$H = H_{SF} + H_{dis}, \tag{7.1}$$

$$H_{SF} = \int_0^\beta dt \sum \left[i(\rho + n_0)\nabla_t \phi + \frac{\rho_0}{2}(\nabla_x \phi)^2 + \frac{1}{2\rho_0}\rho'^2 \right], \tag{7.2}$$

$$H_{dis} = \int_0^\beta \sum \left[\frac{1}{2K_d} \left((\nabla_t y)^2 + V_d^2 (\nabla_x y)^2 \right) - u_P \cos(2\pi y) - Fy \right]. \quad (7.3)$$

Here the integration is done over the imaginary time $0 \leq t \leq \beta = 1/T$; the phase ϕ is defined modulo 2π. The partition function is

$$Z = \int Dy(x,t) D\rho(x,t) D\phi(x,t) \exp(-H), \quad (7.4)$$

with the integration to be performed with respect to the displacement of the core $y(x,t)$, density of the core $\rho(x,t)$ and superfluid phase $\phi(x,t)$. The boundary conditions are taken to be zero along x-axis and periodic $y(x, t+\beta) = y(x,t)$ along imaginary time. The first part of the action describes the superfluid aspect of the dislocation, with n_0 being filling factor and ρ_0 - bare superfluid stiffness. In present simulations n_0 is taken as an integer. The phase derivative is understood as a finite difference defined modulo 2π. The last term in Eq. [C.2] gives the compressibility response of the superfluid core, ρ' being a superfluid density. It also represents the essence of the superclimb effect. According to the constraint in our model $\rho(x,t) = \rho'(x,t) + y(x,t)$, the total matter delivered along the core is used to change the superfluid density ρ' and to create the displacement y. This allows the dislocation to create jogs $y \rightarrow y \pm 1, y \pm 2, ...$ at the expense of the delivered matter $\rho \rightarrow \rho \pm 1, \rho \pm 2, ...$ which in its turn is made easy due to the superfluidity of the core. Note that this jog-creation does not imply any energy cost.

The first two terms in Eq.[7.3] describe the kinetic and potential energies of the dislocation with $1/K_d$ being the effective mass density and V_d - speed of sound. The strength of Peierls potential is given by u_P. As it was discussed before [33, 62] the

parameter K_d does in fact depend on the long-range interaction between kinks (jogs) which induces the dislocation to be smooth at $T = 0$ at any arbitrary small value of such interaction, but in case of superclimb the results are not significantly affected by the strength of this interaction. This is so because the effective mass of a jog is extremely large, which insures that the dislocation must be smooth at low T even without the long-range interaction.

The very last term in Eq. [7.3] introduces the influence of the external stress applied to the dislocation string. In the experiments of Ray and Hallock [34, 35, 36, 37, 38] the injection of superfluid ^{4}He into the cell filled with solid ^{4}He led to the uniform accumulation of matter inside the bulk, therefore, the applied stress (pressure) can be considered as a way to change chemical potential. The linear force density is connected to the applied stress as $F \approx b\sigma$. The chemical potential difference [34, 35, 36, 37, 38] relates to the stress as $\delta\mu = \delta p\Omega$, where $\Omega \approx b^3$ – volume occupied by one atom. Therefore, the external stress σ, linear force density F and applied chemical potential μ are the same if we set $b = 1$. In the future all these three quantities will be considered equivalent.

It was shown [48] that for low T Peierls potential is always relevant, it creates a gap Δ for climb motion and renders the dislocation smooth. Superfluidity in this case will have a speed of sound $v_s \approx \sqrt{\rho_s u_P}$ and very small climb response $\delta y \approx \delta\mu/u_P$. For high enough temperatures Peierls potential becomes irrelevant, the dislocation becomes rough, and the small oscillations of the superfluid phase behave like [48]

$$\ddot{\phi} - \eta\partial_x^4\phi = 0, \qquad \eta \equiv \rho_s n_1 v_d^2 b^2. \tag{7.5}$$

It signifies that the spectrum of superclimbing phonons is quadratic in momentum q along the dislocation $\omega = \sqrt{\eta}q^2$ and not linear as it would be in case of sound

phonons. This regime also suggests a rather strong climbing response with a typical displacement $\delta y \approx L^2 \delta\mu$ [48]. The accumulated amount of atoms per each elementary block of the dislocation forest will be $\sim bL\delta y \approx L^3\delta\mu$ so that the density of the added atoms does not depend on L. It also leads to the important conclusion that the isochoric compressibility of the crystal should not depend on the dislocation density $\sim 1/L^2$, that is, it becomes "giant" (if compared with the case of no superclimb).

The Monte-Carlo simulations were done in terms of J-current model [62] with the use of the Worm Algorithm (WA) [57]. The details can be found in Appendix C.

7.2.1 Isochoric compressibilities

We introduce full and differential isochoric compressibilities χ_1 and χ_2:

$$\chi_1 = \frac{\Delta N}{N\Delta\mu}, \qquad \chi_2 = \frac{dN}{Nd\mu}, \tag{7.6}$$

where N is the total amount of atoms in the bulk, ΔN is the number of accumulated atoms after a chemical potential gradient is applied as in [34, 35, 36]. The latter can be related to the changes in local pressure p from its equilibrium value p_0 as $\Delta\mu = (p - p_0)\Omega$, where Ω is a volume occupied by one atom. Since $F = (p - p_0)b$ the derivative with respect to μ is identical to the derivative over F save the extra coefficient $\frac{d...}{d\mu} = (b/\Omega)\frac{d...}{dF}$.

The following two responses, full and differential, proved to be extremely useful in providing important information about dislocation properties [33]:

$$R_1 = \frac{1}{\beta L_x}\int_0^\beta \sum_x \frac{< y(x,t) >}{F} = \frac{1}{\beta L_x}\frac{d\ln Z(F)}{FdF}, \tag{7.7}$$

$$R_2 = \frac{1}{\beta L_x}\int_0^\beta dt \sum_x \frac{d < y(x,t) >}{dF} = \frac{1}{\beta L_x}\frac{d^2\ln Z(F)}{dF^2}. \tag{7.8}$$

These responses coincide at small stresses [33], but behave quite differently for large ones, giving a valuable information regarding dislocation state. Experimentally R_1 and R_2 can be measured when the total applied stress $F = F_0 + F'$ consists of a finite F_0 modified by small F'. R_2 in this case will be a linear response to F' at a finite background stress F_0.

These two responses can be utilized to obtain full G_1 and differential G_2 shear moduli (for details see [29] and Section 3.2.1)

$$\frac{1}{G_{1,2}} = \frac{1}{G_e} + n_d R_{1,2}. \tag{7.9}$$

Here G_e stands for the bare elastic share modulus so that $G_e = G_{1,2}$ for $T = 0$ [33, 62]. At high T $R_{1,2}$ responses attain their free-string value R_0 and $G_{1,2}$ achieve its high-T value G_∞.

As the atoms are accumulated on the dislocations, the displacement y of the typical dislocation forest segment L_x changes the number of atoms by $\approx 3yL_xb$ per each unit cube-block. Hence the fraction of accumulated atoms is $\approx 3ybL_x/L_x^3 \approx n_d y/b$. Therefore the accumulated atoms ΔN can be associated with the dislocation density n_d so that $\chi_{1,2} \propto n_d R_{1,2}$. The free responses become $R_0 \propto L_x^2$ implying compressibilities χ_0 of liquid ^{4}He (since $n_d \propto 1/L_x^2$). Therefore relative isochoric compressibilities $\tilde{\chi}_{1,2} = \chi_{1,2}/\chi_0$ are directly connected to the relative responses $\tilde{R}_{1,2} =$

$R_{1,2}/R_0$ as

$$\tilde{\chi}_{1,2} = \gamma \tilde{R}_{1,2}. \tag{7.10}$$

Here $\gamma \approx 0.1 - 1$ is a parameter reflecting the geometrical shape of the dislocation network. χ_1 and χ_2 obey $\chi_2 = \chi_1 + F d\chi_1/dF$, and in the linear regime $\chi_1 \approx \chi_2$. It was seen from the simulations that $\kappa \sim \chi_2/L$ when dislocation fluctuations exceed b. It should be understood, however, that κ and χ_2/L are different quantities and were obtained by different methods: χ_2 as a displacement of dislocation core, and κ as a winding number along imaginary time direction. The difference between κ and χ_2 can also be clarified from the point of view that κ and ρ_s serve as a renormalized coefficients of the effective superfluid action

$$S_\phi = \int dx \int d\tau \left[\rho_s \frac{(\partial_x \phi)^2}{2} + \kappa \frac{(\partial_t \phi)^2}{2} \right]. \tag{7.11}$$

This effective action determines the phase slip effects, with the speed of sound $V_s = \sqrt{\rho_s/\kappa}$ being a critical velocity [63].

In this work the superclimb will be considered both in the limit of small external stresses, and for higher values of applied chemical potentials which result in non-linear effects.

7.3 Small stresses: giant isochoric compressibility

In this section we consider the responses R_1 and R_2 in the limit of small applied stresses. Since the superclimbing spectrum is gapped [48] (see also Section 7.2) at low T climb is suppressed and so should compressibility. Such suppression has been seen in experiments [34]-[39]. This effect was observed in MC simulations and is demonstrated in Fig.7.4.

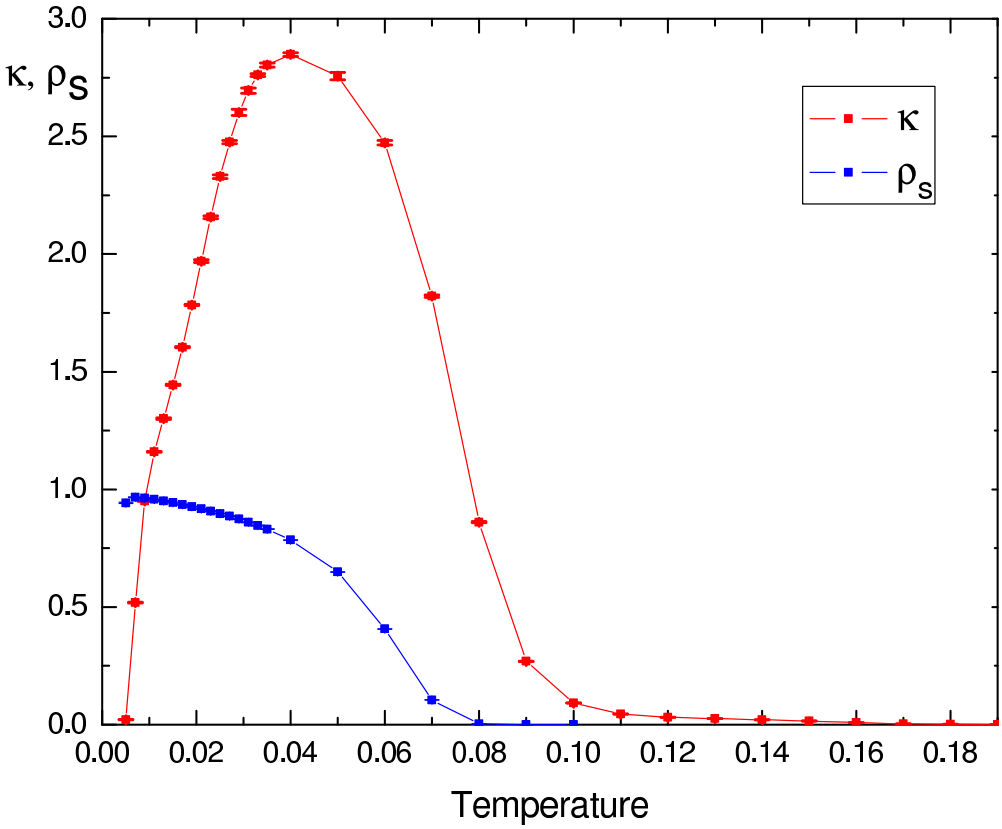

Figure 7.4: Compressibility κ and renormalized superfluid stiffness ρ_s vs T for $Nx = 30$, $Ny = 40$, $K = 1$, $T_0 = 0.2$, $u_P = 0.1$, $U_C = 1$, $F = 0.001$.

In our MC simulations superfluid compressibility was measured in terms of winding numbers of J-currents m_t along imaginary time. At low T compressibility is independent of dislocation size, and the system has strong superfluid $\rho_s \to 1$. As the temperature increases, the jogs are created thermally while the superfluidity is still present, and the superclimb allows a significant ("giant") raise of compressibility. As T grows further, superfluid vanishes, climb becomes impossible and the isochoric compressibility becomes essentially zero, as it should for a non-supersolid material. In our model we allow the bare superfluid stiffness ρ_0 in [2] to decrease with T and vanish at some characteristic temperature T_0 which is a microscopic temperature scale comparable with the bulk λ-temperature. As can be seen in Fig.7.4 and Fig.7.5 the

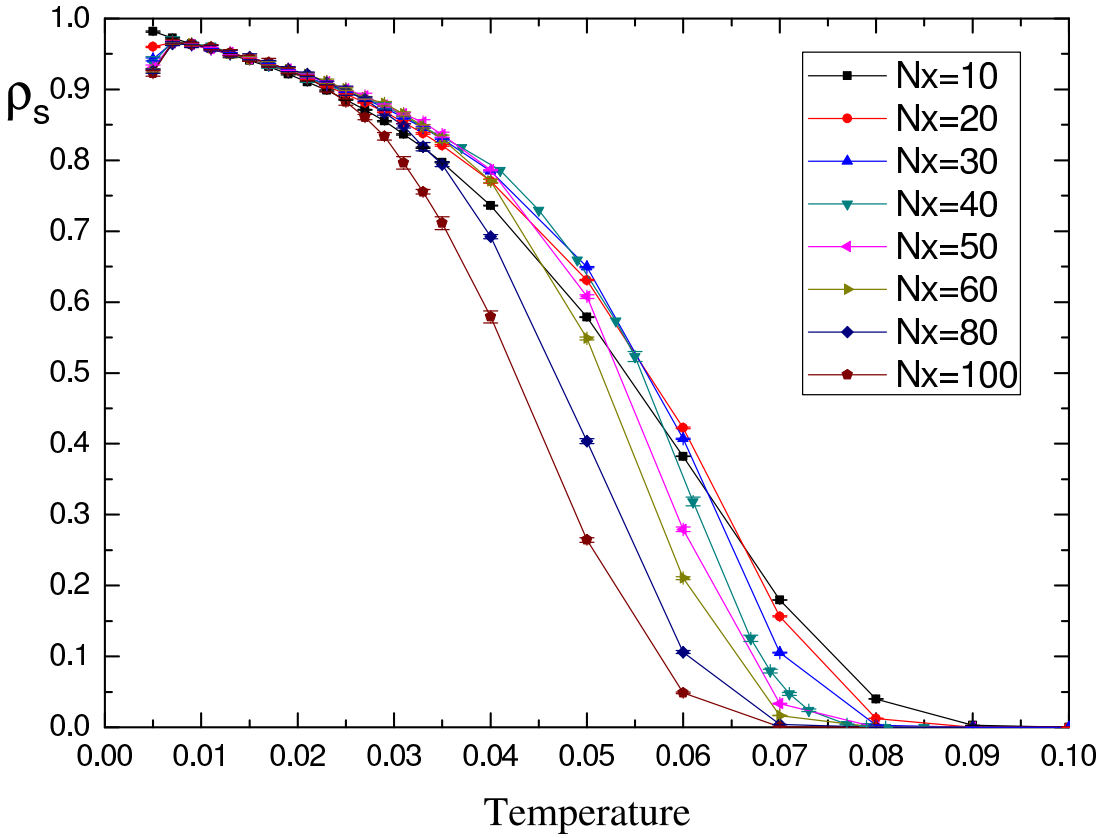

Figure 7.5: ρ_s vs T for different dislocation sizes N_x. The parameters are the same as in Fig.7.4.

suppression of both κ and ρ_s occurs at $T \approx T_0/2$ so the actual choice of $\rho_0(T)$ is not so important as long as it smoothly vanishes at $T = T_0$.

As it was predicted [48], in a superclimbing regime compressibility should scale with a dislocation size as $\kappa \approx L_x^2$. The temperature dependencies of ρ_s and κ are presented on Fig.7.5 and Fig.7.6 respectively. The sizes range from $N_x = 10$ to $N_x = 100$. $\rho_s(T)$ is only slightly affected by the dislocation size. In low-T region of $\kappa(T)$ the curves practically coincide with each other signifying a standard Luttinger-type liquid. As T grows one enters a superclimbing regime with κ_{max} strongly dependent on N_x as $\kappa_{max} \propto (N_x)^w$. At higher T curves grow closer once again and κ vanishes.

The exponent w depends on the strength of the long-range interaction U_C as it can

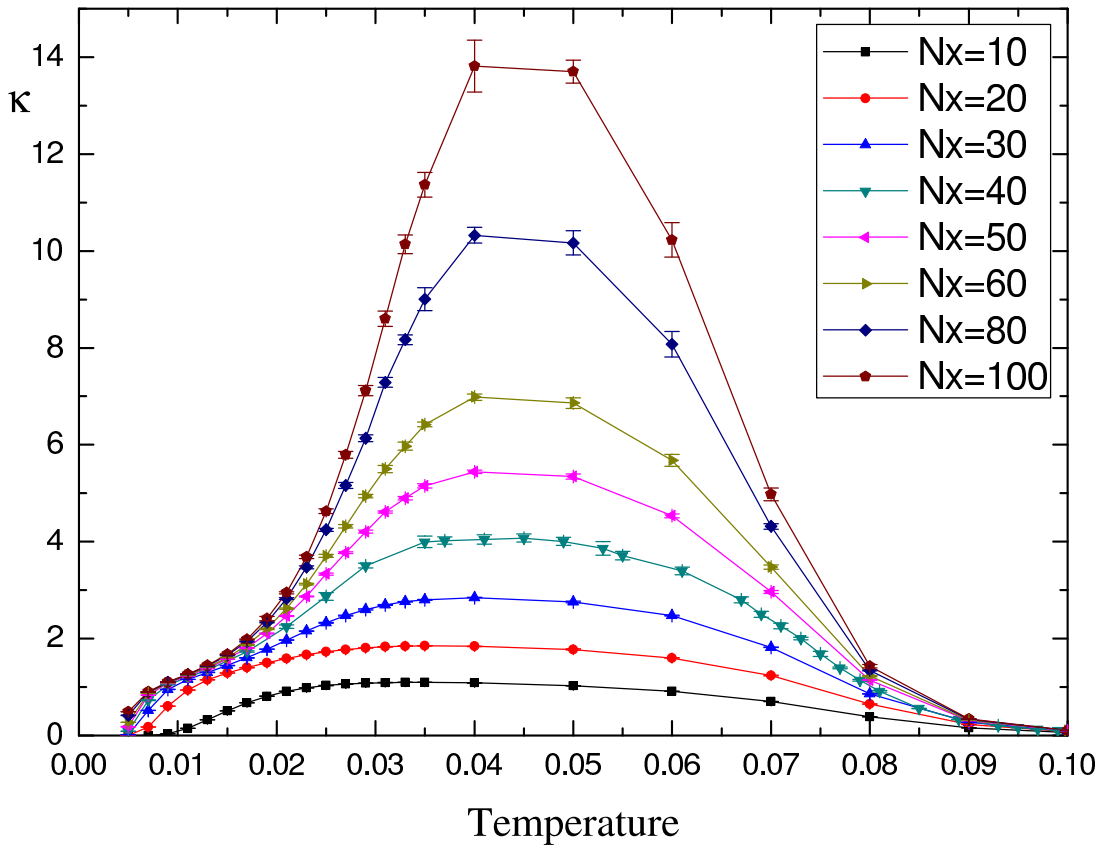

Figure 7.6: κ vs T for different dislocation sizes N_x. The parameters are the same as in Fig.7.4.

be seen in Fig. 7.7 starting from $w \approx 2$ for $U_c = 0$ and going down as U_C increases.

It was therefore shown that the isochoric compressibility is suppressed at low T according to the prediction in [48]. It was also found that the dependence of compressibility on the dislocation length is strongly dependent on long-range interactions.

7.4 Non-liner response

7.4.1 Resonant peaks

In this section we concentrate on the non-linear effects resulting from finite applied stresses [64].

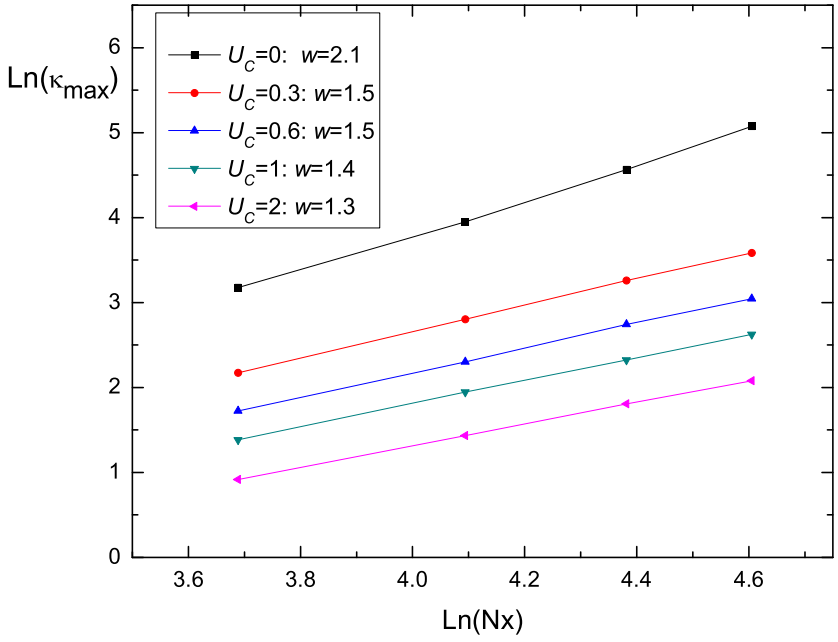

Figure 7.7: Log-dependance of κ_{max} vs N_x for different values of long-range interaction U_C: $\kappa_{max} \approx (N_x)^w$. Values of w are shown on the legend.

The work done by the external force to create a jog-antijog pair is approximately given by $E(l) \approx 2\Delta - Fl$, where Δ is the typical jog/antijog energy, and l is the distance between them. As an external applied stress reaches a certain critical threshold F_{crit} it becomes possible to create pairs as in Fig.7.8.

The external force tries to separate jog from antijog, which will reduce the pair energy, and push them to the dislocation ends . This jogs sliding increases dislocation compressibility. This effect is clearly seen on Fig.7.9 and Fig.7.10 in the ratchet-like jumps exhibited by the full response R_1 and sharp peaks observed in differential one R_2. Each next jump/peak corresponds to the creation of a new jog-antijog pair.

Coming from naive estimations the threshold value of stress should be inversely proportional to the size of the considered dislocation $F_{crit} \sim \Delta/L_x$. It is very im-

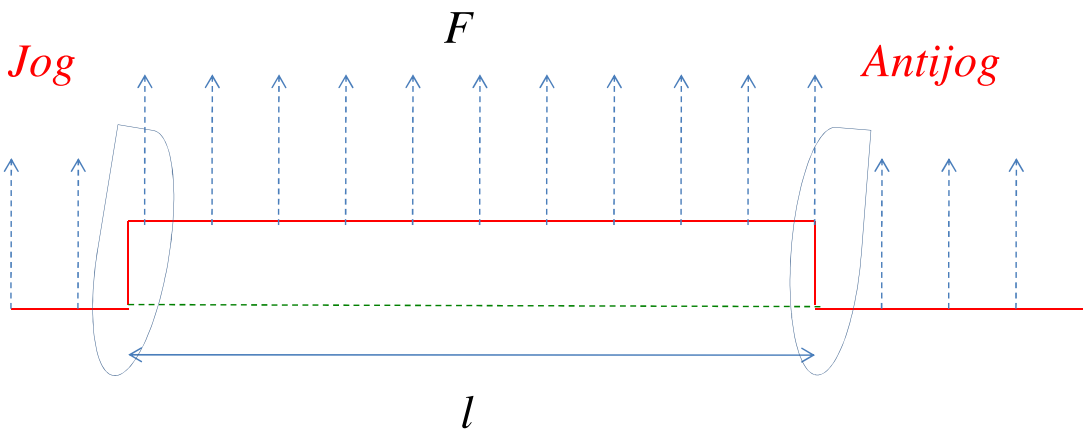

Figure 7.8: A pair of jog-antijog created on a dislocation under the applied stress F. The pair energy is $E(l) \approx 2\Delta - Fl$, Δ being a typical jog-antijog energy.

portant to understand that F_{crit} is a *macroscopically* small quantity, since for rather large dislocation sizes it will become quite small in comparison with Peierls stress.

The numerical simulations show a deviation from this rule at finite T: F_{crit} does have a power dependence on L_x but it behaves rather like $F_c \sim 1/L_x^{\gamma}$ where exponent $\gamma = 1 \div 1.7$ depends on the temperature (see Fig. 7.11). At $T \to 0$ its behavior is consistent with $\gamma = 1$, and as temperature increases $\gamma \to 1.7$. The rate of this growth is determined by the strength of Peierls potential u_P. As it will be shown below this power law is persistent up to the point where hysteresis behavior develops.

Another interesting aspect of the peaks exhibited by differential response R_2 consists in its connection to the speed of sound along the dislocation $V(T,F) = \sqrt{\frac{\rho_S(T,F)}{\kappa(T,F)}}$. Hence the peaks in κ turn into dips in the speed of sound (see Fig.7.12 and Fig.7.13). Here speed of sound $V(T,F)$ is understood as a critical SF speed along the dislocation above which the first phase slips are created thus destroying superfluidity [63].

The results of the simulations for temperature dependence $V(T)$ for different values of applied chemical potential are presented in Fig. 7.14. At small $F = 0.07$ the dip in $V(T)$ is absent, at higher F the dip develops, becomes more prominent, but

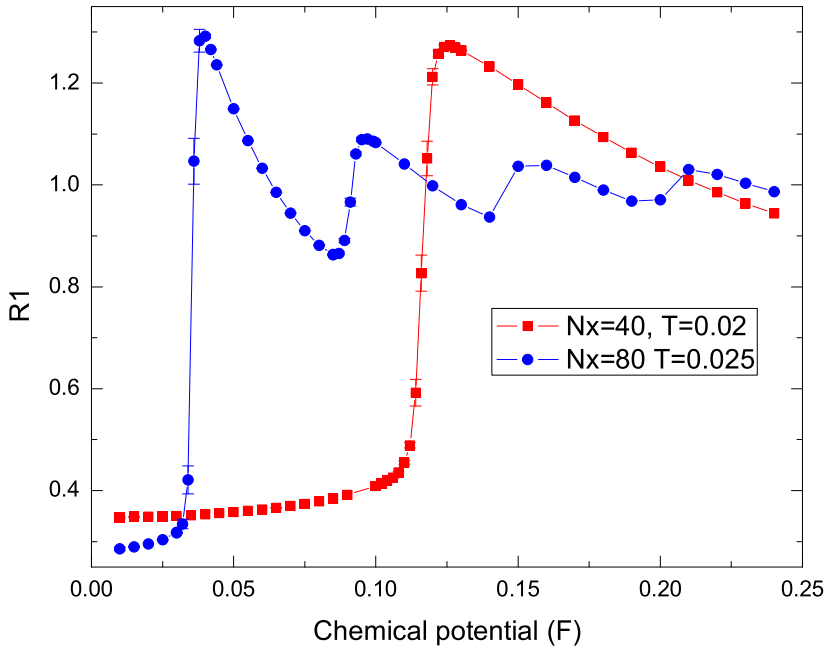

Figure 7.9: Full response R_1 vs. applied chemical potential F for two different sizes $Nx = 40$ and $Nx = 80$. Function exhibits ratchet-like jumps at certain threshold values of F.

with a further increase of F gets smaller and finally at $F = 0.1$ disappears again.

Another example of this effect is shown on Fig. 7.15. As one can see, the depth of the dip in $V_s(T, F)$ depends on how fine the applied stress is tuned to the threshold value of F for creating jog-antijog pair (the first peak values were used in this case).

The speed of sound limits the flux of atoms transported along the dislocation therefore resulting in the mass transfer decrease. We suppose that this is the effect observed in Ray and Hallock experiments [38]. Moreover we predict that at high values of applied chemical potential the effect should disappear. The same applies to low F: there should be a critical value below which the dip will not be seen. We suggest that flow rate should be studied as a function of chemical potential at fixed

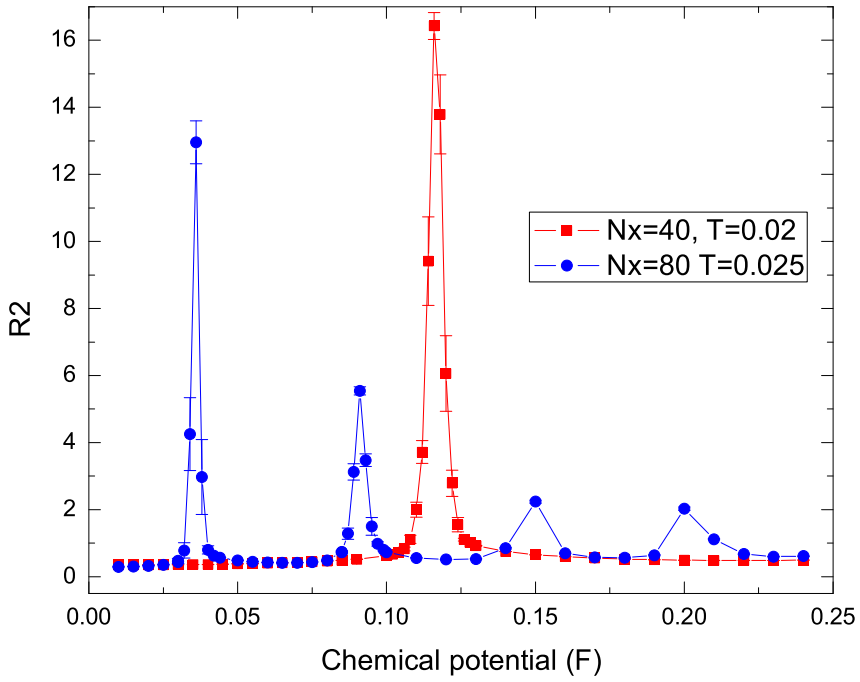

Figure 7.10: Differential response R_2 vs. applied chemical potential F for two different sizes $Nx = 40$ and $Nx = 80$. Function shows peaks at certain threshold values of F. Note that the temperatures used for two sizes are different.

temperatures in order to clarify the nature of the dip.

As we increased the dislocation size L higher than a typical tunneling length L_R through jog-anitijog barrier (compare to kink-antikink tunneling mechanism in [65]) overlap between smooth (with $R_1 \ll 1$) and rough ($R_1 = 1$) states is effectively decreased , so that it takes place only in exponentially small region δF around F_c. Therefore the peak values of $R_2(T, F_c) \approx 1/\delta F$ are diverging. An example of a strong peak dependence on the dislocation size is shown on Fig.7.16 for $T_0 = 0.2$, $u_P = 0.1$,$T = 0.004$.

The measurements of peak heights vs size for different T and u_P are presented in Fig.7.17. As one can see, the peak height increases by 2 orders of magnitude as L

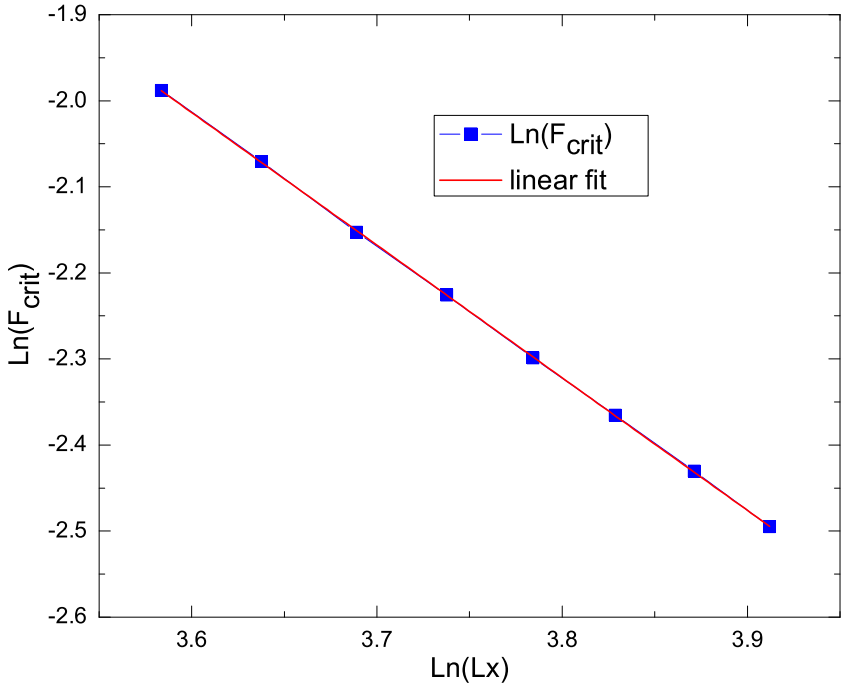

Figure 7.11: The dependence of the peak position F_c on the size of the system for a certain set of parameters at $T = 0.02$ in logarithmic scales. The linear fit gives $\gamma = 1.541 \pm 0.004$ for this particular situation: $u_P = 0.1$.

grows.

The fitting lines in Fig.7.17 were done by $\sim \exp(L/L_R)$ which gave

$$L_R^{-1} \approx L_0^{-1} \left(1 - \frac{T}{T_R}\right)^{2.3}. \tag{7.12}$$

Here L_0 signifies the tunneling length at $T = 0$. Values of T_R were found to be $T_R \approx u_P^s$ with $s = 0.5 \pm 0.1$ being set by the double energy $2\Delta \approx \sqrt{u_P}$ of a jog as the Sine-Gordon soliton. T_R determines a thermal roughtning threshold, that is, above this temperature the amount of jogs is considerable even with no stress present $F \to 0$.

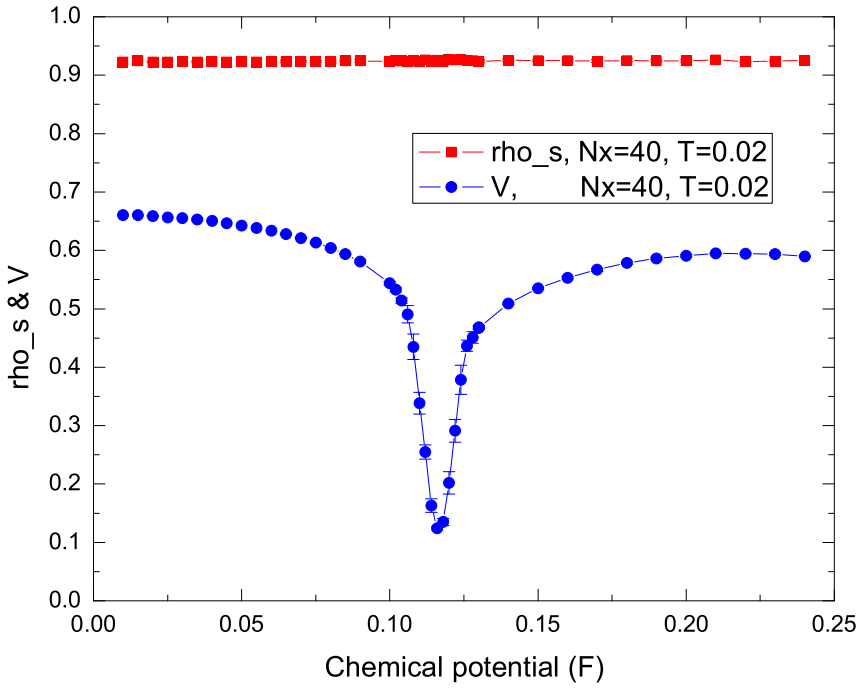

Figure 7.12: Superfluid stiffness ρ_S and speed of sound V as a function of applied chemical potential μ for size $Nx = 40$ at $T = 0.02$.

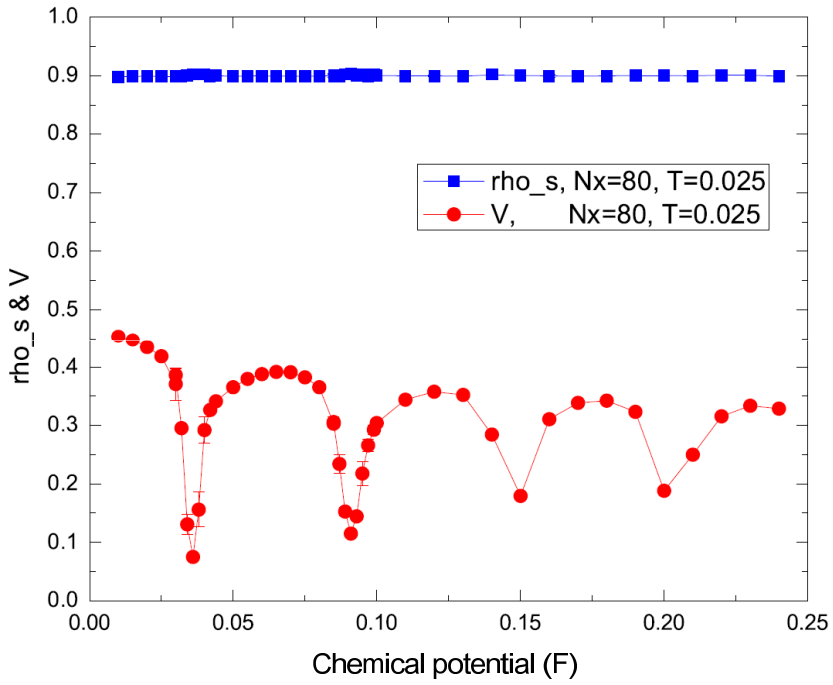

Figure 7.13: Superfluid stiffness ρ_S and speed of sound V as a function of applied chemical potential μ for size $Nx = 80$ at $T = 0.025$. Stiffness essentially does not change which allows the peaks in κ to transform into dips in V.

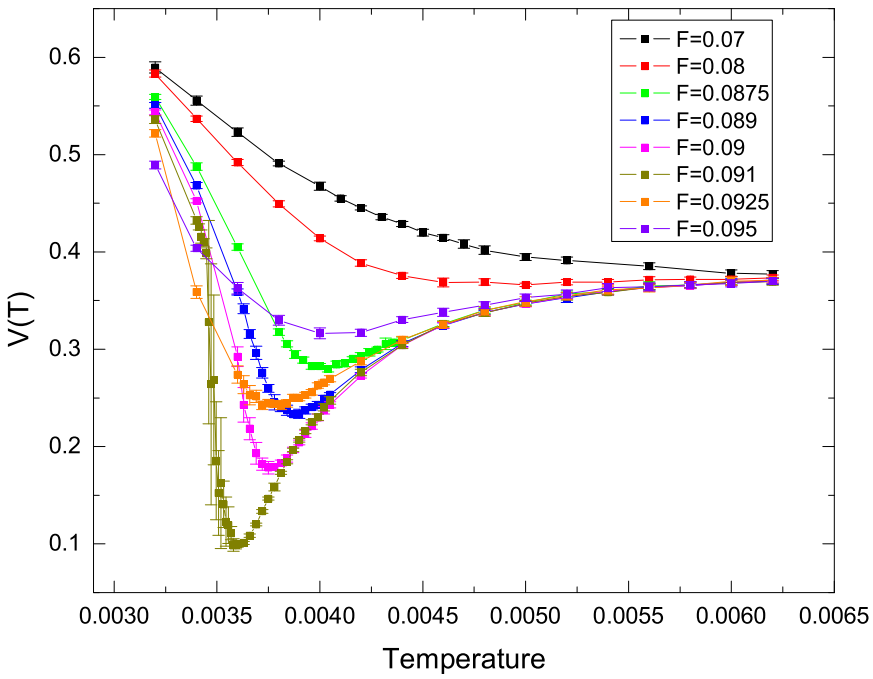

Figure 7.14: Temperature dependence of sound speed for different values of applied chemical potential for $Nx = 80$, $T_0 = 0.2$, $u_P = 0.1$. Well pronounced dip exists only in a certain range of μ

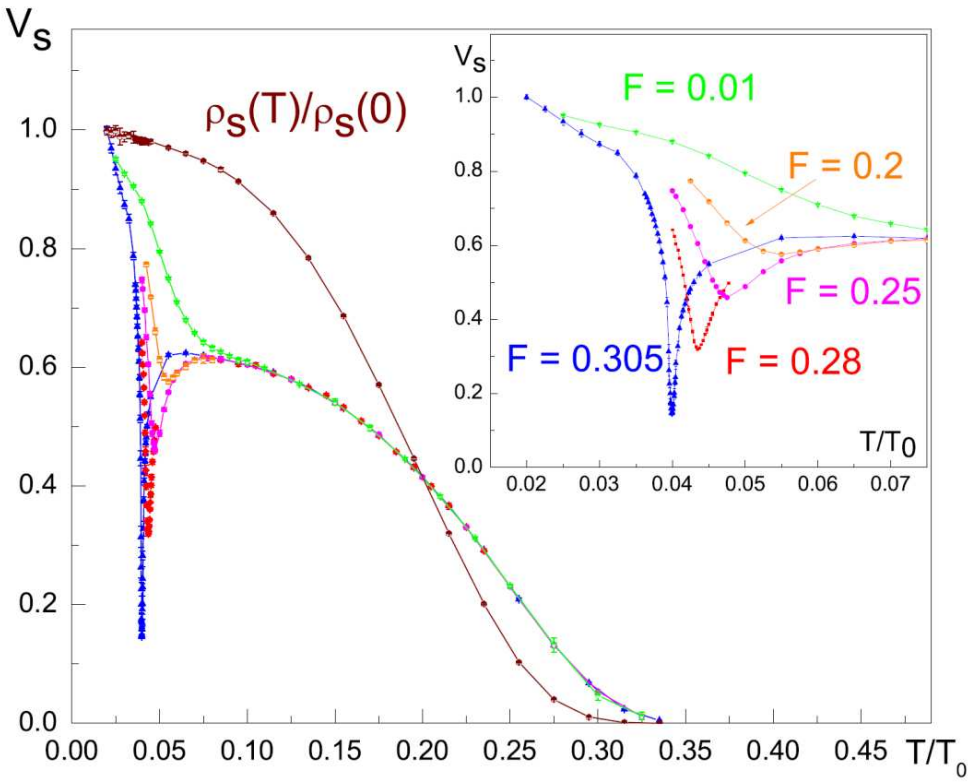

Figure 7.15: Superfluid stiffness $\rho_s(T)$ and sound velocity $V_s = \sqrt{\rho_s(T)/\kappa(T)}$ normalized by their respective low-T values for different values of applied stress F (see inset). Parameters: $L = 30$, $u_P = 3.0$, $T_0 = 0.2$

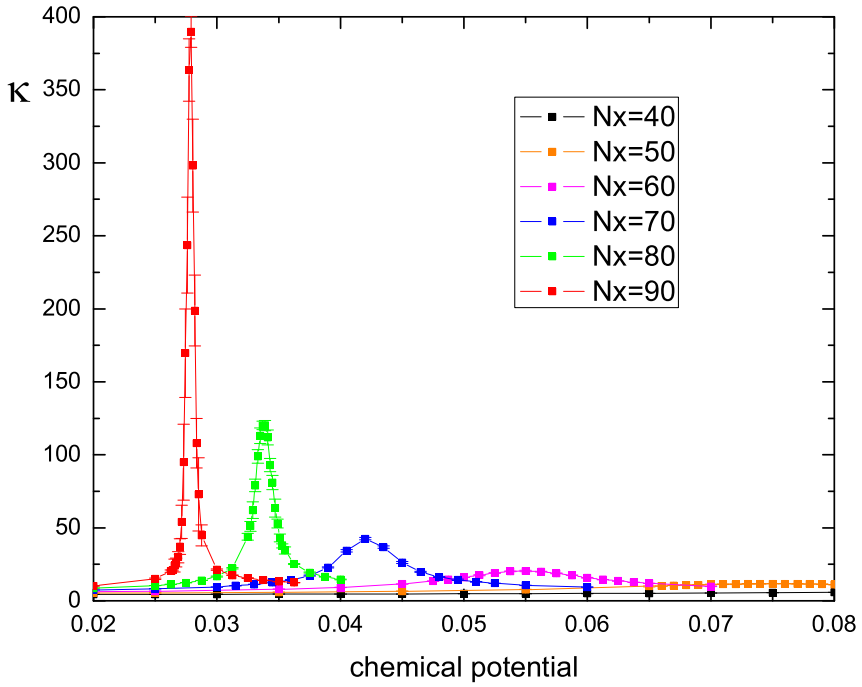

Figure 7.16: Compressibility vs chemical potential for $T_0 = 0.2$, $u_P = 0.1$, $T = 0.004$. Different curves correspond to different dislocation sizes N_x.

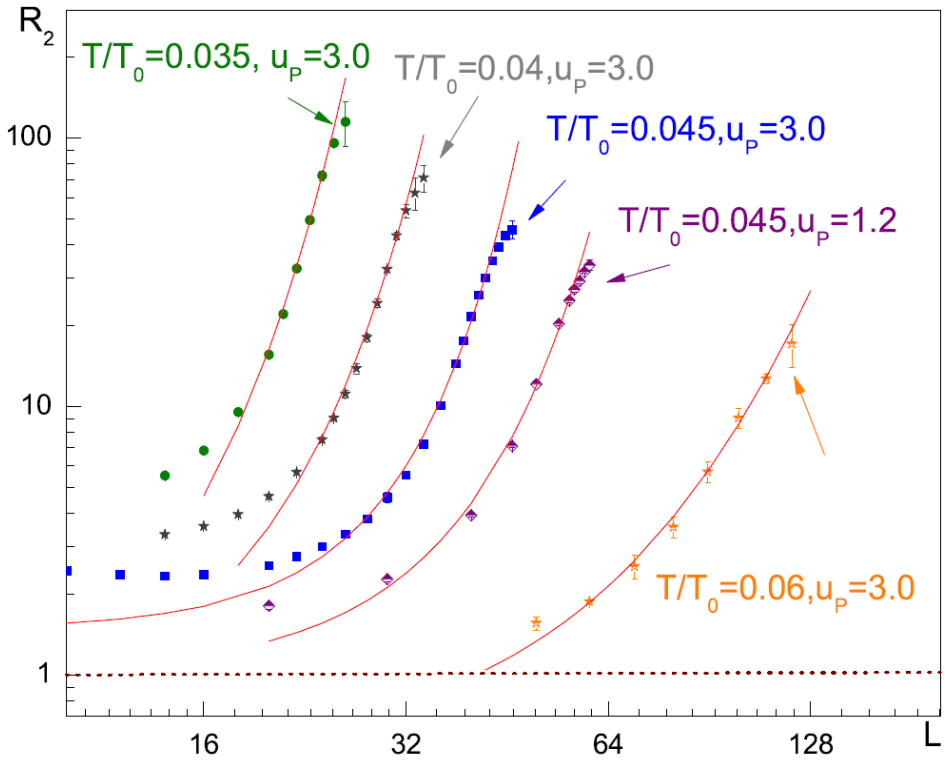

Figure 7.17: Height of the first resonant peak $R_2(F)$ vs. L for different T, u_P. The solid lines represent the fit by $R_2 = \exp(A + L/L_R) + B$ with three adjustable parameters A, L_R, B. Deviations from exponential behavior marked by arrorws signify the beginning of the hysteresis region. The dashed line is the behavior of a free-sting model $R_1 = R_2 = 1$[29]

We claim that the observed resonant-type peak is a precursor of first-order phase transition occurring in the dislocation at finite T.

7.4.2 Landau's argument: on impossibility of I-order phase transition in 1D at finite T

At this point it is necessary to discuss the argument presented by Landau on impossibility of phase coexistence in one-dimensional systems at finite temperatures [40]. Consider a linear system consisting of intervals of two different phases, marked, for

example, by blue and red colors (see Fig.7.18) , and separated by green boundaries (points).

Figure 7.18: 1D system with two phases marked by red and blued color. Green points denote the boundaries.

Let Φ_0 be the the free energy of the system excluding boundary points. To include boundaries contribution, we can consider them as a "weak" solution of these points in two phases. Therefore the energy assumes

$$\Phi = \Phi_0 + nT \ln (n/eL) + n\psi, \tag{7.13}$$

where n - number of boundary points on the length L. Therefore if we minimize the energy

$$\frac{\partial \Phi}{\partial n} = T \ln(n/L) + \psi = 0, \tag{7.14}$$

we obtain the solution

$$\frac{n}{L} = e^{-\frac{\psi}{T}}. \tag{7.15}$$

This signifies that on any given length L there is always a finite number of boundary points meaning that two phases tend to mix together and cannot therefore exist separately. It leads to the conclusion that I-order phase transition is impossible in such a system. The obtained result does not depend on the system size L since it gives the *density* of one phase in the other. Therefore any characteristics of this system should be insensitive to L.

The Landau argument is based on the assumption that the system has a local

order parameter.However, as we will show below, if you don't have the locality of the order parameter, this argument can be violated.

7.4.3 Hysteresis

The peak behavior is reversible that is the results do not depend on the direction of the force scan. As we increase the size above certain threshold value L_h, however, the system stopped exhibiting resonant peaks and started showing the hysteretic behavior. It was found that L_h grows with temperature as $L_h \approx T^{\gamma_h}$ with $\gamma_h \approx 2-3$ for $u_P = 1-3$. It should be noted that both peaks and hysteresis are observed only if $T < T_R$, otherwise dislocation exhibits free string response. The fact that $\gamma_h > 0$ is a strong indicator that the scenario of assisted single pair tunneling is not applicable here: in the latter case it should be *decreasing* with T as $\approx T^{-3/2}$ [65]. Therefore we conclude that in the rough state no clear jog-antijog pairs can be separated out and the behavior is governed by many-jog effects.

A typical hysteresis is presented on the inset in Fig. 7.19. As we increase stress (blue dots) the dislocation starts in a smooth state. As we reach F_U, it jumps into the rough state and stays there. But if we attempt to go back by decreasing F(red dots) dislocation remains in a rough state, and returns to the smooth state at $F_L \leq F_U$. The full picture of the dislocation behavior vs size L is represented on Fig. 7.19. The blue and red points signify the upper and lower hysteresis boundaries respectively. The green dots belong to the region of resonant behavior and show the positions of the peaks. All three fields scale as power laws $F_{U,L}(L) \sim L^{-\gamma_{U,L}}$ with $\gamma_U = 0.4$ and $\gamma_L = 2.7$. The strong dependence of both hysteresis boundaries on the system size violates the Landau argument (see section 7.4.2 and [40]). We attribute this to the absence of local order parameter in our system. In Landau's derivation it was

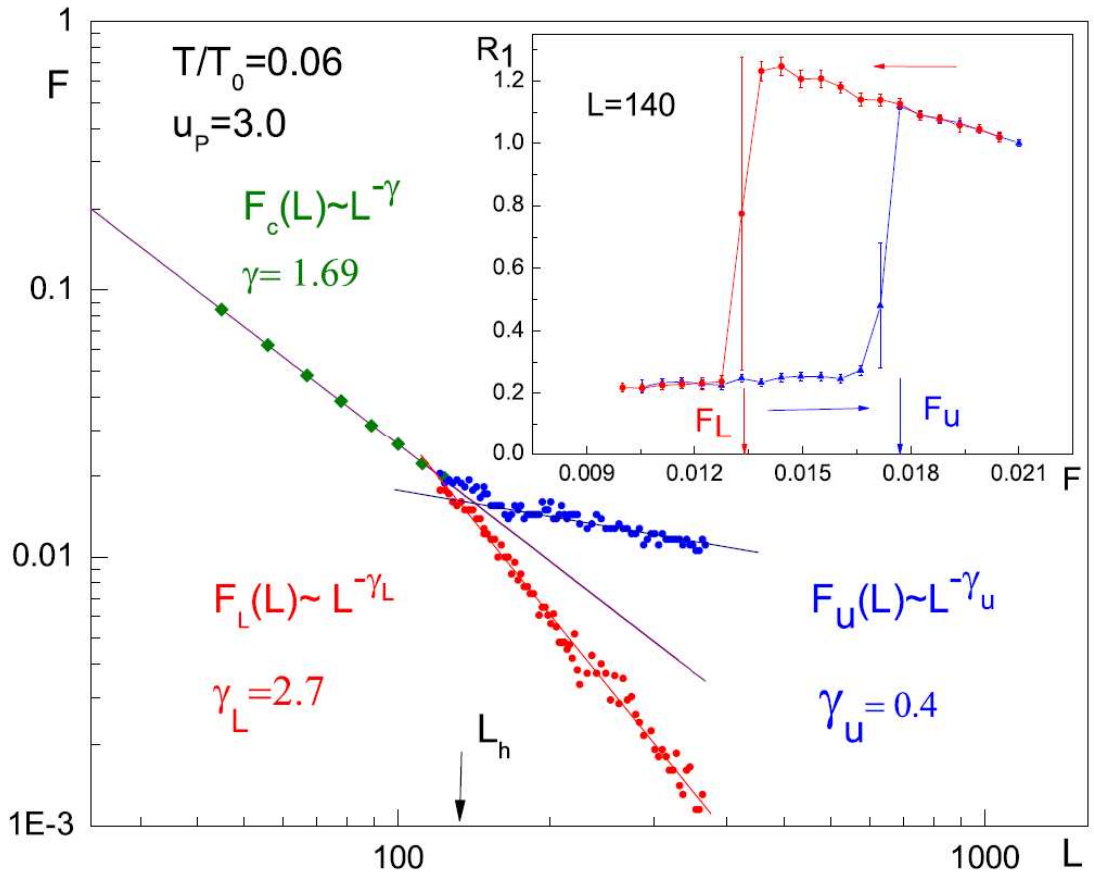

Figure 7.19: Reversible and hysteretic dislocation behavior as a function of T. The green dots: positions of the resonant peaks (reversible). The blue and red dots: the upper and lower hysteresis boundaries respectively. All three fields scale like power laws. Both hysteresis boundaries are sensitive to size L - sign of a I-order phase transition. Inset: example of typical hysteresis behavior for $L = 140$.

assumed that any point in 1D system can be assigned to a certain phase, but in our system the distinction between rough and smooth states can be made only if one looks at the whole dislocation. No separate point either having jog or not can definitely determine the phase of the system. Therefore Landau's reasoning is not applicable here. We conclude that the stress-induced roughening is a I-order phase transition in 1D at finite T.

It should be noted that the above results quantitatively do not depend on the

long-range interaction. If we set it $U_C = 0$ the system still exhibits exponentially scaled peaks and growing with L hysteresis.

Chapter 8

Summary of the results and future work

8.1 Results: the long-range interaction effects

1. 1D quantum dislocation was mapped to 2D classical system with an inclusion of long-range interaction potential. Coulomb gas approach and dual J-current model were considered. J-current model was found superior to Coulomb gas in terms of calculation ability.

2. A suppression of a dislocation compressibility was found in the presence of long-range potential at $T = 0$. It was concluded that the dislocation is in smooth state at $T = 0$ for any *arbitrary* small long-range interaction. The result was in agreement with a heuristic argument.

3. Shear modulus temperature dependencies $G(T)$ were obtained. It was found that all the data fit experimental curves by using *one* rescaling parameter – a typical kink energy. It proved a crucial role of Peierls potential in elastic

properties of dislocations and showed that the crossover from $T = 0$ to finite temperatures leads to *intrinsic* softening of $G(T)$ even if ^{3}He impurities were not present.

8.2 Results: ^{3}He impurities influence

1. Two mechanisms of ^{3}He unbinding were considered: "boiling-off" and "creeping-away".

2. MC simulations of a full non-linear dislocation action with the use of gradient expansion were conducted and it was found that the results could be fit by a gapped string model. Using this fit the gap values Δ were obtained. It was shown that Δ is linearly proportional to the impurity density. Peierls potential was found to effectively increase the gap.

3. To test a "boiling-off" theory a simple thermodynamic model for ^{3}He atoms was considered which allowed to find ^{3}He fraction on a dislocation $X(T)$. The obtained result $\Delta \propto X(T)$ was used to connect shear modulus $G(T)$ with impurity concentration $X(T)$. The actual experimental data were compared with the derived dependence $G(X(T))$. It was shown that for a reasonable amount of dislocations and impurity concentrations a pure "boiling-off" model does not fit the experimental curves.

4. MC simulations with the inclusion of Peierls potential u_P were found to fit the data very well. It showed that u_P plays a crucial role in shear modulus softening, and therefore a combination of "boiling-off" and "creeping-away" mechanisms is a more realistic description of ^{3}He unbinding.

8.3 Results: superclimbing dislocations properties

1. MC simulations of a climbing dislocation with a superfluidity along the core were conducted. Both linear and non-linear responses were investigated. In a regime of linear response a phenomenon of "giant isochoric compressibility" was observed. It was shown that the isochoric compressibility is suppressed at low T. The dependence of compressibility on the dislocation length was found to be strongly dependent on the long-range interaction.

2. The non-linear regime was discovered to possess two types of behavior: reversible and hysteresis depending on the dislocation length.

3. The reversible region manifested itself in ratchet-like jumps in full response and sharp peaks in differential one. Stress threshold was found to be a *macroscopically* small quantity.

4. A resonant peak in compressibility results in a dip in a speed of sound. This effect was proposed to be an explanation for a sudden drop of a flow rate observed in "UMASS" sandwich experiments. It was suggested to study the flow rate as a function of applied stress at fixed T in order to clarify the origin of the dip.

5. The threshold dislocation length above which hysteresis develops was found to *increase* with T contradicting the scenario of single pair tunneling where it *decreases* with temperature.

6. Hysteresis boundaries were found to be strongly sensitive to the dislocation length in the whole range of measurements. It signifies that the stress-induced roughening is a I-order phase transition in 1D at finite T.

7. It was demonstrated that the obtained results do not depend on the long-range interaction.

8.4 Directions of future work

In all our research we considered the gliding or superclimbing dislocations which form a 3D network insider the bulk – a dislocation "forest". But under the condition of large applied stresses and density changes, as it happens in UMASS sandwich experiments dislocations form a considerable amount of prismatic ballistic loops which can significantly affect the material properties. Superclimbing loops can be partially responsible for NCRI fraction, for the abnormally small TO critical velocity and can explain the heat capacity bump. The mechanisms of loops creation, the estimation of their amount and evaluation of the dynamics inside the bulk are the problems for a future research.

All the performed experiments on solid ^{4}He revealed an unusually strong sensitivity to the impurity concentration so we find it quite important to understand how the presence of ^{3}He atoms modifies the dip-anomaly. Impurities pinning can be the major factor in determining the dislocation segment length, which will exponentially grow as T rises due to ^{3}He unbinding. This will insure that the resonant peaks condition will often be met by some dislocations in a narrow temperature range. It can also explain the unsuccessful attempts to observe the change in a flux rate in the dip region. Thus the investigation of ^{3}He effect on a stress-induced roughening is an important problem to consider.

Since MC simulations are limited only to the measurements of the thermodynamically-equilibrated states it would be rather important to simulate the *dynamics* of the superflow along the dislocation network (work in progress). We plan to simulate

Shevchenko state [21] and relate it ti the UMASS sandwich experiment setup. The key question to answer is how phase slips affect the observed temperature dependencies [34]-[39].

8.5 Publications

The results of the conducted research were published in the following papers:

1. D. Aleinikava, E. Dedits, A.B.Kuklov, D. Schmeltzer. "Mechanical and superfluid properties of dislocations in solid ^{4}He". arXiv:0812.0983

2. D. Aleinikava, E. Dedits, A.B.Kuklov, D. Schmeltzer. "Dislocation roughening in quantum crystals". Europhys. Lett., **89** 46002 (2010).

3. D. Aleinikava, E. Dedits, A.B. Kuklov. "Glide and superclimb of dislocations in solid ^{4}He". J. Low Temp. Phys. (2011) 162: 464-475. arXiv:1006.5228.

4. D. Aleinikava, A.B.Kuklov. "Stress-induced dislocation roughening: a phase transition in one dimension at finite temperature". Phys. Rev. Lett. **106**, 235302 (2011), arXiv:1102.5522.

5. D. Aleinikava, A.B.Kuklov. "The role of ^{3}He impurities in the stress induced roughening of superclimbing dislocations in solid ^{4}He". arXiv:1108.1182 (2011), To be published in Proceedings of LT26, Beijing, 2011.

6. D.Aleinikava, A.B.Kuklov. "Interplay of non-linear elasticity and dislocation-induced superfluidity in solid ^{4}He". arXiv:1110.5884, submitted as an invited paper to the special issue of J. Low Temp. Phys. dedicated to supersolidity.

The results were also presented by Darya Aleinikava at the following meetings:

1. American Physical Society March Meeting 2009. Oral presentation "Absence of Dislocation Quantum Roughening in Solid ^{4}He"

2. Gotham Metro Condensed Matter Meeting, Spring 2009. Talk "Mechanical and superfluid responses of dislocations in solid ^{4}He".

3. American Physical Society March Meeting 2010. Oral presentation "Mutual effect of ^{3}He impurities and Peierls potential on shear modulus softening in solid ^{4}He".

4. International workshop Supersolidity 2010. Poster "Non-linear superclimb of dislocations in solid ^{4}He".

5. Gotham Metro Condensed Matter Meeting, Fall 2010. Poster "Superclimb of dislocations in solid ^{4}He".

6. American Physical Society March Meeting 2011. Oral presentation "Superclimb of dislocations in solid ^{4}He".

7. Gotham Metro Condensed Matter Meeting, Spring 2011. Talk "Superclimb of dislocations in solid ^{4}He".

8. International workshop Supersolidity 2011. Invited talk "Superclimb and the anomalies of solid ^{4}He".

and were used in the following talks:

1. International Workshop Supersolids 2008, ICTP, Trieste, Italy. Talk given by Anatoly Kuklov "Dislocations and supersolidity in ^{4}He".

2. American Physical Society March Meeting 2009. Oral presentation given by Eugene Dedits "Classical roughening of dislocations and the effect of shear modulus softening in solid ^{4}He".

3. International workshop Supersolidity 2010, Paris, France. Invited talk given by Anatoly Kuklov.

4. International symposium on quantum fluids and solids 2010, Grenoble, France. Invited talk given by Anatoly Kuklov "Quantum dislocations in solid ^{4}He".

5. American Physical Society March Meeting 2011. Invited talk given by Anatoly Kuklov "Superclimb of dislocations in solid ^{4}He".

6. 26th International Conference on Low Temperature Physics. Talk given by Anatoly Kuklov.

Appendix A

Coulomb gas simulations: failure of the direct approach

We are interested in calculating the energy and correlation function of a two dimensional gas of charges described by the partition function

$$Z = \sum_{\{N_i^+, N_i^-\}} \left(\prod_i \frac{\alpha^{N_i^+ + N_i^-}}{N_i^+! N_i^-!} \right) e^{-\frac{1}{2}\sum_{i \neq j} m_i m_j U(\mathbf{x}_i - \mathbf{x}_j)} \tag{A.1}$$

with the total energy

$$E = \frac{1}{2} \sum_{i \neq j} m_i m_j U(\mathbf{x}_i - \mathbf{x}_j). \tag{A.2}$$

So we start with the empty lattice of size Nx*Nt (with periodic boundary conditions) and use only one type of updates (enough to generate an ergodic process). That is we randomly choose two lattice sites and try to put there one negative charge and a positive one (to ensure total charge neutrality). We also allow the charge in a site to have only one of three possible values +1, 0, 1. The acceptance ratio is $R = e^{-\Delta E} \alpha^{\Delta n}$ where Δn is the change in the total number of charges in the lattice.

One of the ways to see in which state (plasma or insulator) the system consists of plotting the graph of the inverse dielectric permittivity as a function of a distance between two additional fixed charges. So we first have to compute the energy of the system as we described. Then we place an additional pair of charges at, say, distance $Nx/2$ between each other and compute the energy of this system. Dielectric permittivity can be computed as $\frac{1}{\varepsilon(x)} = \frac{E_{with\,pair} - E_{no\,pair}}{E_{bare}}$ where E_{bare} is the bare energy between two additional charges. If $\frac{1}{\varepsilon(x)}$ dies off as we increase Nx it means that the charges in the gas screen each other which implies that the gas is in the plasma state. If, on the contrary, $\frac{1}{\varepsilon(x)}$ reaches some constant value then the system is an insulator. The critical value for stiffness k is [52] 1/2, below which the system is plasma, above insulator. It is expected, as we have seen, that in the presence of long-range interaction term the system will always be in plasma state. For the original model it means that the dislocation will always be in smooth state.

If instead of increasing the size of the system we will just change the position of two fixed charges, then graphs $\frac{1}{\varepsilon(x)}$ at $k < k_{critical}$ for two different sizes should diverge with increasing distance between the charges. If $k > k_{critical}$ the graphs should coincide.

We did some preliminary calculations for the systems of sizes $Nx = 24$ and $Nx = 48$ with regular (no long-range) potential, which you see on the Figure A.1. They showed that for not too big sizes of the systems the errors are considerable enough to prevent us from seeing the difference between the graphs with increasing distance between the fixed charges. Bigger sizes should be considered and smaller errors should be achieved in order to use this method to actually see BKT transition.

It is also interesting to calculate the correlation function $\langle \phi(\mathbf{x})\, \phi(0) \rangle$. The classical action for a system (no long-range interaction) in the presence of the external field is

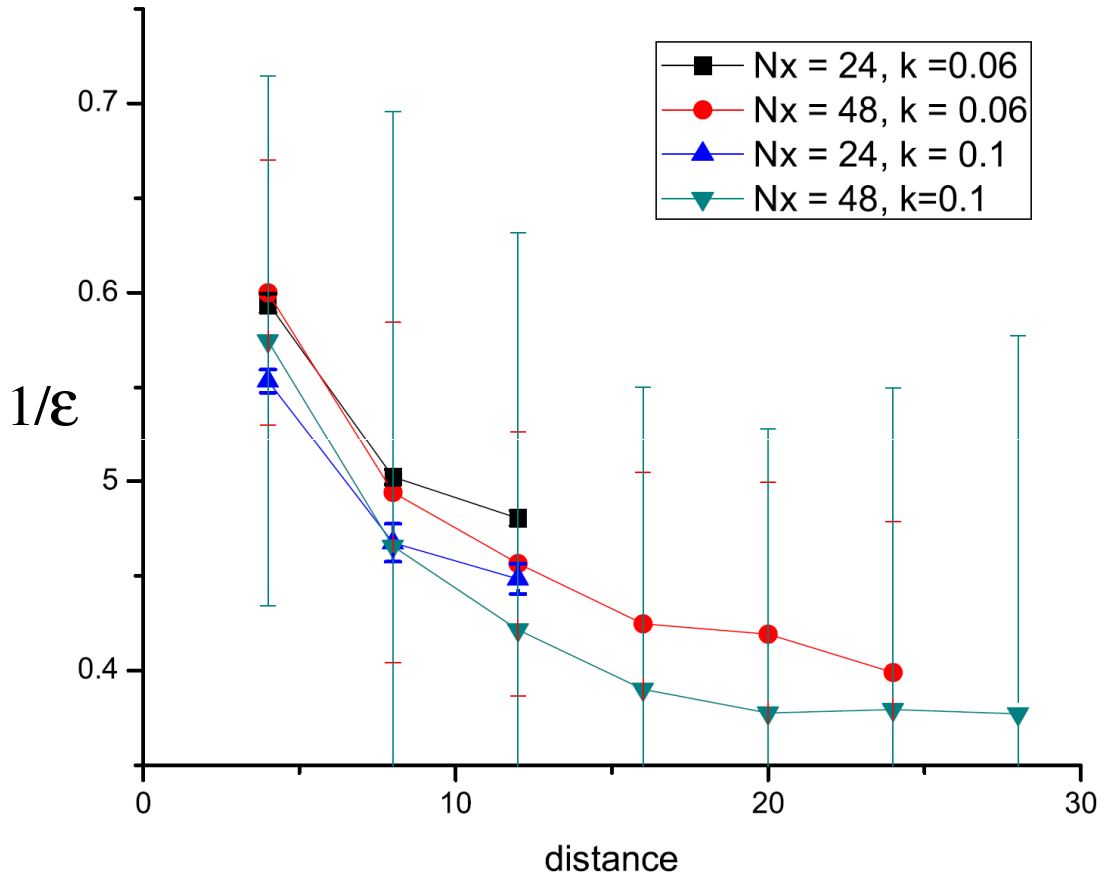

Figure A.1: Inverse dielectric permittivity vs. the distance between additional pair of charges for $Nx = 24$, $Nx = 48$ and $k = 0.1$, $k = 0.06$.

$$S_f = \int_0^{\beta} d\tau \int_0^{L_x} dx \left[\frac{1}{2K} (\nabla\phi)^2 - \alpha \cos(\phi) - f \cdot \phi \right], \tag{A.3}$$

where β is an imaginary time identified as an inverse temperature: $\beta = 1/T$. The average is

$$\langle \phi \rangle = \frac{\int \mathbf{D}\phi e^{-S_f} \phi}{\int \mathbf{D}\phi e^{-S_f}}. \tag{A.4}$$

It is expected to be linearly proportionally to the external force f, so after expansion of the exp-function in f we can leave only linear in f terms (similar to procedure

in Section 3.2.1)

$$\langle \phi(x,\tau) \rangle = \frac{\int e^{-S_0} \mathbf{D}\phi \int dx' d\tau' \phi(x',\tau') \phi(x,\tau) f(x',\tau')}{\int e^{-S_0} \mathbf{D}\phi}. \tag{A.5}$$

Therefore, response to the external field f is determined by the correlation function with no external field present

$$\langle \phi(x,\tau) \rangle_{S_f} = \int dx' d\tau' \langle \phi(x',\tau') \phi(x,\tau) \rangle f(x',\tau'). \tag{A.6}$$

In case of constant f it becomes even simpler

$$\langle \phi(x,\tau) \rangle_{S_f} = f_0 \int dx' d\tau' \langle \phi(x',\tau') \phi(x,\tau) \rangle. \tag{A.7}$$

So we see that the calculation of $\langle \phi(x',\tau') \phi(x,\tau) \rangle$ can give valuable information about the behavior of a system.

The partition function is given by $Z_f = \int e^{-S_f} \mathbf{D}\phi$. It is obvious that the correlation function is, consequently,

$$\langle \phi(x',\tau') \phi(x,\tau) \rangle = \left. \frac{\frac{\partial^2 Z_f}{\partial f(x,\tau) \partial f(x',\tau')}}{Z_0} \right|_{f=0}. \tag{A.8}$$

The expression for the estimator in two-dimensional Coulomb gas is

$$\langle \phi(i) \phi(j) \rangle_{est} = U(i-j) - \sum_k U(i-k) m(k) \sum_{k'} U(i-k') m(k'). \tag{A.9}$$

The simulation scheme, types of updates, etc. are the same as already discussed.

It is worth mentioning another away to tell the difference between plasma and

insulator states using correlation function. Instead of calculating the energies of the gas, we can collect charge correlation function $c(\mathbf{x}) = \langle m(\mathbf{x})m(0)\rangle$, then [52] the inverse of the Fourier transform of dielectric permittivity is very simply connected to the Fourier transform of the correlator we collect $\frac{1}{\varepsilon(\mathbf{q})} = 1 - U_0(\mathbf{q})c(\mathbf{q})$, where $U(\mathbf{q}) = \frac{K}{\left(\sin^2\left(\frac{q_x}{2}\right)+\sin^2\left(\frac{q_t}{2}\right)\right)}$. In the plasma state the function $\frac{1}{\varepsilon(\mathbf{q})}$ starts from zero at $q \to 0$ and gradually increases to 1 for larger q. In the insulator state $\frac{1}{\varepsilon(\mathbf{q})}$ is also 1 at large $\mathbf{q}$, but it starts from a non-zero value at small $\mathbf{q}$. In actual simulation, it is not necessary to collect two-dimensional correlator, it is enough to gather only $c(x)$, normalizing it on the collected separately $c(0,0) = \langle m^2(0)\rangle = \frac{\langle N\rangle}{Nx*Nt}$. To determine the state of the system one can plot $\frac{1}{\varepsilon(q_x,0)} = 1 - U_0(q_x,0)c(q_x,0)$.

On the Figure A.2 one can see the results of simulations of the system with no long-range interaction for $k = 0.06$ and $k = 0.72$ of the size $Nx = 80$, $Nt = 4$. As it is expected for $k = 0.06 < k_{critical}$ the graph starts from zero gradually increasing afterwards which means that the system is in the plasma state. On the contrary, for $k = 0.72 > k_{critical}$ the graph starts from some non-zero value, which signifies that the system passed through phase transition and turned into insulator state. Therefore, on these graphs one can clearly see the difference between plasma and insulator states.

Since in order to determine the state of the system one really does not need the whole curve but only the value $\frac{1}{\varepsilon(0)}$ it is tempting for practical purposes to find the direct expression for this value. The expansion in Taylor series around $q = 0$ gives $\frac{1}{\varepsilon(0)} - 1 = 2k \sum_{x=0}^{Nx/2} c(x)\, x^2$. It is really much easier to calculate this number instead of the whole correlator and its Fourier transform but there is a price to pay: the convergence of $\frac{1}{\varepsilon(0)} - 1$ for sizes 20*20 is very poor since $U_0(q_x,0)c(q_x,0) \xrightarrow[q_x\to 0]{} \frac{c(q_x,0)}{q_x^2}$, so even small errors in correlator results in enormous errors in $\frac{1}{\varepsilon(0)} - 1$ for big sizes. Therefore, for big systems one still have to use the old method with plotting the whole curve.

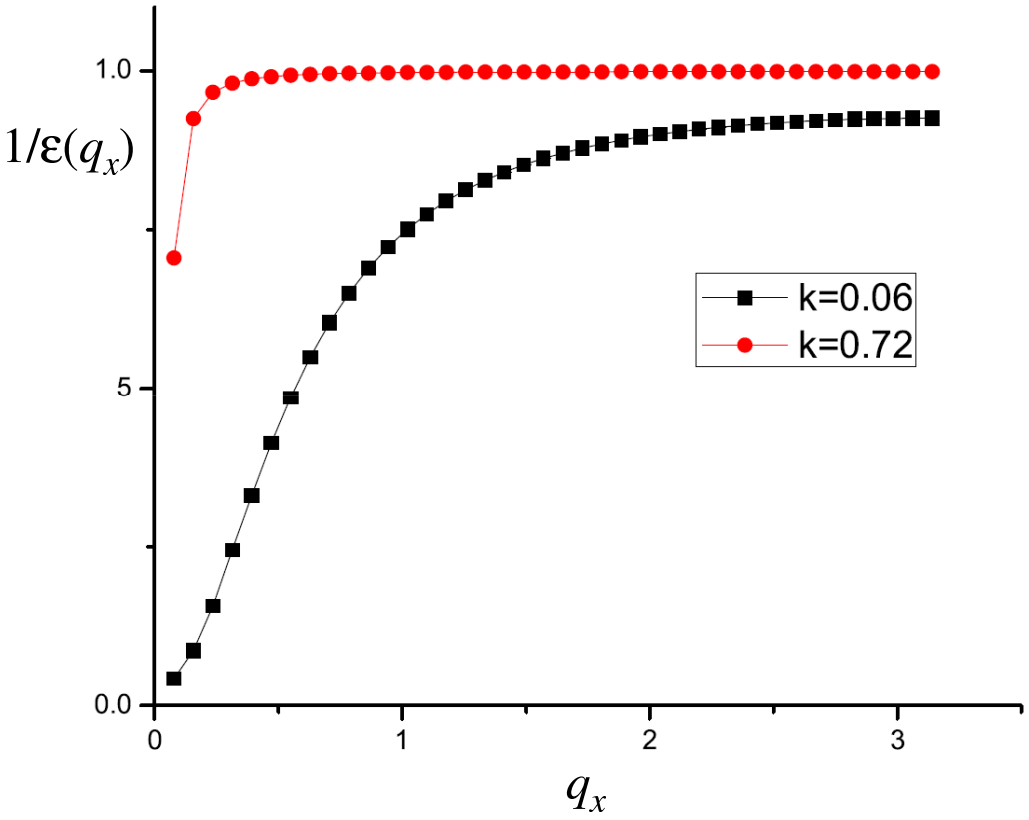

Figure A.2: Inverse dielectric permittivity function $1/\varepsilon$ vs. wave vector q_x at $k = 0.06$ and $k = 0.72$, $Nx = 80$, $Nt = 4$.

Another interesting thing to observe in our system is the crossover between quantum-mechanical behavior and purely classical one. In classical picture pinched dislocation can be considered as a string with fixed ends with Hamiltonian

$$H = \int_0^L dx \frac{\sigma}{2} \left(\frac{\partial y}{\partial x} \right)^2 = \sum_q \frac{\sigma}{2L} q^2 \left| y_q \right|^2, \tag{A.10}$$

where $2L$ is the distance between the ends, σ is the tension and y is the displacement. The correlation function

$$\langle y(x)\, y(0) \rangle = \frac{1}{L} \sum_q \left| y_q \right|^2 e^{iqx} = \int \frac{dq}{2\pi} \frac{T}{\sigma q^2} e^{iqx} \propto \frac{T}{\sigma} |x|, \tag{A.11}$$

that is linearly proportional to $|x|$. In our quantum description of a 1D dislocation, after mapping, we deal with 2D classical system with action

$$S = \int_0^{\hbar/k_B T} d\tau \int_0^{L_x} dx \left[\frac{\rho}{2} (\partial_t y)^2 + \frac{\sigma}{2} (\partial_x y)^2 - \alpha \cos y \right] \tag{A.12}$$

with $L_y = \hbar/k_B T$. The dependence of the correlator on $|x|$ is still linear but with different $\sigma(T)$, which now depends on the temperature. The classical behavior here can be obtained in the limit $L_t \to 0$. Thus, changing the size of the system (in t-direction) and tracking the dependence of the correlator $\langle y(x)\, y(0) \rangle$ on $|x|$, we can obse

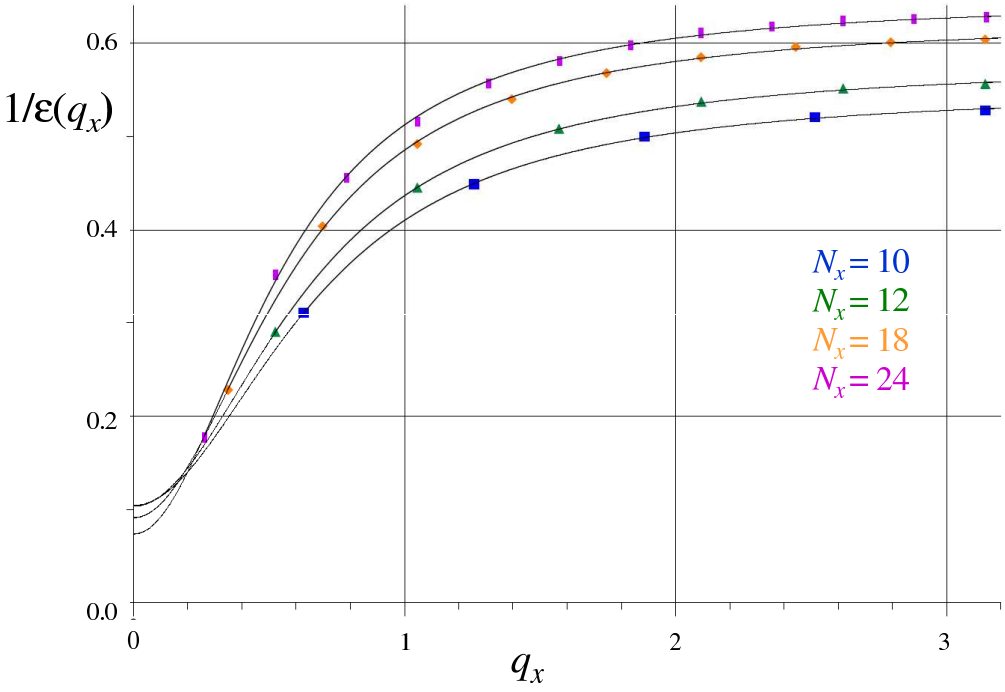

Figure A.3: Inverse dielectric permittivity function $1/\varepsilon$ vs. wave vector q_x at $k = 0.64$ for different sizes of the system $Nx = Nt$. The data are fitted by $y = A + \frac{B}{1+Cx^2}$, where $\frac{1}{\varepsilon(0)} = A + B$.

On the Figure A.3 one can see the results of simulations for the systems with

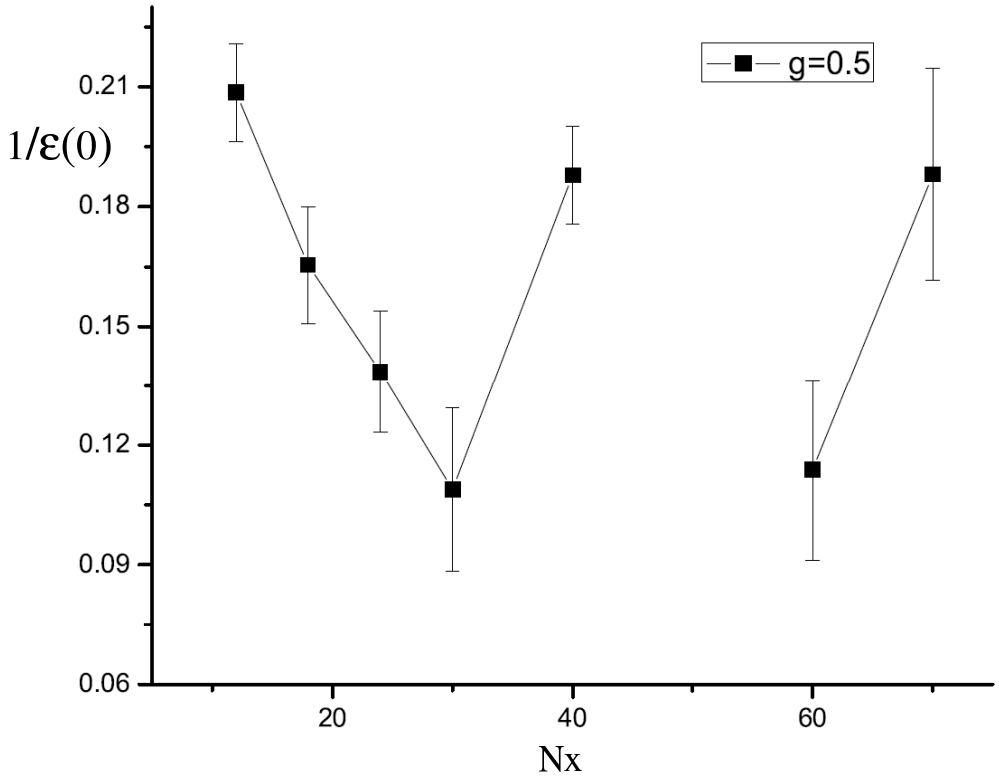

Figure A.4: $\frac{1}{\varepsilon(0)}$ vs. size of a system Nx, $g = 0.5$, $k = 0.64$.

long-range potential present $g = 1$, $k = 0.64 > k_{critical}$. Here g denotes the strength of long-range interaction. Function $\frac{1}{\varepsilon(q_x)}$ is fitted with the function $y = A + \frac{B}{1+Cx^2}$, where $\frac{1}{\varepsilon(0)} = A + B$. As we see, as the size of the system increases, value of $\frac{1}{\varepsilon(q_x)}$ is going down, which signifies that the system is really in plasma state as we expected.

However, if we try to increase the size of the system, we encounter major difficulties. On the Figure A.4 one can see the calculation results of $\frac{1}{\varepsilon(q_x)}$ as a function of a size of a system in the presence of long-range potential with $g = 0.5$ at $k = 0.64$ $> k_{critical}$. As mentioned before, our expectations are that it should go to zero if size increases to manifest plasma state. For small sizes $Nx < 40$ dielectric permittivity is really going down, but the results for bigger sizes acquire quite large simulation errors. Long waiting times do not improve the situation which shows bad convergence

of Monte-Carlo simulations process. The same bad results were achieved for different values of g. It proves that the simulations of Coulomb gas are not efficient to analyze the behavior of the system in the presence of long-range potential.

Appendix B

Gradient expansion approach: general technique

Here we introduce a technique which is called a "gradient expansion" and is based on using Taylor series for the exponent, containing gradient term, in the partition function.

Let's start from a basic hamiltonian of SG model (neglecting long-range interactions):

$$H = \sum_{\langle ij \rangle} \frac{1}{K} (y_i - y_j)^2 - \sum_i 2\alpha \cos(B' y_i) \tag{B.1}$$

and perform rescaling (to eliminate K as a coefficient)

$$H = \sum_{\langle ij \rangle'} \frac{1}{K} \frac{K}{2} (y_i - y_j)^2 - \sum_i 2\alpha \cos(B' \sqrt{\frac{K}{2}} y_i) = \sum_i \left(2y_i^2 - 2\alpha \cos(B y_i)\right) - \sum_{\langle ij \rangle'} y_i y_j, \tag{B.2}$$

where $B = B'\sqrt{K/2}$ and $\sum_{\langle ij \rangle'}$ denotes the summation over all non-repeatable bonds

$\langle ij \rangle$.

Then we obtain

$$H = \sum_i H_i - \sum_{\langle ij \rangle'} y_i y_j. \tag{B.3}$$

After performing the expansion on each bond

$$e^{y_i y_j} = \sum_{\{N_{ij}\}} \frac{(y_i y_j)^{N_{ij}}}{N_{ij}!} \tag{B.4}$$

the partition function becomes

$$Z = \int Dy \exp(-H) = \prod_i \int dy_i \exp\left(-H_i\right) \prod_{\langle ij \rangle'} \sum_{\{N_{ij}\}} \frac{(y_i y_j)^{N_{ij}}}{N_{ij}!}, \tag{B.5}$$

$$\prod_{\langle ij \rangle'} \sum_{\{N_{ij}\}} \frac{(y_i y_j)^{N_{ij}}}{N_{ij}!} = \prod_i \sum_{\{N_{ij}\}} y_i^{k(i)} \prod_{\langle ij \rangle'} \frac{1}{N_{ij}!}, \tag{B.6}$$

where $k(i) = \sum_{\langle j \rangle = i} N_{ij}$ are called "site charges".

Therefore

$$Z = \sum_{\{N_{ij}\}} \left(\prod_i C(i) \right) \prod_{\langle ij \rangle'} \frac{1}{N_{ij}!}, \tag{B.7}$$

where we introduced

$$\begin{aligned} C(i) &= \int dy_i \exp\left(-2y_i^2 + 2\alpha \cos(B y_i)\right) y_i^{k(i)} = \\ &= \sum_{\{n_+, n_-\}} \frac{\alpha^{n_+ + n_-}}{n_+! n_-!} \int dy_i y_i^{k(i)} e^{-2y_i^2 + y_i i B (n_+ - n_-)}. \end{aligned} \tag{B.8}$$

When we suggest update in WA only few sites are affected by it, it follows from (B.7) that the acceptance ratio will bear a very simplistic form – a ratio of $C(i)$ for the updated site multiplied by the corresponding change in N_{ij} factors:

$$C(i) = \sum_{\{n_+,n_-\}} \frac{\alpha^{n_++n_-}}{n_+!n_-!} e^{-\frac{B^2(n_+-n_-)^2}{8}} \int dy_i \left(y + \frac{iB(n_+-n_-)}{4} \right)^{k(i)} e^{-2y_i^2}. \quad \text{(B.9)}$$

If one uses binomial formula once again, the result will be

$$C(i) = \sum_{l=0}^{k(i)} \sum_{\{n_+,n_-\}} \frac{\alpha^{n_++n_-}}{n_+!n_-!} e^{-\frac{B^2(n_+-n_-)^2}{8}} \frac{k(i)!}{l!(k(i)-l)!} \left(\frac{iB(n_+-n_-)}{4} \right)^{k(i)-l} \int dy_i y_i^l e^{-2y_i^2}. \quad \text{(B.10)}$$

The integral depends on whether l is odd or even. Introducing $k(s) = 2p'$ and $l = 2p$, and evaluating the integral one obtains

$$\begin{aligned} C(k(s) = 2p') = & \sum_{n,m} \frac{\alpha^n}{m!\,(n-m)!} e^{-\frac{B^2}{8}(n-2m)^2} \\ & \times \sum_{p=0}^{p'} \frac{(2p')!(2p-1)!!}{(2p'-2p)!(2p)!} \left(\frac{iB(n-2m)}{4} \right)^{2(p'-p)} \frac{\sqrt{\pi}}{2^{2p+1/2}}. \end{aligned} \quad \text{(B.11)}$$

Due to α being small one can truncate the series at $n = 1$

$$\begin{aligned} C(2p') = & \frac{(2p'-1)!!}{2^{2p'+1/2}} \sqrt{\pi} + \\ & + \sum_{m=0}^{1} \alpha e^{-\frac{B^2}{8}(n-2m)^2} \sum_{p=0}^{p'} \frac{(2p')!(2p-1)!!}{(2p'-2p)!(2p)!} (-1)^{(p'-p)} \left(\frac{B(n-2m)}{4} \right)^{2(p'-p)} \frac{\sqrt{\pi}}{2^{2p+1/2}}. \end{aligned} \quad \text{(B.12)}$$

Both terms for $m = 0$ and $m = 1$ are the same thus we get

$$C(2p') = \frac{(2p'-1)!!}{2^{2p'+1/2}}\sqrt{\pi} + \sqrt{2\pi}\alpha e^{-\frac{B^2}{8}} \sum_{p=0}^{p'} \frac{(2p')!(2p-1)!!}{(2p'-2p)!(2p)!} (-1)^{(p'-p)} \left(\frac{B}{4}\right)^{2(p'-p)} \frac{1}{2^{2p}}. \tag{B.13}$$

Now the normalized $C(i)$ has the following form

$$\frac{C(p')}{C(p'_{n=0})} = 1+2\alpha e^{-\frac{B^2}{8}} \sum_{p=0}^{p'} (-1)^{(p'-p)} \left(\frac{B^2}{4}\right)^{(p'-p)} \frac{(2p')!(2p-1)!!}{(2p'-2p)!(2p)!\,(2p'-1)!!} = 1+\alpha F(p'), \tag{B.14}$$

where $F(p')$ is the following function

$$F(p') = 2e^{-\frac{B^2}{8}} \sum_{p=0}^{p'} (-1)^{(p'-p)} \left(\frac{B^2}{4}\right)^{(p'-p)} \frac{(2p+1)*...*(2p')}{1*2*...*(2p)} \frac{1}{(2p+1)*...*(2p'-1)}. \tag{B.15}$$

Appendix C

Superclimbing dislocations: simulations

C.1 Action

We consider response on static force $f = f_0 f'(x)$ of non-slanted and strongly pinned climbing dislocation. Here f_0 is amplitude and $f'(x)$ can be chosen as $f' = 1$ (uniform force) or $f' = \sin(q_1 x)$, where $q_1 = 2\pi/N_x$ is the lowest harmonic consistent with total mass conservation during climb. The spatial boundary condition is $y(0,t) = y(N_x,t) = 0$, where $b = 1$ is Burgers vector; $\beta = N_t$-periodicity along imaginary time is retained. The original action is

$$
\begin{aligned}
H &= H_{SF} + H_{dis}, && \text{(C.1)}\\
H_{SF} &= \sum_{x,t} [i(\rho + n_0)(\nabla_t \phi + 2\pi m_t) + \frac{\rho_s}{2}(\nabla_x \phi + 2\pi m_x)^2 + \frac{g}{2}(\rho - y)^2], && \text{(C.2)}\\
H_{dis} &= \sum_{x,t} \left[\frac{1}{2K_d} \left((\nabla_t y)^2 + V_d^2 (\nabla_x y)^2 \right) - \alpha \cos\left(B y(x,t)\right) - f y(x,t) \right], && \text{(C.3)}\\
y(0,t) &= y(N_x,t) = 0 \quad y(x, t+\beta) = y(x,t); \quad B = 2\pi && \text{(C.4)}
\end{aligned}
$$

Here ϕ is superfluid phase, with the integer field m_x, m_t introduced to insure modulo 2π definition of ϕ;ρ stands for density of liquid part of the core, with n_0 being fractional filling; $g = 1/\rho_0$ describes energy required to build the solid core from arrived matter; H_{dis} is energy of climbing dislocation in terms of speed velocity V_d and Peierls potential α.

We want to integrate out ρ as $\exp(-H') = \int D\rho \exp(-H)$ and obtain renormalized action. Given the boundary conditions for y, we have to impose similar ones for ρ. Namely, $\rho(x = 0, t) = \rho(x = N_x, t) = 0$. This corresponds to the situation when two ends of the dislocation are in a good contact with large SF reservoirs. Then, we obtain

$$
\begin{aligned}
H' &= H_{SF} + H_{dis}, && \text{(C.5)}\\
H_{SF} &= \sum_{x,t} [i(y + n_0)(\nabla_t \phi + 2\pi m_t) + \frac{1}{2K_s}(\vec{\nabla}\phi + 2\pi\vec{m})^2], && \text{(C.6)}\\
H_{dis} &= \sum_{x,t} \left[\frac{1}{2K_d} \left((\nabla_t y)^2 + V_d^2 (\nabla_x y)^2 \right) + \frac{u}{2}(y(x,t) + P)^2 - f y(x,t) \right], && \text{(C.7)}\\
y(0,t) &= 0;\ y(N_x, t) = 0, \quad y(x, t+\beta) = y(x,t); \quad u = (2\pi)^2 \alpha, && \text{(C.8)}
\end{aligned}
$$

where we switched to units where SF sound velocity is unity and K_s stands for SF Luttinger parameter; V_d is now measured in units of SF velocity. Here we also used Villain approximation [59] for $\cos(By)$ according to

$$
\alpha \cos\left(By(x,t)\right) \to -\frac{\alpha}{2}(2\pi y(x,t) + 2\pi P)^2 = -\frac{u}{2}(y(x,t) + P)^2 \qquad \text{(C.9)}
$$

with $P(x,t) = 0, \pm 1, \pm 2, ...$ similar to (5.20).

This action is quadratic in ϕ and y. So, we integrate them out. For the field $\vec{m}$ we use Poisson summation $\exp(-H'') = \sum_{\vec{J}} \int D\vec{m} \int D\phi \exp(-H' - 2\pi i \sum_{x,t} \vec{J}\vec{m})$, with

$\vec{J}$ being integer. For H'' we get

$$H'' = H_1 + H_2, \tag{C.10}$$

$$H_1 = \sum_{x,t} [\frac{K_s}{2} J_x^2 + \frac{K_s}{2}(J_t + n_0 + y)^2], \tag{C.11}$$

$$\vec{\nabla}\vec{J} = 0, \quad J_t(x = 0, t) = J_t(x = N_x, t) = 0;$$

$$H_2 = \sum_{x,t} \left[\frac{1}{2K_d} \left((\nabla_t y)^2 + V_d^2 (\nabla_x y)^2 \right) + \frac{u}{2}(y(x,t) + P)^2 - f y(x,t) \right]. \tag{C.12}$$

Next step is integrating out y by using the Fourier basis

$$y(x,t) = \sqrt{\frac{2}{N_x N_t}} \sum_{n_x = 1,2,...N_x - 1, n_t = 0,1,2,..N_t - 1} y_{q_x, q_t} \sin(q_x x) \exp(i q_t t), \tag{C.13}$$

where $q_x = \pi n_x / N_x$, $q_t = 2\pi n_t / N_t$. Finally,

$$\tilde{H} = H_1 + H_2 \tag{C.14}$$

$$H_1 = \sum_{x,t} [\frac{K_s}{2} J_x^2 + \frac{K_s}{2}(J_t + n_0)^2 + \frac{u}{2} P^2], \tag{C.15}$$

$$\vec{\nabla}\vec{J} = 0, \quad J_t(x = 0, t) = J_t(x = N_x, t) = 0;$$

$$H_2 = -\frac{1}{2} \sum_{n_x, n_t} \frac{F(q_x, q_t) F(q_x, -q_t)}{Q^2 + u + K_s}, \quad Q \equiv \frac{4 \sin^2(q_t/2) + 4 V_d^2 \sin^2(q_x/2)}{K_d}, \tag{C.16}$$

$$F(q_x, q_t) \equiv [-f + K_s n_0 + K_s J_t + u P]_{q_x, q_t}, \tag{C.17}$$

C.2 Measured response

We use the definition of (differential) isochoric compressibility

$$\chi = \frac{1}{N_x N_t}\frac{d}{df_0}\sum_{x,t} f'(x)\langle y(x,t)\rangle_{f_0} = \frac{1}{N_x N_t}\frac{d^2 \ln Z(f)}{df_0^2}. \tag{C.18}$$

So

$$Z(f) = \sum_{\vec{J},P} \exp(-\tilde{H}), \tag{C.19}$$

$$\tilde{H} = \sum_{x,t}[\frac{K_s}{2}J_x^2 + \frac{K_s}{2}(J_t+n_0)^2 + \frac{u}{2}P^2] - \frac{1}{2}\sum_{n_x,n_t}\frac{F(q_x,q_t)F(q_x,-q_t)}{Q^2+u+K_s}, \tag{C.20}$$

$$\chi = \frac{1}{N_x N_t}\left(\sum_{n_x,n_t}\frac{[f']_{q_x,q_t}}{Q^2+u+K_s} + \langle \mathcal{P}^2\rangle - (\langle \mathcal{P}\rangle)^2\right), \tag{C.21}$$

$$\mathcal{P} = \sum_{n_x,n_t}\frac{[K_s J_t + uP]_{q_x,q_t}}{Q^2+u+K_s}[f']_{q_x,q_t}, \tag{C.22}$$

where $[f']_{q_x,q_t}$ stands for full space-time Fourier over the basis (C.13). Since $f'(x)$ is time-independent, we can rewrite it as

$$[f']_{q_x,q_t} = \sqrt{N_t}\delta_{q_t,0}[f']_{q_x},\ [f']_{q_x} \equiv \sqrt{\frac{2}{N_x}}\sum_x f'(x)\sin(q_x x). \tag{C.23}$$

As an example:

$$[1]_{q_x} = \frac{1}{\sqrt{2N_x}}(1-(-1)^n)\cot(q_x/2), \tag{C.24}$$

$$[\sin(q_1 x)]_{q_x} = \sqrt{\frac{N_x}{2}}\,\delta_{q_x,q_1}. \tag{C.25}$$

C.3 Back to real space

We need to express all in real space. Then, $\tilde{H}$ becomes

$$\tilde{H} = \sum_{x,t}[\frac{K_s}{2}J_x^2 + \frac{K_s}{2}(J_t + n_0)^2 + \frac{u}{2}P^2] - \\ - \frac{1}{2}\sum_{x,t;x',t'} U(x,t;x',t')\tilde{F}(x,t)\tilde{F}(x',t'), \tag{C.26}$$

$$U(x,t;x',t') = V(x-x',t-t') - V(x+x',t-t'), \tag{C.27}$$

$$\tilde{F}(x,t) = K_s J_t(x,t) + uP(x,t) - f_0 f'(x) + K_s n_0, \tag{C.28}$$

$$V(z,t) = \frac{1}{N_x N_t}\sum_{n_x,n_t} \frac{K_d \cos(q_x z)\cos(q_t t)}{4\sin^2(q_t/2) + V_d^2 4\sin^2(q_x/2) + K_d(K_s+u)}; \tag{C.29}$$

$$\mathcal{P} = \sum_{x,t} \mu'(x)[K_s J_t(x,t) + uP(x,t)], \tag{C.30}$$

where the factor $\mu'(x)$ depends on the choice in Eqs.(C.24,C.25). In general

$$\mu'(x) = \sqrt{\frac{2}{N_x}}\sum_{n_x} \frac{[f']_{q_x} K_d \sin(q_x x)}{4V_d^2 \sin^2(q_x/2) + K_d(K_s+u)}, \\ q_x = \frac{\pi n_x}{N_x}, n_x = 1,2,...,N_x - 1 \tag{C.31}$$

C.4 Updates

Updates will consist in the standard J-current ones and that for $P \to P \pm 1$ at, say, masha. A simplest one is along space for J_x: $dE_x(x,t) = K_s(J_x(x,t)DJ + 0.5)$. This update contributes to space windings which determine superfluid stiffness $\rho_s = (N_x/N_t)\langle W_x^2\rangle$. It does not involve long-range forces. For the J_t and P updates it is convenient to introduce the *potential* which is to be changed if the update is accepted.

So, for the $J_t(x,t)$ to $J_t \to J_t + DJ$ we can write for the energy cost

$$dE_J(x,t) = K_s \left[DJ \left(J_t(x,t) + n_0 - \Phi(x,t) \right) + 0.5 \left(1 - K_s U(x,t;x,t) \right) \right], \quad \text{(C.32)}$$

Similarly, for $P \to P + DP$:

$$dE_P(x,t) = u \left[DP \left(P(x,t) - \Phi(x,t) \right) + 0.5 \left(1 - uU(x,t;x,t) \right) \right], \quad \text{(C.33)}$$

General expression for Φ is

$$\Phi(x,t) \;\; = \;\; \sum_{x',t'} U(x,t;x',t')[K_s J_t(x',t') + uP(x',t') - f_0 f'(x') + K_s n_0]. \quad \text{(C.34)}$$

But, there is no need to calculate it on each step! Simply, if update is accepted the potential is to be changed as

$$\Phi(x',t') \to \Phi(x',t') + K_s U(x',t';x,t) DJ(x,t) \quad \text{(C.35)}$$

on each site x', t' in the case of (C.32) and

$$\Phi(x',t') \to \Phi(x',t') + uU(x',t';x,t) DP(x,t) \quad \text{(C.36)}$$

in the case (C.33). [It may make sense to use *two* potentials Φ in order to avoid extra multiplication during the pipelining in the cycles (C.35,C.36)]. The potential is to be initialized as $\Phi(x,t) = \sum_{x',t'} U(x,t;x',t')[-f_0 f'(x') + K_s n_0]$.

The estimator $\mathcal{P}$ for χ is to be collected during each update. Specifically, in the case (C.32) it is $\mathcal{P} \to \mathcal{P} + \mu'(x) K_s DJ(x,t)$ and $\mathcal{P} \to \mathcal{P} + \mu'(x) uDP(x,t)$ in the case (C.33).

In the case of grand canonical simulations we will use (C.24) in Eq.(C.31). In the case of canonical one, we will use (C.25) in Eq.(C.31), and will impose a restriction that masha and ira cannot go farther apart in time direction than $N_t/2 - 1$ [that is, distance $N_t/2$ is not already acceptable].

Bibliography

[1] E. Kim, M. H. W. Chan Nature **427**, 225 (2004).

[2] E. Kim, M. H. W. Chan Science **305**, 1941 (2004).

[3] A.S.C. Rittner and J.D. Reppy, Phys. Rev. Lett. **97**, 165301 (2006).

[4] M. Kondo, S. Takada, Y. Shibayama, and K. Shirahama, cond-mat/0607032 (to appear in J. of Low Temp. Phys.).

[5] A. F. Andreev and I. M. Lifshitz, Sov. Phys. JETP **29**, 1107 (1969).

[6] G. V. Chester, Phys. Rev. A **2**, 256 (1970).

[7] D.S.Greywall. Phys. Rev. B **16**, 1291 (1977)

[8] J.Day,T.Herman, and J.Beamish. Phys. Rev. Lett. **95**, 035301 (2005)

[9] J.Day , J.Beamish. Pressure-driven flow of solid helium Phys. Rev. Lett. **96**, 105304 (2006).

[10] A.S.C.Rittner, W.Choi, E.J.Mueller, and J.D.Reppy. Phys. Rev. B **80**, 224516 (2009)

[11] O. Penrose and L. Onsager. Phys. Rev. L , **104** 576 (1956).

[12] Boninsegni M., Prokofev N and Svistunov B Phys.Rev.Lett. **96**, 105301 (2006).

[13] Boninsegni M., A.B.Kuklov *et al.*Luttinger Liquid in the Core of a Screw Dislocation in Helium-4. Phys.Rev.Lett. **99**, 035301 (2007).

[14] J. Toner arXiv:0707.3842v4 [cond-mat.other] 29 Nov 2007.

[15] A. S. C. Rittner and J. D. Reppy arXiv:cond-mat/0702665v2 [cond-mat.other] 23 May 2007.

[16] A. V. Balatsky, M. J. Graf, Z. Nussinov, and S. A. Trugman. Phys. Rev. B **75**, 094201 (2007)

[17] A.Andreev, arXiv:0705.0571v1 [cond-mat.soft] 4 May 2007

[18] E. Kim, J. S. Xia, J. T. West,X. Lin,1 A. C. Clark, and M. H. W. Chan. Rhys. Rev. Lett. **100** 065301 (2008)

[19] Efstratios Manousakis. arXiv:cond-mat/0606383v8 [cond-mat.str-el] 23 Apr 2007

[20] J.Day , J.Beamish. Low-temperature shear modulus changes in solid and connection to supersolidity. Nature: Letters. **450**, 6 Dec.2007.

[21] S. I. Shevchenko, Sov. J. Low Temp. Phys. **13**, 61 (1987).

[22] Singsaas A. and Ahlers G. Phys. Rev. B **29** 4951 (1984)

[23] Lin X., Clark A.C. and Chan M.H.W. Nature **449** 1025 (2007)

[24] S. Balibar and F. Caupin. J. Phys. Condens. Matter **20** (2008) 173201

[25] T. Leggett, Phys. Rev. Lett. **25**, 1543 (1970).

[26] X. Lin,1 A. C. Clark, Z.G.Cheng, and M. H. W. Chan. Phys. Rev. Lett. **102** 125302 (2009)

[27] D.Aleinikava, A.B.Kuklov. Report at Workshop *Supersolidity 2011*, New York, June 7 - June 10, 2011.

[28] J.Day, O.Syshchenko, J. Beamish, Phys. Rev. B**79** 214524 (2009)

[29] A. Granato, K. Lucke, J. Appl. Phys. **27**, 583 (1956); ibid. 789(1956)

[30] J.P.Bouchaud, G.Biroli. Quantum plasticity and dislocation-induces supersolidity. arXiv:0710.3087v4 [cond-mat.stat-mech] 18 Mar 2008; C.R. Physique **9** 1067-1075 (2008)

[31] X.Rojas, C.Pantalei, H.J.Maris, S.Balibar. J. Low Temp. Phys. (2010) **158**:478-484.

[32] X.Rojas, A.Haziot, V.Bapst, S.Balibar. Phys. Rev. Lett. **105** 145302 (2010)

[33] D. Aleinikava, E. Dedits, A.B. Kuklov. J. Low Temp. Phys. (2011) 162: 464-475.

[34] M.W.Ray, R.B. Hallock, Phys. Rev. Lett., **100**, 235301 (2008)

[35] M.W.Ray, R.B. Hallock, Phys. Rev. B, **79**, 224302 (2009)

[36] M.W.Ray, R.B. Hallock, Phys. Rev. B, **81**, 214523 (2010)

[37] M.W.Ray, R.B. Hallock, Phys. Rev. B, **82**, 012502 (2010)

[38] M.W.Ray, R.B. Hallock, arXiv:1007.2156v1

[39] M.W.Ray, R.B. Hallock. Phys. Rev. Lett., **105**, 145301 (2010)

[40] L.D.Landau and E.M.Lifshitz, Statistical Physics, Part 1: Volume 5. Course of Theoretical Physics, 3rd Edition, Butterworth-Heinemann, Oxford, 2000, P.537.

[41] Berezinskii, V. L. Destruction of long-range order in one-dimensional and two-dimensional systems possessing a continuous symmetry group. II. Quantum systems. Sov. Phys. JETP **34**, 610616 (1972).

[42] J. M. Kosterlitz, D. J. Thouless: Ordering, metastability and phase transitions in two- dimensional systems. J. Phys. C, **6**, 1181-1203 (1973).

[43] A.H. Cottrell. Dislocations and plastic flow in crystals. Oxford, At The Clarendon Press, 1958.

[44] D.Hull, D.J.Bacon. Introduction to dislocations. Butterworth, Heinemann, 2009.

[45] J.P.Hirth, J. Lothe, Theory of dislocations, McGraw-Hill, NY-Sydney, 1968.

[46] J. Frenkel. *Zeit. Phys.* **37**, 572 (1926).

[47] P.G. Shewmon, Diffusion in Solids , McGraw-Hill, 1963

[48] S.G. Soyler, A.B. Kuklov, L. Pollet, N.V. Prokof'ev, B.V. Svistunov, Phys. Rev. Lett. **103**, 175301 (2009)

[49] A.M. Kosevich, The crystal Lattice, Wiley-VCH Verlag, CmbH, 2005

[50] J.Friedel, Dislocations (Pergamon Press) 1964.

[51] A.M.Kosevich, E.M.Lifshitz, L.D.Landau and L.D.Pitaevskii, Theory of Elasticity, Third Edition (Theoretical Physics, Vol 7), Reed Educational and Professional Publishing, Ltd. (1986)

[52] P. M. Chaikin and T. C. Lubensky. Principles of condensed matter physics. Cambridge University Press, Cambridge, England, 1995

[53] Materials on the website: http://mcwa.csi.cuny.edu/umass/

[54] N. Metropolis, A.W. Rosenbluth, M.N. Rosenbluth, A.H. Teller, and E. Teller. "Equations of State Calculations by Fast Computing Machines". Journal of Chemical Physics, **21(6)** 1087-1092, 1953

[55] Karen G. Balabanyan. Applications of Worm Algorithm for Monte-Carlo Simulations of Physical Systems Described by the J-current Model. webmaterial: http://mcwa.csi.cuny.edu/umass/JCurrentModelFiles/WAJCM.pdf

[56] M. Wallin, E.S. Sorensen, S.M. Girvin, and A.P. Young, Superconductor-Insulator Transition in Two-Dimensional Dirty Boson Systems, Phys. Rev. B **49**, 12115 (1994).

[57] N.V. Prokof'ev, B.V. Svistunov, Phys. Rev. Lett. **87**, 160601 (2001).

[58] A. Altland and B. Simons, Condensed matter field theory, Cambridge University Press, 2006.

[59] J. Villain, J.Phys. (Paris) **36**, 581 (1975).

[60] W.Janke, H.Kleinert. Nuclear Physics B270[FS16] (1986) 135-153.

A.J.Leggett, Phys. Rev. Lett., **25**, 1543 (1970)

[61] D.Aleinikava, A.B.Kuklov. "Interplay of non-linear elasticity and dislocation-induced superfluidity in solid ^{4}He". arXiv:1110.5884, submitted as an invited paper to the special issue of J. Low Temp. Phys. dedicated to supersolidity.

[62] D. Aleinikava, E. Dedits, A.B.Kuklov, D. Schmeltzer, Europhys. Lett., **89** 46002 (2010), arXiv:0812.0983.

[63] Yu. Kagan, N.V.Prokof'ev, and B.V.Svistunov. Phys.Rev.A **61**, 045601 (2000)

[64] D.Aleinikava, A.B.Kuklov. Phys. Rev. Lett. **106**, 235302 (2011).

[65] B.V.Petukhov and V.L.Pokrovskii, Sov. Phys. JETP **36**, 336 (1973).

[66] L. Pollet, M. Boninsegni, A.B. Kuklov, N.V. Prokof'ev, B.V. Svistunov, M. Troyer Phys. Rev. Lett. **101**, 097202 (2008), Phys. Rev. Lett. **101**, 269901 (2008)

[67] N. Prokof'ev and B. Svistunov, Phys. Rev. Lett. **94**, 155302 (2005)

[68] M.W. Ray, R.B. Hallock, arXiv:1106.1084.